NANYANG
TECHNOLOGICAL
UNIVERSITY

COMPLEX METAL OXIDE-BASED ELECTRODE MATERIALS FOR ELECTROCHEMICAL ENERGY STORAGE

YU LE

SCHOOL OF CHEMICAL AND BIOMEDICAL ENGINEERING

2016

COMPLEX METAL OXIDE-BASED ELECTRODE MATERIALS FOR ELECTROCHEMICAL ENERGY STORAGE YU LE 2016

COMPLEX METAL OXIDE-BASED ELECTRODE MATERIALS FOR ELECTROCHEMICAL ENERGY STORAGE

YU LE

School of Chemical and Biomedical Engineering

A thesis submitted to the
Nanyang Technological University
in partial fulfillment of the requirement for the degree of
Doctor of Philosophy

2015

Acknowledgement

First and foremost, I would like to express my deepest respect and the most sincere gratitude to my supervisor, Assoc. Prof. David Lou Xiong Wen, for his patient instructions throughout my project. All my research work is under his smart ideas and inspirations. Whenever I encounter any problem in the experiments and turn to him for advice, he will always manage to squeeze some time from the busy schedule to guide me utilizing his knowledge and experience and give me many good suggestions. He always encourages me when I feel down and persuades me to keep modesty all the time. Also, I would also like to extend my thanks and appreciations to my co-supervisor, Assoc. Prof. Lim Teik Thye. He is always ready for providing any assistance I need and his kindness will be remembered.

I am extremely grateful to the staffs and research facilities in School of Chemical and Biomedical Engineering, School of Physical and Mathematical Sciences and School of Materials Science and Engineering, especially Dr. Wang Xiujuan. Dr. Ong Teng Teng, and Dr. Yu Shucong for their kindly assistance in sample analyses.

Special thanks are extended to all of the former and present colleagues for their precious friendship in daily life, and helpful discussion and collaboration in research.

Last but not least, I would like to give my special and deepest gratitude to my wife and my parents for their ongoing love and vigorous support throughout my life.

Abstract

Complex metal oxides, especially in the form of nanostructures, have attracted increasing attention as promising electrode materials for electrochemical energy storage (EES) systems such as lithium-ion batteries (LIBs) and hybrid supercapacitors (HSCs) owing to their superior structure features compared to the simple binary metal oxides. In this project, we focus the rational design and synthesis of two representative types of complex metal oxide-based electrodes including hybrid systems and ternary metal oxides, as well as their applications in LIBs and HSCs.

The hybrid metal oxides systems include TiO_2@Fe_2O_3 integrated electrodes and $NiCo_2O_4$@MnO_2 core-shell structures. In the former case, we have designed a smart nanocomposite composed of aligned TiO_2 nanotube arrays (TNAs) with attached Fe_2O_3 hollow nanorods on both the outer and inner surface. The unique core-shell architecture has been created by introducing FeOOH nanospindles onto the TNAs with a follow-up thermal treatment in air. Benefitting from their structural superiorities, such a hierarchical structure displays excellent lithium storage property with a remarkable areal capacity and a good cycle performance.

Hierarchical $NiCo_2O_4$@MnO_2 core-shell heterostructured nanowire (NW) arrays grown on nickel foam are produced via a facile two-step hydrothermal method. The core-shelled NW arrays on nickel foam, own obvious advantages as an electrode for HSCs due to the strong synergistic effect from the mesoporous $NiCo_2O_4$ NW core and the sheet-like MnO_2 shell. Impressively, such advanced integrated array exhibits a

large areal capacitance, satisfying rate and cycling performance in a LiOH solution.

The three typical examples of ternary metal oxides systems are $Co_xMn_{3-x}O_4$ micro-/nanostructures array, $NiCo_2O_4$ hierarchical structures and yolk-shelled Ni-Co mixed oxide prisms. Hierarchical $Co_xMn_{3-x}O_4$ micro-/nanostructures array has been developed through a facile two-step process. Co-Mn precursor with tunable morphology and composition on stainless steel matrix is firstly synthesized via tuning the solvent components during the solvothermal process. The mesoporous $Co_xMn_{3-x}O_4$ micro-/nanostructures with various macroscopic features from nanowires to nanosheets can be finally obtained through a further annealing process at 600 ^{o}C with a slow ramping rate. The distinct micro-/nanostructures endow the $Co_xMn_{3-x}O_4$ sample with outstanding rate capacities at high current densities with enhanced capacity retention after 30 cycles as anode material for LIBs.

Other than the binder-free array structures, micro-/nanostructured particles can overcome the limit of loading mass for the active materials. Similar to $Co_xMn_{3-x}O_4$ system, hierarchical $NiCo_2O_4$ structures composed of wire-like or sheet-like mesoporous building blocks can be prepared via a facile two-step route. The outer morphologies can be easily tuned via the control of the reaction solvents. These distinct hierarchical architectures could ensure the fast electronic/ionic dynamics, large surface area, and enhanced mechanical integrity. When applied as electrode materials for high-performance HSCs, these $NiCo_2O_4$ micro-/nanostructures deliver large specific capacitance with long calendar life. Starting with prism-like metal acetate hydroxide, Ni-Co mixed oxide nanoprisms with yolk-shelled characteristic

and tunable chemical element can be prepared by a simple oxidation process in air. The formation mechanism can be attributed to the fast thermally driven contraction process. Thanks to the intriguing porous structure with desirable composition, these yolk-shelled Ni-Co oxides represent greatly enhanced electrochemical activities as energy source for hybrid supercapacitors with amazing capacitance retention over 15000 cycles. Moreover, these interesting materials can effectively buffer the structural stress during Li ions insertion/extraction process, leading to highly reversible specific capacities at diverse densities.

Table of Content

List of Abbreviations

EES: electrochemical energy storage

LIBs: lithium-ion batteries

HSCs: hybrid supercapacitors

EDLC: electric double layer capacitors

ALD: atomic layer deposition

CVD: chemical vapor deposition

TiO_2: titanium dioxide

Fe_2O_3: iron oxide

TNAs: titania nanotube arrays

FeOOH: iron oxide hydroxide

$NiCo_2O_4$: nickel cobalt oxide

MnO/MnO_2: manganese oxide

$Co_xMn_{3-x}O_4$/ $CoMn_2O_4$: cobalt manganese oxide

$MnCo_2O_4$/ $Mn_{1.5}Co_{1.5}O_4$: manganese cobalt oxide

Ni-Co: nickel cobalt

MOs: metal oxides

NiO: nickel oxide

Li_2O: lithium oxide

Li: lithium

Ti: titanium

Ni: nickel

LiOH: lithium hydroxide

KOH: potassium hydroxide

SnO_2/SnO: tin dioxide

CoO/Co_3O_4: cobalt oxide

V_2O_5: vanadium oxide

WO_{3-x}: tungsten oxide

Au: gold

MMn_2O_4: manganites

MFe_2O_4: irontites

MCo_2O_4: cobaltites

$ZnCo_2O_4$: zinc cobaltites

$ZnFe_2O_4$: zinc irontites

$ZnMn_2O_4$: zinc manganites

CMP: cobalt manganese precursor

$Co_{0.33}Mn_{0.67}CO_3$: cobalt manganese carbonate

(Co, Mn)OOH: cobalt manganese oxide hydroxide

Co-Mn: cobalt manganese

NC-EH: nickel cobalt precursor prepared in ethanol and water

NC-E: nickel cobalt precursor prepared in ethanol

NCO: nickel cobalt oxide

AAO: aluminum oxide

ZIF 67: zeolitic imidazolate framework-67

LDH: layered double hydroxides

EG: ethylene glycol

NH_4F: ammonium fluoride

$FeCl_3$: iron chloride

$LiPF_6$: Lithium hexafluorophosphate

CTAB: cetyltrimethylammonium bromide

PEG: polyethylene glycol

HMT: hexamethylenetetramine

$Zn(CH_3COO)_2$: zinc acetate

$Co(NO_3)_2\cdot 6H_2O$: cobalt nitrate hexahydrate

$Ni(NO_3)_2\cdot 6H_2O$: nickel nitrate hexahydrate

$KMnO_4$: potassium permanganate

$MnSO_4\cdot H_2O$: manganese sulfate

PVP: polyvinylpyrrolidone

EtOH: ethanol

DI: deionized

super-P-Li: carbon black

PVDF: polyvinylidene difluoride

Pt: platinum

Hg/HgO: mercury/mercury oxide

SCE: saturated calomel electrode

NC: nanocrystal

NW: nanowire

NS: nanosheet

NF: nanoflake

NCs: nanocages

DSNCs: double-shelled nanocages

1D: one-dimensional

2D: two-dimensional

3D: three-dimensional

V/V: volume to volume

W/W: weight to weight

ΔT: temperature gradient

F_c: contraction force

F_a: adhesive force

JCPDS: international centre for diffraction data

Sat.: satellites

AC: alternating current

ASC: areal specific capacitance

FESEM: field-emission scanning electron microscope

TEM: transmission electron microscope

HRTEM: High-resolution transmission electron microscope

SAED: selected-area electron diffraction

XRD: X-ray diffraction

EDX: energy-dispersive X-ray spectroscopy

HAADF-STEM: high-angle annular dark-field STEM

XPS: X-ray photoelectron spectroscope

ICP: inductively coupled plasma

TGA: Thermogravimetric analysis

BET: Brunauer-Emmett-Teller

CV: cyclic voltammetry

CP: chronopotentiometry

EIS: electrochemical impedance spectroscopy

List of Tables

List of Figures

Chapter 1. Introduction

1.1. Background

With the imminent shortage of fossil fuels and growing environmental concerns, the demands for high-efficiency electrical energy storage (EES) technologies are becoming more and more critical.[1, 2] As two typical devices of EES systems, lithium ion batteries (LIBs) and hybrid supercapacitors (HSCs) are promising technological choices for large-scale applications (stationary energy storage, electric vehicles and even electrical grids, etc.) in virtue of their high power/energy density with long life span.[3] Generally, an EES device is composed of three essential components: a negative electrode (anode), a positive electrode (cathode), and an electrolyte.[4-6] Despite different definitions, electrochemical energy storage/release process for both LIBs and HSCs relies on electron and ion charge/discharge at the electrodes.[7, 8] The working principle involves the voltage controlled reversible movement of the ions between the electrodes via the electrolytes as the media. Meanwhile, the electrons flow through the external circuit to sustain the charge balance. Overall, the performances of LIBs and HSCs are determined by the property of their electrodes.[4, 9, 10] Therefore, further breakthroughs in electrode materials are crucial to realize new generations of high-efficiency EES devices.

Amongst numerous candidates, a series of metal oxides (MOs) has been intensely investigated as potential electrode materials for LIBs and HSCs.[8, 11, 12] Generally speaking, MOs have a multitude of possible stoichiometric compositions, crystal structures, valence states, and nanocrystalline morphologies, endowing them with rich electrochemical activities and thus superior specific capacities/capacitances over the commercialized carbon/graphite-based electrode.[13-15] For application in LIBs, MOs exhibit high capability of lithium storage by the formation of a Li_2O buffering matrix during electrode reaction (conversion type) or favorable crystal structure for lithium insertion (insertion type) or alloying/dealloying reaction (alloy type).[12] The electrochemical reactions involved in these three types are displayed as follows:

Conversion type (M_xO_y, M = Mn, Fe, Co, Ni, and Cu):

$$M_xO_y + 2yLi^+ + 2ye^- \leftrightarrow xM + yLi_2O \quad (1)$$

Insertion type (MO_x, M=Ti):

$$MO_x + yLi^+ + ye^- \leftrightarrow Li_yMO_x \quad (2)$$

Alloy type (M_xO_y, M=Sn):

$$M_xO_y + 2yLi^+ + 2ye^- \rightarrow xM + yLi_2O \quad (3)$$

$$M + zLi^+ + ze^- \leftrightarrow Li_zM \quad (4)$$

When applied in HSCs, most MOs usually serve as the battery-type faradaic electrodes for energy source in alkaline solution, in which the charge storage mainly comes from redox reactions on the surface.[14-16] The specific reaction can be described as follow:

$$MO + OH^- \leftrightarrow MOOH + e^- \text{ (MO, M = Ni, Co, Cu, and Mn)} \quad (5)$$

Combined with a capacitor-like electrode as power source, the cell voltage, energy and power densities of the HSCs system could be further improved in comparison to conventional carbon-based pseudocapacitors in neutral environment.[17]

Unfortunately, the employment of MOs in LIBs and HSCs are largely hampered by the sluggish electron/ionic transport kinetics (wide-bandgap nature) and pronounced volumetric expansion and contraction of the electrode during the discharge/charge process. As a result, MOs based electrode usually display undesirable rate performance, fast capacity fading and short calendar life.[13-15]

1.2. Motivation

The employment of nanostructured complex electrode materials represents a promising avenue to settle the above-mentioned obstacles and achieve enhanced electrochemical performance of metal oxides. Compared to simple binary metal oxides, the usage of the complex metal oxides can enhance the essential properties of each single component in term of ameliorative electrical/ionic conductivity, redox activity, reversible capacity, and mechanical stability due to the synergetic effects from different metal cations.[3, 8] Moreover, combined metal oxides with different energy storage mechanisms can make full use of electrolyte or afford additional capacity to total electrochemical energy storage. Overall, these complex systems can be approximately classified into two categories, including hybrid metal oxides systems and single-phase multiple metal oxides. The former groups are the mixtures of two or more metal oxides as different components. The latter systems are single-phase multinary metal oxides with multiple metal elements (For ease of discussion, in this thesis, this system only refers to the ternary metal oxides).

Notwithstanding continuous efforts, the results achieved by nanostructured hybrid electrode materials so far are still not satisfying. Therefore, it is still desirable to boost the electrochemical properties of LIBs and HSCs via rational design and synthesis of the complex structures with unique features (e.g., hierarchical micro-/nanostructures; porous; yolk-shelled structures).

1.3. Overall Objective

The objective of this project is the rational design and synthesis of complex metal oxide-based electrode materials and establishment of the internal relationship between structure and their electrochemical activities as the electrode for LIBs and HSCs. To be specific, this program mainly focuses on the nanostructuring of hybrid systems as binder-free electrodes and ternary metal oxides with smart architectural features and studying their performance in LIBs and HSCs. The hybrid systems contain the mixtures of simple binary metal oxides or the composite of binary and ternary metal oxides. For the ternary metal oxides, abundant advanced merits of micro-/nanostructures have been integrated within the individual single-phrase material. In order to break through the loading mass limit, monodispersed ternary metal oxides nanoparticles are prepared with unique hollow configurations. Based on these considerations, the objective of this project can be generally summarized into the following three parts.

1.3.1. To Develop Hierarchical Hybrid Metal Oxides Arrays with Desired Structures and Compositions as Binder-free Electrode

The employment of hybrid nanostructures is a satisfying direction to enhance the electrochemical activity of electrode due to the synergistic effect from each component. The rational design for the hybrid structure plays a key factor to determine the overall activity of the composite. In our project, one objective is to discover the outstanding hybrid systems with desirable components as integrated electrodes for LIBs and HSCs. To achieve this target, two superior hybrid structures, Fe_2O_3@TiO_2 framework and $NiCo_2O_4$@MnO_2 core-shell system, are studied. Besides the structural characterizations, substantial electrochemical investigations are carried out to reveal their synergetic advantages and limitations.

1.3.2. Construction of Ternary Metal Oxides Hierarchical Structures as Electrodes

Compared with binary metal oxides, ternary metal oxides exhibit enhanced electrical/ionic conductivity and structural stability during the electrochemical reactions. Nanoengineering ternary metal oxide with a highly-porous hierarchical micro-/nanostructures has been regarded as a new solution for EES system. To fulfill this goal, porous $Co_xMn_{3-x}O_4$ and $NiCo_2O_4$ hierarchical structures have been developed with exceptionally hierarchical structures. Through delicate control of the synthesis conditions, the morphology and chemical composition of these systems can be adjusted. Besides, the inherent relationship between the material merits and improved electrochemical activity are revealed through the systematic analysis.

1.3.3. Exploring Ternary Metal Oxides with Advanced Hollow Structures for High-performance Electrochemical Energy Storage

Hollow structured nanomaterials gain great success as advanced electrode configuration. Recent advances in the synthetic method bring the possibility to further modify the hollow structure with enhanced energy and power density. In this regards, we prepare yolk-shelled Ni-Co mixed oxide nanoprisms through a facile template-engaged method. In addition, the shape and composition of final product can be further tailored by altering the Ni/Co molar ratio in the precursor. When evaluated as electrodes for both HSCs and LIBs, the distinguished complex hollow features endow the yolk-shell prism with greatly enhanced electrochemical properties. The composition dependent properties are also investigated to demonstrate the componential advantages.

1.4. Organization

The detailed frame of this thesis is listed as below:

Chapter 1 is a brief introduction of the background, motivation of the project and objectives of this research project. Then, Chapter 2 summarizes recent research progress in the rational design and preparation of two representative types of complex metal oxide-based electrodes and their applications in LIBs and HSCs. The common synthetic procedures, structure characterizations, and electrochemical measurement parameters used in this project are presented in Chapter 3. From Chapter 4 to 8, five outstanding systems of complex metal oxide-based electrode materials are presented, including TiO_2@Fe_2O_3 3D frameworks, $NiCo_2O_4$@MnO_2 core-shell arrays, hierarchical arrays composed by $Co_xMn_{3-x}O_4$ nanowire or nanosheet, morphology controlled $NiCo_2O_4$ micro-/nanostructures, and yolk-shelled Ni-Co mixed oxide nanoprisms. The electrochemical performance of above complex materials as electrodes for LIBs and HSCs are also investigated. Lastly, the Chapter 9 sums up the major results and findings of the above systems, together with some suggestions for future works in this research area.

Chapter 2. Literature Review

2.1. Overview of Lithium-ion Batteries and Hybrid Supercapacitors

As two typical electrical energy storage (EES) devices, lithium ion batteries (LIBs) and hybrid supercapacitors (HSCs) are promising technological choices for large-scale applications, in virtue of their high power/energy density with long life span.[3] Generally, an EES device is composed of three essential components: a negative electrode (anode), a positive electrode (cathode), and an electrolyte.[4, 5] Basically, electrochemical energy storage/release process for both LIBs and HSCs relies on electron and ion charge/discharge at the electrodes.[6-8] As schematic represented in **Figure 2.1**, the working principle involves the voltage controlled reversible movement of the ions within the two electrodes via the electrolytes. Meanwhile, the electrons flow across the exterior circuit to sustain the charge balance. Overall, the performances of LIBs and HSCs are determined by the property of their electrodes.[4, 9, 10] However, the activities of traditional electrode materials are approaching their inherent limits. Therefore, further breakthroughs in electrode materials play a crucial role to realize new generations of high-efficiency EES devices.

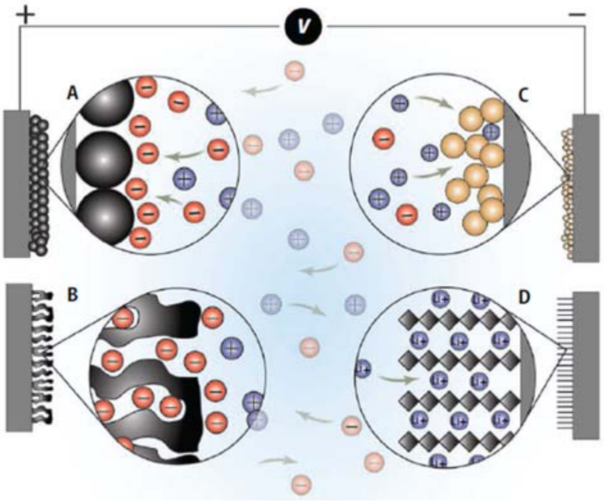

Figure 2.1 Schematic representation of LIBs and HSCs.[6] Reproduced with permission from ref. 6. Copyright 2014 Kristy Jost/Drexel University.

Amongst available alternatives, metal oxides (MOs) attract ever-growing research interests as potential electrode materials for both LIBs and HSCs. Generally speaking, MOs have a multitude of possible stoichiometric compositions, crystal structures, valence states, and nanocrystalline morphologies, endowing them with higher electrochemical activities. As anode materials in LIBs, MOs can storage lithium through reversible electrochemical reaction as "conversion reaction" to form a Li_2O buffering matrix with high capacity or intercalation of lithium ions (e.g. TiO_2) or alloying/dealloying reaction (e.g. SnO_2). However, the practical performance of these MOs is largely compromised by numerous obstacles, especially the intrinsic low charge/ionic conductivity and unsatisfying cycling stability related to the pronounced volume expansion during the reactions.

When applied as energy source in hybrid supercapacitors (HSCs), MOs with variable valences can storage charge through reversible surface or near-surface faradaic redox reactions. These battery-like electrodes are promising to achieve battery-level energy density together with comparable cycle stability and high power density as traditional electric double layer capacitors (EDLCs). Combined with a capacitor-like electrode as power source, the cell voltage, energy and power densities of the HSCs system could be further improved in comparison to conventional pseudocapacitors. Nonetheless, sufficient electrochemical active area and favorable electro-conductivity are requested for these MOs materials to achieve optimum performance.

The great advances in the development of micro-/nanostructures as electrode materials provide the possibility to solve the current problems of metal oxides in LIBs and HSCs, which can ensure enhanced electrochemical performance.[4, 8, 11, 12, 18-24] To be specific, nanosized structures endow the metal oxides with a shorter ion diffusion path and increased specific surface area for good penetration of the electrolyte, leading to enhanced rate capability. Meanwhile, the microsized configuration could effectively prevent the agglomeration of nanoparticles during the discharge-charge process, leading to modified cycling stability of the electrode. Furthermore, the employment of the complex systems can retain and remarkably ameliorate the essential properties of binary metal oxides such as electrical/ionic conductivity, redox activity, reversible capacity, and mechanical stability due to the synergistic effect from each component. To fully exert their advantages, the structures of complex electrode materials are often need to be optimized with desirable architectures. Thanks to the great advancement in modern emerging synthetic approaches, considerable research has concentrated on the rational design and synthesis of complex metal oxide micro-/nanostructures with inspiring results. In the following sections, we will review the recent progress in complex metal oxides (hybrid systems and ternary metal oxides) as advanced electrodes for LIBs and HSCs, as summarized in **Tables 1** and **2**.

Table 1 Hybrid metal oxides systems for LIBs and HSCs

Category	**Material**	**Synthesis method**	**Electochemical performance**	**Reference**
3D core-shelled structure	Branched α-Fe_2O_3 nanorod @SnO_2 nanowire	CVD & hydrothermal method	1167 mAh g^{-1} at 1 A g^{-1} for LIBs	[25]
3D core-shelled structure	TiO_2/SnO array	Anodization & hydrothermal method	675 mAh g^{-1} at 50μ A g^{-1} for LIBs	[26]
3D core-shelled structure	SnO_2@V_2O_5 core-shell nanowires	CVD & hydrothermal method	126 mAh g^{-1} at 0.5 A g^{-1} for LIBs	[27]
3D core-shelled structure	Co_3O_4 nanowires@ MnO_2 nanosheets	Two-step hydrothermal method	0.56 F g^{-1} at 11.25 mA cm^{-2} for HSCs	[28]
3D core-shelled structure	CoO-TiO_2 wire-in-tube	Hydrothermal method & ALD	2.85 F cm^{-2} at 10 mA cm^{-2} for HSCs	[29]
Hollow structure	α-Fe_2O_3@SnO_2 rattle-type structures	Two-step solvothermal method	1621 mAh g^{-1} at 200 mA g^{-1} for LIBs	[30]
Hollow structure	SnO_2-V_2O_5 double-shelled hollow spheres	One-step solvothermal method	673 mAh g^{-1} at 250 mA g^{-1} for LIBs	[31]
Hollow structure	Co_3O_4/$NiCo_2O_4$ double-shelled nanocages	Two-step solvothermal method	805 F g^{-1} at 10 A g^{-1} for HSCs	[32]

Table 2 Ternary metal oxides systems for LIBs and HSCs

1D nanostructure	$ZnMn_2O_4$ nanowires	Hydrothermal method & solid-state reaction	350 mAh g^{-1} at 1 A g^{-1} for LIBs	[33]
2D nanostructure	Hexagonal $NiCo_2O_4$ nanoplates	One-step solvothermal method	270 F g^{-1} at 1 A g^{-1} for HSCs	[34]
3D hierarchical nanostructure	$CoMn_2O_4$ microspheres assembled by 2D nanoflakes	One-step solvothermal method	894 mAh g^{-1} at 100 mA g^{-1} for LIBs	[35]
3D hierarchical nanostructure	Mesoporous ultra-layered $NiCo_2O_4$ nanostructures	One-step solvothermal method	407 F g^{-1} at 1 A g^{-1} for HSCs	[36]
3D hierarchical nanostructure	Mesoporous $NiCo_2O_4$ nanosheets on four diverse conductive matrixes	One-step solvothermal method	2 F cm^{-2} at 8.5 A cm^{-2} for HSCs	[37]
3D hierarchical nanostructure	$ZnCo_2O_4$ nanowire arrays on carbon cloth matrix	One-step solvothermal method	1300 mAh g^{-1} at 200 mA g^{-1} for LIBs	[38]
Hollow structure	$ZnFe_2O_4$/C hollow spheres	One-step solvothermal method	910 F g^{-1} at 65 mA g^{-1} for LIBs	[39]
Hollow structure	Ball-in-ball $ZnMn_2O_4$ hollow microspheres	One-step solvothermal method	750 F g^{-1} at 400 mA g^{-1} for LIBs	[40]
Hollow structure	$NiCo_2O_4$ tube-in-tube structure	Single-spinneret electrospinning technique	1610 F g^{-1} at 5 A g^{-1} for HSCs	[41]

2.2. Hybrid Metal Oxides Systems for LIBs and HSCs

The hybrid metal oxides systems are mixtures of two or more metal oxides as different components, which possess not only all merits of metal oxides materials from each constituents (e.g., high capacity and environmental benignity) but also bring some unique synergistic effects (e.g., accommodation of the volume variation during charging/discharging process).[42] By rationally designing the structures and compositions of each constituent, modified performance can be revealed in such hybrid electrodes for LIBs and HSCs.

2.2.1. Three-Dimensional Core-shelled Hybrid Metal Oxides

Three-dimensional (3D) core-shelled hybrid structure is a typical kind of architectures for hybrid systems used in LIBs and HSCs. The core-shelled electroactive nanostructures are directly formed onto current-collector matrix as binder-free 3D electrodes, in which the core and shell materials are different with each other for the hybrid metal oxides. Compared with the granule system, the ordered nanostructure arrays as device electrodes can offer direct channels for electronic delivery and endure structural stress during repeated discharging-charging process to boost electrochemical performance. Besides, this smart design can efficiently reduce the surface energy to minimize the side reaction between the active material and electrolyte. In addition, the core-shell structure can prevent the particle aggregation during the discharge/charge process to give improved cycling performance. Therefore, the electrochemical reversibility can be largely improved.

Inspiring by these advantages, many research group have done some salutary attempts to develop advanced electrodes composed of 3D core-shelled hybrid structures using simple binary metal oxides.

As for electrode materials for LIBs, the utilization of core-shell hybrid metal oxides systems focuses on combination of metal oxides with different lithium storage mechanisms (conversion type, insertion type and alloy type).[25, 26, 30, 31, 43-51] The enriched reaction activities grant the hybrid with enhanced capacities. For instance, Zhou and coworkers used chemical vapor deposition (CVD) technique with hydrothermal process to manufacture a hierarchical nanostructure grown on stainless steel foil composed of six-fold-symmetry branched convention-type α-Fe_2O_3 nanorod on alloy-type SnO_2 wire-like stem (**Figure 2.2**).[25] Besides, the lengths and growth direction of Fe_2O_3 nanorods can be simply controlled through the adjustment of parameters during the synthesis of FeOOH precursors. Such heterogeneous electrode demonstrates enhanced performance, compared to both individual components with lower initial irreversible capacity loss. This work demonstrates the potential of hybrid structures in LIBs. Based on a similar concept, there are several excellent works reported for application in LIBs, such as a nanoarchitectured TiO_2/SnO arrays for high power density Li-ion microbatteries presented by Ortiz and coworkers and a SnO_2@V_2O_5 core-shell nanowires prepared by Lee's group.[26, 27]

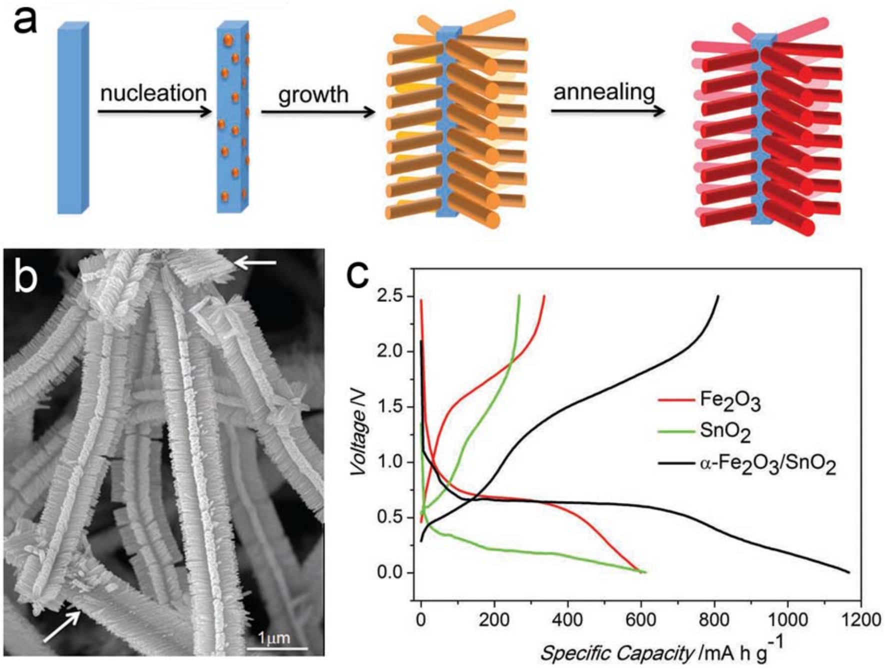

Figure 2.2 (a) Schematic of preparation procedures for the hierarchically assembled α-Fe_2O_3/SnO_2 nanocomposite. (b) Typical SEM image of α-Fe_2O_3/SnO_2 branched nanostructure. (c) First charge-discharge profiles of bare α-Fe_2O_3 nanorod arrays, pristine SnO_2 nanowires, and α-Fe_2O_3/SnO_2 branched nanostructure.[25] Reproduced with permission from ref. 25. Copyright 2011 Wiley.

As for the HSCs, one of the effective strategies to bridge the gap of performance among various types of electrode materials for HSCs is the usage of hybrid nanostructures composed of battery-like material as shell structure and carbon-based conductive matrix as the core.[8] Unfortunately, in order to obtain high rate and cycling stability, a relatively low weight fraction is considered at the sacrifice of energy density. Recently, research interests have been aroused by novel electrode designs of hybrid battery-like materials into 3D core-shell structures using different metal oxides.[52-57] This pioneering design could exhibit all advantages of hybrid structures with enhanced capacitance versus the carbon-based nanocomposites.

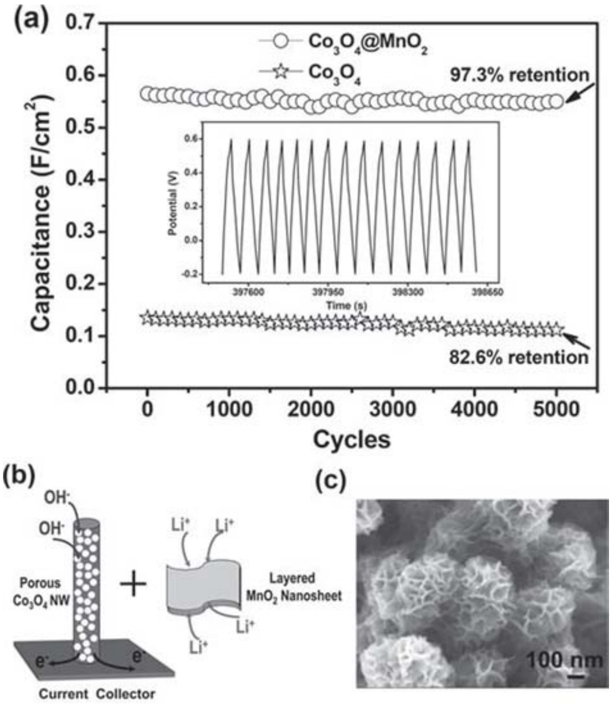

Figure 2.3 (a) Cycling performance of the core-shell composite and Co$_3$O$_4$ nanowire arrays over 5000 cycles. (b) Charge storage mechanism of the core-shell composite array and both the anions and cations are used to contribute to the total capacitance. (c) Typical SEM image of the hybrid array.[53] Reproduced with permission from ref. 53. Copyright 2011 Wiley.

A classical case is the porous Co$_3$O$_4$ nanowires@MnO$_2$ nanosheets core-shell arrays, which is reported by Fan and coworkers (**Figure 2.3**).[53] The hybrid array is synthesized through a facile carbon-assisted hydrothermal reaction. For applications in SCs, such smart design manifests several noteworthy structure merits. For one thing, both the inner and outer materials are typical battery-like metal oxides in alkaline solution with different charge-storage mechanisms. Besides the redox reactions with anions, the MnO$_2$ shell can absorb the cations in the electrolyte. Therefore, the well-designed structure can make full utilization of ions in the electrolyte, leading to enhanced charge storage. Moreover, the nanowires are well separated and keep good attachment to the conductive matrix without binder, which substantially reduces inactive surface in the electrode. In addition, the single-crystalline Co_3O_4 nanowire core can serve as a direct channel for electron transport during charge/discharge. Benefitting from above structural merits, the hybrid array exhibits an excellent areal capacitance, much better than that of the individual Co_3O_4 nanowire array at different current densities.

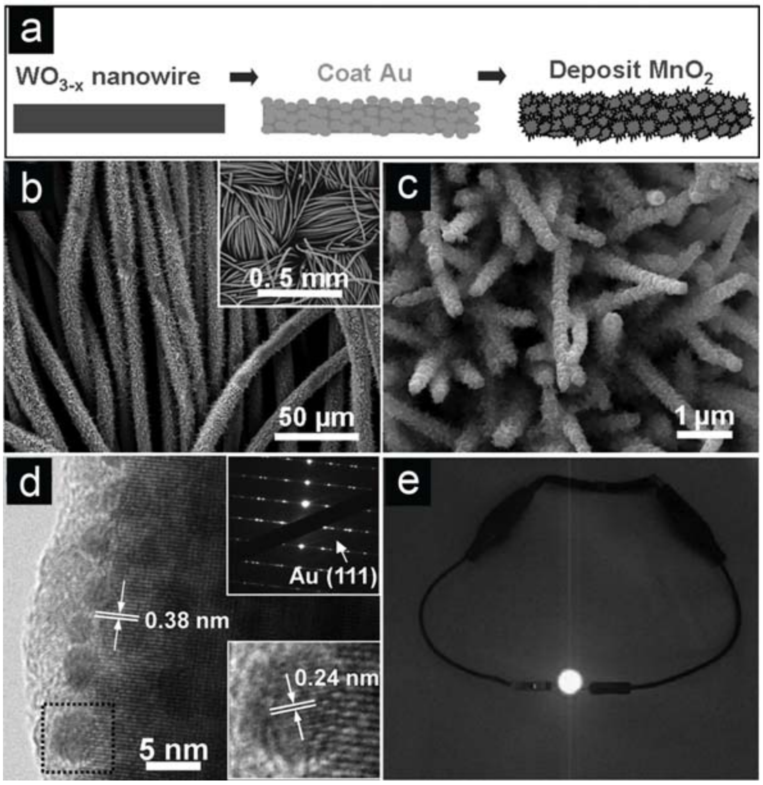

Figure 2.4 (a) Schematic for preparation of WO_{3-x}@Au@MnO_2 core-shell structure. (b) SEM images of the as-prepared WO_{3-x} NWs on carbon fabric and (c) WO_{3-x}@Au@MnO_2 NWs on carbon fabric. (d) HRTEM image of WO_{3-x}@Au@MnO_2 NW. (e) Demonstration of light-emitting diode (LED) driven by two flexible solid-state devices of WO_{3-x}@Au@MnO_2.[54] Reproduced with permission from ref. 54. Copyright 2012 Wiley.

Similarly, there are other excellent works of hybrid metal oxide-based architectures using MnO_2 as shell materials for SCs. Lee *et al.* presented a novel SnO_2@MnO_2 core-shell structure as electrode material for HSCs. The 1D SnO_2

nanowires with good electronic conductivity on stainless steel is firstly synthesized through CVD method. Then, the amorphous MnO_2 layer is deposited via a solution-based method.[58] The energy density and power density measured at various currents demonstrate the good rate capability, indicating the hybrid array is very suitable and promising for fabricating supercapacitors. Wang and his coworkers introduced an Au layer coating between the total WO_{3-x} nanowire core and MnO_2 shell to further modify the collection of charge (**Figure 2.4**).[54] The core-shell structures grown on highly flexible carbon fabric show remarkable cycling life. As an outstanding electrode for HSCs, the composite delivers high power density of 30.6 kW kg^{-1} and energy density of 106.4 Wh kg^{-1}. More specifically, they can also be used to assemble a flexible solid-state capacitive device. These inspiring results display the high possibility of the WO_{3-x}@Au@MnO_2 structures as the flexible electrode for next-generation supercapacitors. More recently, Fan *et al.* proposed and demonstrated a general concept of the "wire in tube" nanostructures for electrochemical energy storage application. With the help of atomic layer deposition (ALD), a hollow space as a nanogap is introduced between core and shell structures of CoO-TiO_2 to ensure an increased reaction area and the structural integrity after long-time cycling. Such novel structures with advanced electrochemical performance again prove the promising use of 3D core-shell structures using mixed metal oxides in supercapacitors.[29]

2.2.2. Hollow Structured Hybrid Metal Oxides

Apart from the 3D core-shell architectures, hollow structures, especially complex hollow systems with yolk-shelled or multi-shelled features, have also been demonstrated as a successful class as smart electrodes for LIBs and HSCs. The well-defined hollow structures composed of nanosized subunits could guarantee reduced ion diffusion paths, alleviate the structural stress and accommodate the large volume expansion related with repeated discharge-charge cycles, resulting in improved cycling life.

There are some inspiring progresses in this field with intriguing results. An instance of such smart architecture is an interesting a-Fe_2O_3@SnO_2 rattle-type hollow structures composed of a porous SnO_2 shell and a portable a-Fe_2O_3 core, which is reported by Lou and coworkers (**Figure 2.5**).[30] The hollow space between core and shell is formed by hydrothermal process can efficiently withstand the drastic volume change accompanied by cycling process. Besides, it can also act as a barrier to prevent the encapsulated electroactive nanoparticles from aggregation. When served as electrode in LIBs, the hybrid electrode manifests reduced irreversible loss during the initial cycle with long-term stability compared to SnO_2. Besides, the synergistic effect also lies in the catalytic activity of nanosized iron particles, which is beneficial to the reversibility of the alloy reaction between SnO_2 and lithium, leading to a higher reversible capacity.

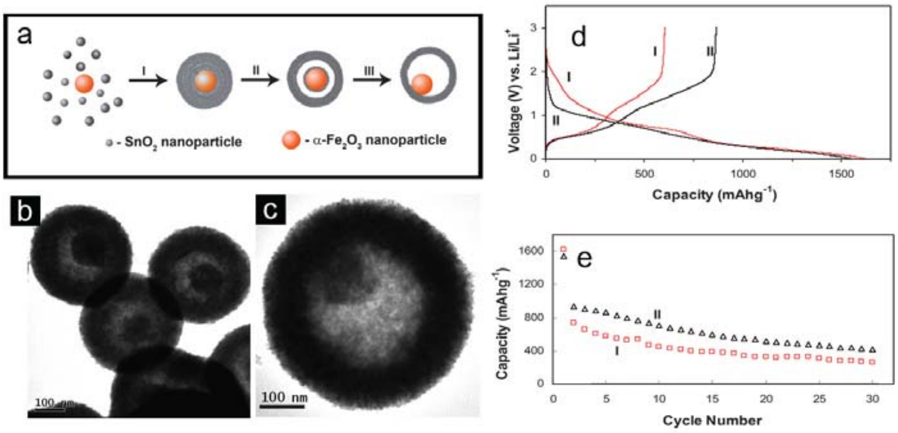

Figure 2.5 (a) Schematic illustration of α-Fe_2O_3@SnO_2 nanorattles synthesized via inside-out Ostwald ripening process. (b, c) TEM images of α-Fe_2O_3@SnO_2 nanorattles. (d, e) Discharge/charge profiles at the 1st cycle and cycling test of SnO_2 hollow spheres (I) and α-Fe_2O_3@SnO_2 nanorattles (II).[30] Reproduced with permission from ref. 30. Copyright 2009 RSC.

Xue *et al.* selected double shell V_2O_5 as the matrix to successfully fabricate SnO_2-V_2O_5 double-shelled hollow spheres based on a combined Ostwald ripening method.[31] Further structural examinations demonstrate that tiny SnO_2 nanocrystals are homogeneously loaded on V_2O_5 support. As anode and cathode materials for LIBs, the homogenous nanocomposite exhibits a very high reversible capacity, remarkable cycle life, and good rate performance benefitting from their architecture merits.

The composition-dependent electrochemical performance has been approved by core-shell structures as we described in the last section. However, due to the technological obstacles in the synthesis, the hollow structures using hybrid metal oxides is seldom reported for the HSCs. Recently, our group has reported a novel Co_3O_4/$NiCo_2O_4$ double-shelled nanocages (DSNCs) for HSCs. By partly transformation of the surface zeolitic imidazolate framework-67 (ZIF-67) into Ni-Co layered double hydroxides (LDH) and a subsequent annealing process in air, a double-shelled cage-like structure can be obtained with diverse shell compositions.[32] As illustrated in the **Figure 2.6**, the multifunctional hollow structures demonstrate much superior performance compared with one-shelled Co_3O_4 nanocages (NCs) in terms of enhanced capacitance and better cycle life.

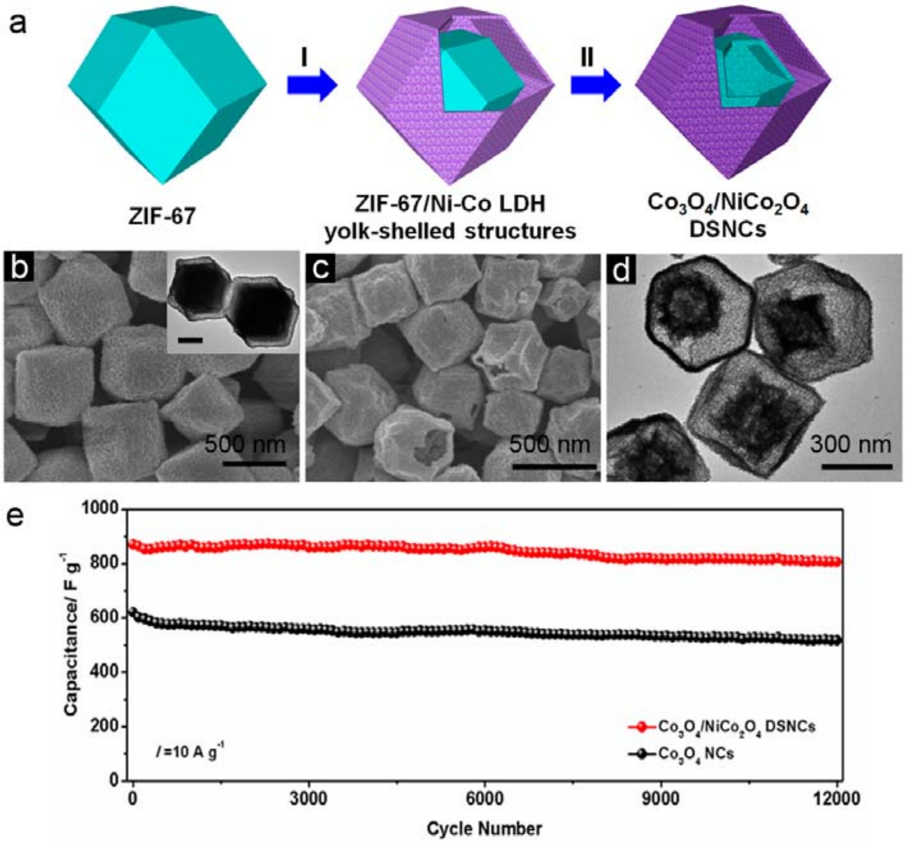

Figure 2.6 (a) Formation process of $Co_3O_4/NiCo_2O_4$ DSNCs from ZIF-67 templates. (b) FESEM image of ZIF-67@Ni-Co LDH. Inset is the TEM image of this yolk-shelled structure; scale bar is 300 nm. (c, d) Morphology characterizations of $Co_3O_4/NiCo_2O_4$ DSNCs. (e) Cycling performance of $Co_3O_4/NiCo_2O_4$ DSNCs and Co_3O_4 NCs.[32] Reproduced with permission from ref. 32. Copyright 2015 ACS.

2.3. Ternary Metal Oxides Nanostructures for LIBs and HSCs

Ternary metal oxides have been studied as promising candidates for LIBs and

HSCs for a long time due to their numerous advantages of environmental benignity, improved conductivity, abundant valence states and new energy storage mechanisms.[44, 59-62] Especially, several groups of spinel oxides like MMn_2O_4 (M=Co), MFe_2O_4 (M=Co), and MCo_2O_4 (M=Ni, Mn, Zn, Cu) have been intensely studied in recent years.[38, 63-65] Compared with the binary metal oxides, the ternary metal oxides present complex chemical compositions with intriguing physicochemical properties owing to the synergetic effects from the two different metal cations. For example, $Mn_xCo_{3-x}O_4$ can store Li^+ based on a redox reaction. To be specific, the metal oxides (MnO and CoO) can react with Li to generate to metallic (Mn and Co) nanoparticles and Li_2O during lithiation process. After delithiation, the metallic crystals can be oxidized to the original oxidation states, leading to high reversible theoretical capacities than those of commercial carbonaceous materials (372 mAh g^{-1}) as anode materials.[35, 66] Meanwhile, Zn-based spinel materials such as $ZnCo_2O_4$, $ZnFe_2O_4$ and $ZnMn_2O_4$ exhibits additional capacity from the reversible formation of alloys between Li and Zn.[33, 39, 61] Another interesting spinel material, $NiCo_2O_4$, stands out because of its fantastic electrical conductivity. According to the former reports, the conductivity is at least two orders of magnitude higher than those of binary nickel oxide (NiO) and cobalt oxide (Co_3O_4), which is rather critical to the remarkable electrochemical performance.[67, 68]

However, it was not until recently that researchers focus on the studies of the morphologies and nanostructure of ternary metal oxide systems and relationship between the nanostructure and the electrochemical activity in LIBs and HSCs.

According to the previous reports, the nanostructuring strategies for the ternary metal oxides can be generally divided into three categories: (I) low-dimensional (1D, 2D) nanostructures; (II) three-dimensional (3D) hierarchical nanostructures; (III) hollow nanostructures. In the following Sections, we will review the recent development about these nanostructured ternary metal oxides for the EES.

2.3.1. Low-Dimensional Nanostructured Ternary Metal Oxides

Low-dimensional nanostructures including 1D systems (nanorod, nanobelt, nanowire) and 2D systems (nanosheet/nanoflake) have attracted extensive interest due to their special functional properties such as splendid electroconductivity and high surface area. Various methods have been developed to obtain the low-dimensional ternary metal oxides with encouraging electrochemical results. For instance, Kim *et al.* prepared one-dimensional $ZnMn_2O_4$ nanowires by a solid-state reaction of α-MnO_2 nanowires and $Zn(CH_3COO)_2$ and investigated them as anode materials in LIBs.[33] Due to the enhanced kinetics of the nanowire, as-obtained $ZnMn_2O_4$ electrode can store and release Li^+ ions reversibly with a high specific capacity. Besides the template method, Wang's group reported a template-free cetyltrimethylammonium bromide (CTAB) assisted method to obtain the porous hexagonal $NiCo_2O_4$ nanoplates.[34] Benefitting from the unique 2D structure with plenty of active sites, the plate-like structures exhibit decent electrochemical performance as electrode for HSCs in 1M KOH solution.

2.3.2. Three-Dimensional Hierarchical Nanostructures

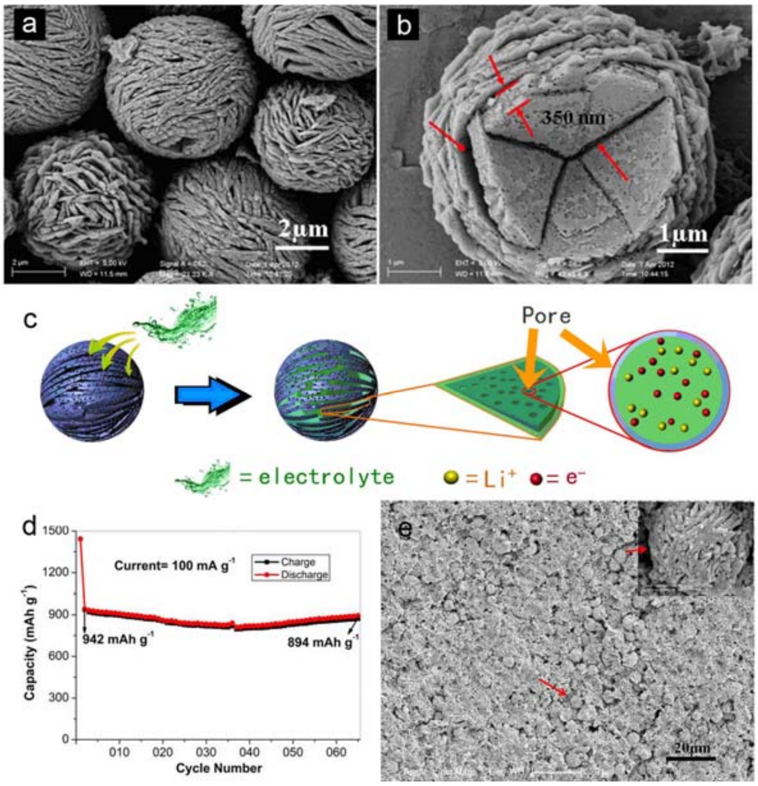

Figure 2.7 (a, b) SEM and TEM images of the mesoporous $CoMn_2O_4$ spheres constructed by 2D nanosheets. (d, e) Illustration for the diffusion of electrolyte and ions. (e) Long-term cycling test and morphological study of the cycled $CoMn_2O_4$ sample.[35] Reproduced with permission from ref. 35. Copyright 2012 Nature Publishing Group.

Although the low-dimensional nanostructures have unique functionalities, they usually suffer from low thermodynamic stability, surface side-reactions, and high cost for the synthesis. Meanwhile, the staggering developments in three-dimensional (3D) hierarchical nanostructures offer a great opportunity to improve the performance of electrode for EES system. As we mentioned in Chapter 2.2.1, 3D hierarchical nanostructures can effectively maintain the structural advantages and restrain shortcomings of the low-dimensional subunits. Also, the void space within the 3D architectures can be beneficial to address volume stress during the discharge/charge process. As shown **Figure 2.7**, Chen's group highlighted the synthesis of hierarchical $CoMn_2O_4$ microspheres assembled by 2D nanoflakes through a facile polyethylene glycol (PEG) assisted solvothermal method.[69] The flake-like porous structure with higher surface area can contribute to faster ionic transport in the electrodes and sufficient contact area with the electrolyte. When applied as LIBs electrode, the hierarchical spheres give a high specific capacity of 894 mAh g^{-1} over 60 cycles at the current density of 100 mA g^{-1}. As demonstrated by the FESEM image of electrode after cycles, the morphology of spheres can survive after the long-tern convention reaction, leading to great cycling stability. Yuan and coworkers synthesized mesoporous ultra-layered $NiCo_2O_4$ nanostructures with large surface area on a large scale through a solution-based method (**Figure 2.8**).[36] The hierarchical 1D structure is constructed from ultra-layered subunits with porous features. The wire-like structure with higher surface area can contribute to faster ionic transport in the electrodes and low internal resistance, giving rise to higher specific capacitance and excellent long-term electrochemical stability.

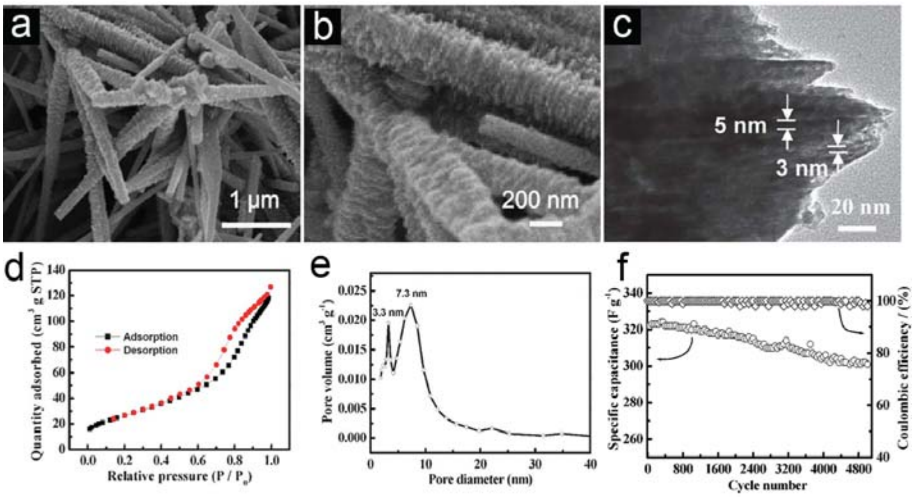

Figure 2.8 (a-c) SEM and TEM images of the mesoporous $NiCo_2O_4$ ultra-layered structures. (d, e) Porous analysis of ultra-layered $NiCo_2O_4$. (f) Long-term cycling test

for the mesoporous $NiCo_2O_4$ structures.[36] Reproduced with permission from ref. 36. Copyright 2014 RSC.

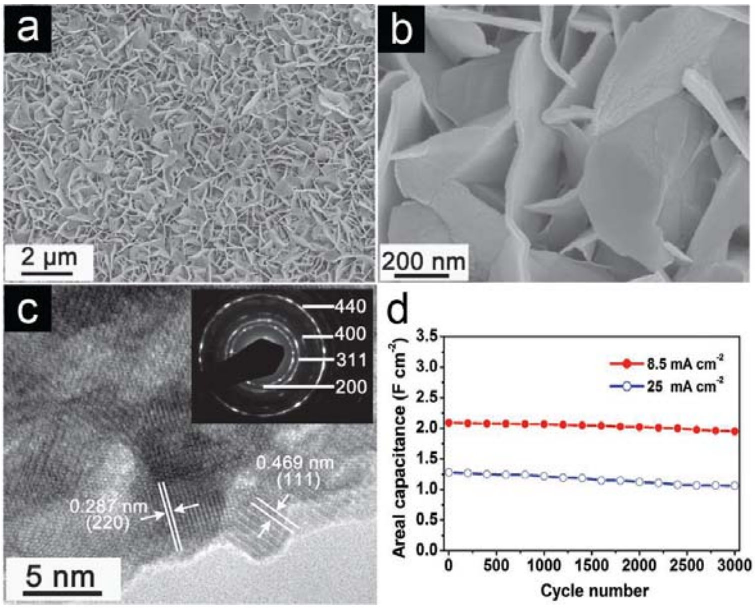

Figure 2.9 (a-c) Morphology characterizations of annealed $NiCo_2O_4$ nanosheets on conductive matrix. (d) The cycling performance of the binder-free $NiCo_2O_4$ electrode at two different current densities of 8.5 and 25 mA cm^{-2}.[37] Reproduced with permission from ref. 37. Copyright 2013 Wiley.

Meanwhile, the construction of integrated 3D structures without binder is as another attractive structure to improve the performance of electrode owing to their more electrochemical active sites, enhanced weight fraction of active materials and better current transport. For example, our group developed a hexamethylenetetramine (HMT) assisted precipitation reaction to develop mesoporous $NiCo_2O_4$ nanosheets. This versatile strategy can be applied to grow the sheet-like structures on four diverse conductive matrixes without obvious topography changes (**Figure 2.9**).[37] This distinctive configuration might have intriguing structure features for high-performance HSCs. Firstly, the mesoporous $NiCo_2O_4$ nanosheets largely improve the electroactive sites. Secondly, the highly porous structure with good mechanical adhesion to the substrate facilitates transport of the electrolyte and serves as the direct current collector. When applied as binder-free electrode, these integrated structures deliver superior specific capacitance with good rate stability at different charge/discharge current densities from 1.8 to 48.6 mA cm^{-2}.

Compared with the planar substrate, 3D conductive matrix such as carbon cloth can be used to further improve the loading mass of active material and rate performance, thus maximizing the volumetric capacity/capacitance. As reported by Shen's group, a 3D system composed of $ZnCo_2O_4$ nanowire arrays on carbon cloth matrix have been developed via a simple hydrothermal method (**Figure 2.10**).[38] Due to the structural merits such as good electronic conductivity from carbon cloth and large electrolyte/$ZnCo_2O_4$ contact area ensured by the 3D configuration, when applied as a highly flexible full battery, the $ZnCo_2O_4$ nanowire arrays/carbon cloth display wonderful performances considering their larger capacity and improved rate capability. More importantly, the hybrid system keeps good cycling performance at 0.2 C.

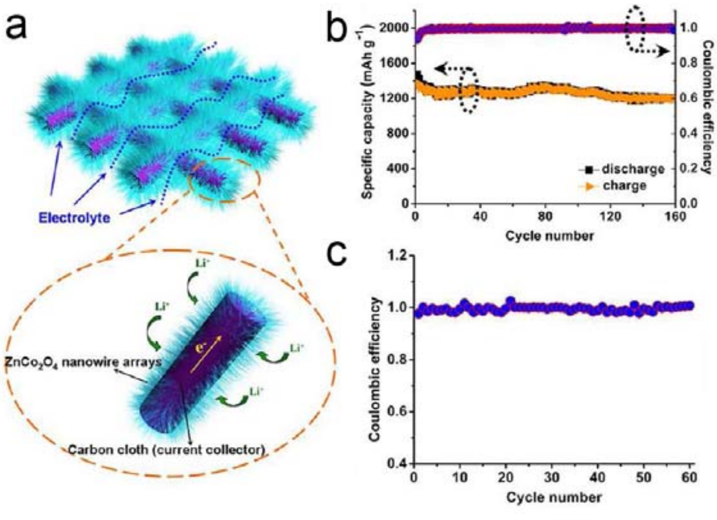

Figure 2.10 (a) Schematic of the $ZnCo_2O_4$ nanowire arrays/carbon cloth and the demonstration of the lithium storage process. (b) Long-term cycling performance over

160 cycles. (c) Rate performance at different charging current densities.[38] Reproduced with permission from ref. 38. Copyright 2012 ACS.

2.3.3. Hollow Structured Ternary Metal Oxides

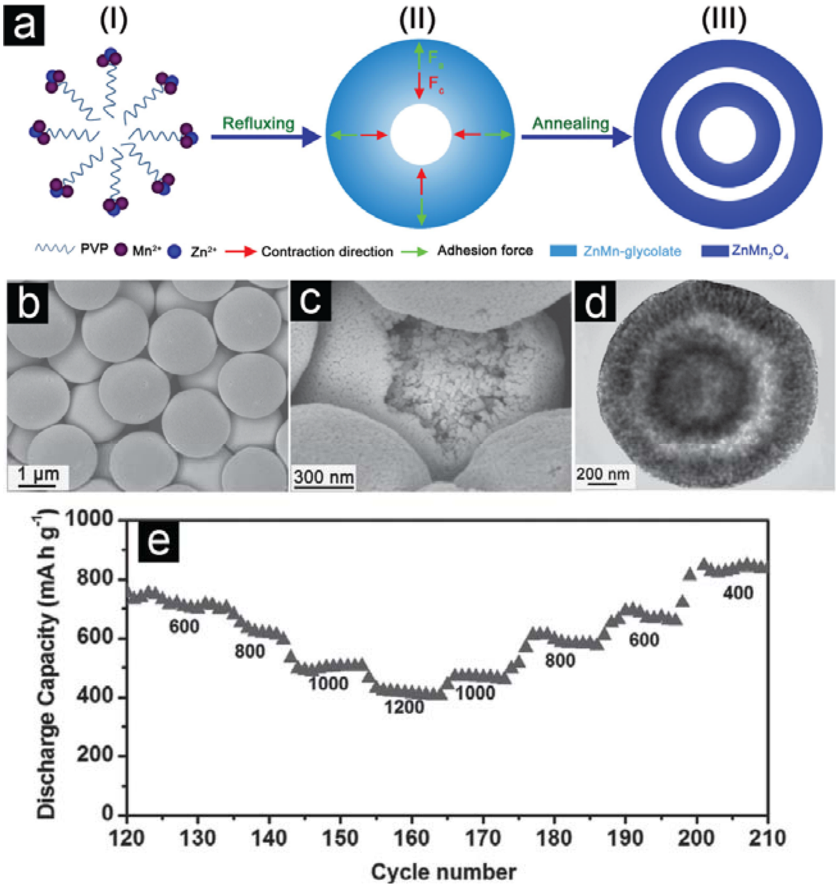

Figure 2.11 (a) Formation mechanism of $ZnMn_2O_4$ ball-in-ball configuration. (b-d) FESEM and TEM images of double-shelled $ZnMn_2O_4$ hollow microspheres. (e) Rate performance of the ball-in-ball structures tested after 120 cycles at 400 mA g^{-1}. The unit of current densities is mA g^{-1}.[40] Reproduced with permission from ref. 40. Copyright 2012 Wiley.

Considering the great success of hollow architectures using simple binary metal oxides for EES applications, we can look forward their great achievement in the ternary metal oxide systems. For example, Chen and coworkers report the synthesis of $ZnFe_2O_4$/C hollow spheres through a one-pot solvothermal method.[39] The formation mechanism of uniform hollow interior can be explained through the well-known "Ostwald ripening process". When tested as anode material for LIBs, the hollow structure has a high specific capacity with good retention. Our group has proposed a protocol for the fabrication of novel ball-in-ball $ZnMn_2O_4$ hollow microspheres via a facile co-precipitation and annealing treatment.[40] As shown in **Figure 2.11**, the forming process of the ball-in-ball architecture could be deduced to a combined result of the contraction and adhesion forces. During the annealing treatment in air, the large amount of organic species in the precursor will be decomposed to create the contraction force, which can tear the metal glycerates hollow spheres into double-shelled structure. Benefitting from the unique ball-in-ball structure, the enhanced lithium storage properties of the double-shelled $ZnMn_2O_4$ spheres can be expected. Specially, the nanosized subunits of $ZnMn_2O_4$ could largely shorten the diffusion length of Li^+ ions, and the hollow interior provide enough space to address the volume expansion during the conversion reaction. In addition, the double-shelled configuration provides much higher volumetric energies than single-shelled structures. According to the electrochemical data for LIBs, these distinctive ball-in-ball $ZnMn_2O_4$ spheres show splendid rate performance and good capacity retention after 120 cycles. As for the HSCs area, Chen *et al.* highlighted the synthesis of 1D hollow tubulars with complex inner architectures for various mixed metal oxide through controllable single-spinneret electrospinning technique.[41] The morphology of these unique structures can be tuned from solid to tube or tube-in-tube architectures through the adjustment of parameters in annealing procedure. Thanks to advantageous configurations, the $NiCo_2O_4$ tube-in-tube structures show superior electrochemical performance in HSCs.

2.4. Summary

A detailed literature survey reveals that advanced architectures of complex metal oxides can be very promising as the electrode materials. Engineering the structure and composition of the complex metal oxides has been demonstrated as an effective and practically feasible approach to fully realize the excellent electrochemical properties of such fascinating materials. Specially, the utilization of micro-/nanostructures, complex hollow structures and hybrid configuration shows many attractive structural merits as smart materials for LIBs and HSCs. Although some encouraging advances have already achieved, the research related to nanostructured complex electrode materials for LIBs and HSCs is still at the early stage and room for improvement remains. More advanced design for the electrode structures is required to meet the ever-growing demand of future EES devices with high energy density merit as batteries along with the high power density feature as supercapacitors. The persistent efforts are necessary to find out the inherent relationship between the enhanced performance and the well-designed architectures to for the future electrode design using nanostructured complex metal oxides.

Chapter 3. Experimental Section

3.1. Synthesis Methodology

3.1.1. Anodization Method

Anodization approach is a classical method to fabricate nanotube arrays, especially for the preparation of anodic aluminum oxide (AAO) membrane and titanium dioxide nanotube arrays (TNAs). The tube length and surface roughness can be further adjusted through the control of electrolysis conditions. By choosing fluoride ions contained organic electrolyte, long-length TNAs with smooth surface can be obtained.

3.1.2. Hydrothermal/Solvothermal Method

Hydrothermal/solvothermal method is a widely used strategy to obtain various kinds of precursors in this project. By meticulous management of the experimental parameters such as type of solvents, concentration of reactants, precipitation agents, molar ratio of metal cations, the size and morphology of final precursors can be further controlled. After annealing treatment in air, well-defined complex metal oxides with distinctive features can be fabricated.

3.2. Materials Characterizations

3.2.1. Morphology Analysis

The morphologies of the samples were taken on field-emission scanning electron microscope (FESEM; JEOL, JSM-7600F/ JSM-6700F, 5 kV) and transmission electron microscope (TEM; JEOL, JEM-2010/JEM-2100F, 200 kV).

3.2.2. Crystallography and Composition Analysis

The crystal structures of the samples were examined by X-ray powder diffraction (XRD) with a Bruker D2 phaser at a voltage of 30 kV and a current of 10 mA. Elemental composition was analyzed with energy-dispersive X-ray spectroscopy (EDX) attached to the FESEM. High-angle annular dark-field STEM (HAADF-STEM) and elemental mapping images were acquired using energy-dispersive X-ray spectroscopy attached to JEM-2100F. The inductively coupled plasma (ICP) optical emission spectroscopy was recorded by a Perkin-Elmer ICP Optima 2000DV. X-ray photoelectron spectroscope (XPS) spectra were taken on a VG ESCALAB MKII spectrometer. Thermogravimetric analysis (TGA) was performed with Pyris Diamond TGA at a heating rate of 10 ^{o}C min^{-1} in air.

3.2.3. Porosity Measurement

The nitrogen adsorption-desorption isotherm was measured using Autosorb 6B at liquid-nitrogen temperature.

3.3. Electrochemical Measurements

3.3.1. Electrode Preparation

For the TiO_2@Fe_2O_3, $NiCo_2O_4$@MnO_2 core-shell integrated structures and $Co_xMn_{3-x}O_4$ arrays were directly used as the working electrodes without ancillary binders or conductive agent. For the hierarchical $NiCo_2O_4$ spheres and Ni-Co mixed oxide yolk-shelled prisms, the active materials were mixed with carbon black (super-P-Li), and polymer binder (polyvinylidene difluoride, PVDF) in a weight ratio of 70:20:10 to prepare electrode slurry. Then the slurry was pressed on current collector (Ni foam for the HSCs and Cu foil for LIBs) as the working electrode with a loading mass of the active material about 1 mg cm^{-2}. Before tests, the working electrodes were dried at 120 ^{o}C for 10 h.

3.3.2. Test Conditions

The electrochemical measurements for HSCs electrode were carried out in an aqueous LiOH or KOH electrolyte with a three-electrode cell where a Pt foil served as the counter electrode and the Hg/HgO or saturated calomel electrode (SCE) was used as the reference. The characterization of the electrode material for LIBs was performed using two-electrode Swagelok-type cells with lithium plate as both the counter electrode and reference electrode. The electrolyte was composed of 1.0 M LiPF6 in a 1:1 (V/V) mixture of ethylene carbonate and diethyl carbonate. Cell assembly was carried out in an argon-filled glovebox with concentrations of moisture and oxygen below 1.0 ppm. Galvanostatic charging/discharging and cycling tests were performed using a NEWARE battery tester. Cyclic voltammetry measurements were conducted on a CHI 660C electrochemical workstation. Electrochemical impedance spectroscopy (EIS) measurements were carried out by applying an AC voltage at open circuit potential.

Chapter 4. TiO_2 Nanotube Arrays Grafted with Fe_2O_3 Hollow Nanorods as Integrated Electrodes for Lithium-ion Batteries†

4.1. Introduction

Amongst the available materials for LIBs, iron oxides have been regarded as very attractive substitutes for the graphite material owing to their much higher specific capacity of 900-1000 mAh g^{-1}, harmless, high erosion resistance and enhanced safety.[70-72] Iron oxides are classical conversion-type materials, which could store lithium through reversible conversion reactions to form a Li_2O buffering matrix and reduced metallic nanoparticles during lithiation. Then both of them return to the original states after successive delithiation.[70, 73, 74] The multi-electron redox reactions within the charge-discharge process render iron oxides higher specific capacities than that of the metal oxides which store lithium by addition-type reaction (e.g., TiO_2).[12] The highly reversible formation of Li_2O matrix also not only reduces the irreversible capacity loss, but enhances the structural stability upon electrochemical cycling, resulting in the superior performance over the metal or metal alloy electrodes.[75, 76] Therefore, iron oxides are very promising for lithium storage due to the balanced lithium storage capacities and calendar life.

---

† Reproduced and modified from [L. Yu, Z. Y. Wang, L. Zhang, H. B. Wu, X. W. Lou, *J. Mater. Chem. A* 1, 122-127 (2013)] by permission from *The Royal Society of Chemistry*. Copyright 2013.

The practical performance of bulk iron oxides, however, is far below the expectation as rapid capacity loss is often observed, even at low current densities.[77, 78] One effective approach to prolong the cycling lifespan of iron oxides is to engineer delicate nanostructures. So far, many iron oxide nanostructures from zero-dimensional nanocrystals to complex hybrid architectures have been fabricated and studied as negative electrodes for lithium storage with encouraging results.[42, 79-83] Nevertheless, the synthesis of truly durable iron oxide based electrodes still remains as a significant challenge at this moment.

Herein, we develop a 3D electrode by assembling Fe_2O_3 hollow nanorods onto highly oriented TiO_2 nanotube arrays (TNAs). The TNAs are chosen as the 3D framework for their particular advantages: a) they can be readily synthesized in large scale by common methods such as anodization;[84] b) TiO_2 can also contribute to the lithium storage capacity with negligible lattice change;[26, 45] c) the tubular nanostructure may offer much larger surface area and easier access for the lithium ions than the solid rods or pillars; d) TiO_2 is highly stable in solution to support the growth of iron oxide nanostructures. By combining with Fe_2O_3 hollow nanostructures, the formed TNAs@Fe_2O_3 hierarchical structure can be independently applied as the integrated anode in LIBs without any ancillary additives, for example polymer binder and conductive agents. The TNAs@Fe_2O_3 electrode manifests remarkable lithium storage properties in terms of high areal capacity of around 680 μAh cm^{-2} at a high areal current of 100 μA cm^{-2} and almost 100% capacity retention in 50 cycles.

4.2. Materials Synthesis

4.2.1. Synthesis of TNAs

TiO_2 nanotube arrays were synthesized by two-step electrochemical anodization of titanium foil at room temperature.[85] Prior to anodization, a titanium foil with a thickness of 0.3 mm was successively rinsed with ethanol and deionized (DI) water in an ultrasonic bath for 30 mins. Then it was subjected to potentiostatic anodization for 3 h in a two-electrode electrochemical cell configuration using a platinum foil as the auxiliary electrode. A constant voltage about 60 V was employed for this anodization process and the electrolyte used is 0.12 M NH_4F in a 1:9 (W/W) composite of DI water and ethylene glycol (EG). Afterward, the Ti foil was taken out and ultrasonically cleaned in DI water for a few seconds for the next round of potentiostatic anodization under identical conditions. After reaction, the anodized sample was ultrasonically cleaned in ethanol for several times. After annealed at 400 ^{o}C for 2 h with a ramp rate of 1 ^{o}C min^{-1}, crystalline TNAs on the titanium foil can be obtained.

4.2.2. Growth of FeOOH nanospindles on TNAs (denoted as TNAs@FeOOH)

The growth of FeOOH nanospindles on TNAs was conducted by immersing as-obtained TNAs in 40 mL of aqueous solution of $FeCl_3$ (80 mM) at 80 ^{o}C for 12 h. Then, the final hybrids were washed with DI water and ethanol before being fully dried in air at 60 ^{o}C.

4.2.3. Synthesis of TNAs@Fe_2O_3 hierarchical structure

For the formation of hollow Fe_2O_3 nanorods on the TNAs, the TNAs@FeOOH hierarchical structure was annealed in air at 400 °C for 2 h with a slow ramp rate of 1 °C min^{-1}. As a reference, pure Fe_2O_3 powder from the reaction solution was also collected and annealed under the same conditions.

4.3. Results and Discussion

4.3.1. Formation of TNAs@Fe_2O_3 Arrays and Material Characterizations

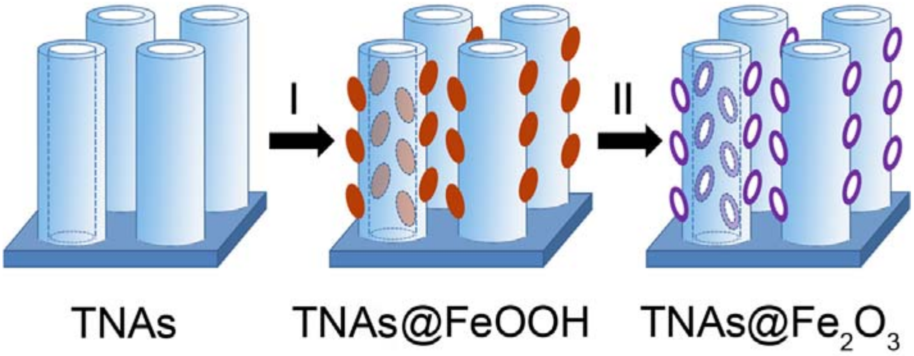

Figure 4.1 Formation of Fe_2O_3 hollow nanorods on TiO_2 nanotube arrays (TNAs): (I) introduction of FeOOH nanospindles onto TNAs through a facile hydrolysis process; (II) annealing treatment of FeOOH nanospindles to Fe_2O_3 hollow nanorods on TNAs (TNAs@Fe_2O_3).

The synthesis process of Fe_2O_3 hollow nanorods on TNAs is straightforward, as schematically illustrated in **Figure 4.1**. Well-oriented TNAs are firstly synthesized as the nanostructured 3D substrate by anodization treatment on a titanium foil at room temperature. Then β-FeOOH nanospindles are voluntarily formed on both the external and internal surface of TNAs through the direct hydrolysis of Fe^{3+} ions at moderate conditions. Due to the good material compatibility, surface pre-treatment is not required for the growth of FeOOH on TiO_2, which greatly simplify the process for the synthesis. Secondly, β-FeOOH nanospindles grafted on TNAs can be easily changed to α-Fe_2O_3 hollow nanorods due to the thermal dehydroxylation and synchronous lattice shrinkage at high temperature, leading to the formation of heterostructures composed of α-Fe_2O_3 hollow nanorods on TNAs.[86]

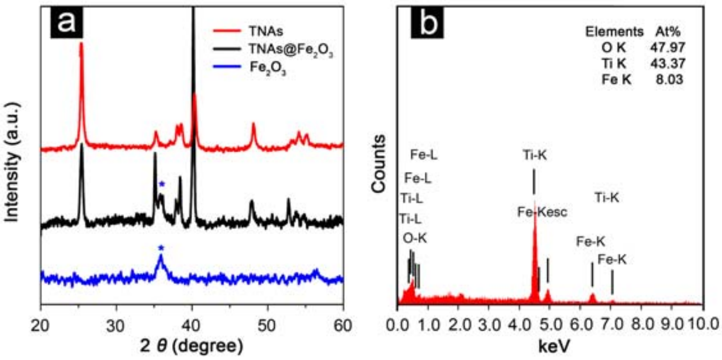

Figure 4.2 (a) XRD patterns of TNAs@Fe_2O_3, TNAs and Fe_2O_3; (b) EDX spectrum of TNAs@Fe_2O_3. The asterisk in (a) indicates the diffraction peak of Fe_2O_3.

The crystallographic structure of TNAs@Fe_2O_3 is examined by X-ray powder diffraction (XRD) analysis, as displayed in **Figure 4.2**a. The XRD spectrum of TNAs confirms the structure of the TiO_2 nanotubes to be anatase TiO_2 (JCPDS Card No. 21-1272) and the existence of titanium (JCPDS Card No. 44-1294). Compared to the TNAs, although the signals of Fe_2O_3 are rather weak, it is obvious that one major diffraction peak indexed to (110) plane of hexagonal α-Fe_2O_3 (hematite, JCPDS Card No. 33-0664) can be observed at around 35^o in the TNAs@Fe_2O_3 hybrid structure. Energy dispersive X-ray (EDX) spectroscopy demonstrates the presence of Fe element with a relatively small atomic concentration of around 8 %, as shown in

Figure 4.2b.

The morphological characteristics of the TNAs and TNAs@Fe_2O_3 are characterized with FESEM and TEM. A panoramic FESEM image demonstrates that the TNAs consist entirely of the dense array of uniform nanotubes without aggregated particles at the surface (**Figure 4.3**a). These TiO_2 nanotubes have an average length of as long as 10 μm with a uniform diameter of around 160 nm, corresponding to a high aspect ratio of around 100 (Figure 4.3b). After the reaction in $FeCl_3$ solution, the surface of TNAs is covered with large quantities of FeOOH nanospindles as a result of the hydrolysis of Fe^{3+} and simultaneously complex growth of FeOOH on TiO_2 nanotubes, as displayed in Figure 4.3c-e. Benefited from the precisely controlled reaction, the FeOOH nanospindles have a length of less than 60 nm, enabling their growth inside the TiO_2 nanotubes. In this process, the initial concentration of $FeCl_3$ in the reaction system is very critical to the formation of FeOOH nanospindles on TNAs. A very low concentration (e.g., 4 mM or 20 mM) results in few FeOOH nanorods on TNAs due to insufficient growth; whereas the excessive amount of $FeCl_3$ (e.g., 160 mM) induces severe homogeneous growth of FeOOH particles (Figure 4.3f-h).

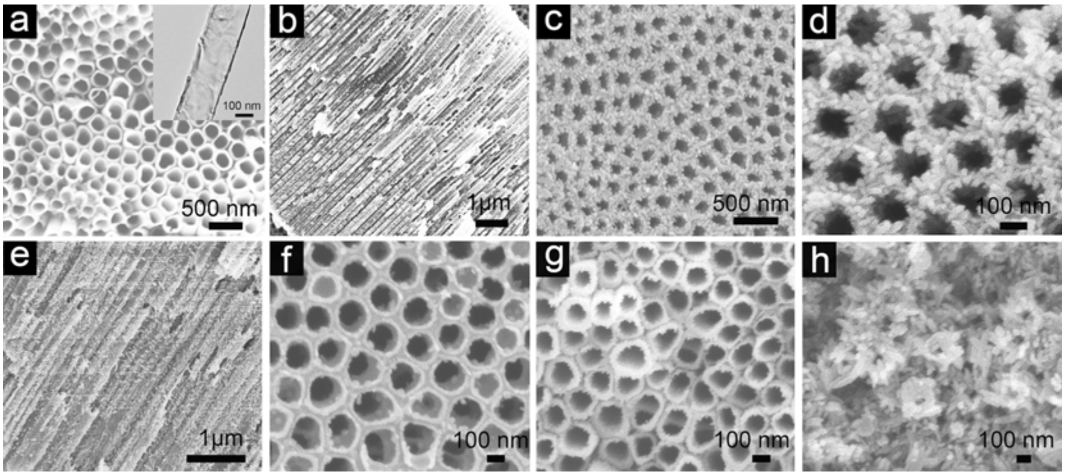

Figure 4.3 (a, b) FESEM images of TNAs, in which the TEM image of a TiO_2 nanotube is shown as the inset in (a); (c, d) top view of TNAs@FeOOH structure; (e) the cross section of TNAs@FeOOH structure; (f-h) the TNAs@FeOOH samples obtained by the hydrolysis of $FeCl_3$ with various concentration of 4 mM, 20 mM and 160 mM, respectively.

TEM analysis is carried out to provide further insight into the detailed structures of the as-prepared samples. It is obvious from the cross-sectional view and top view of TEM observation that highly dispersed FeOOH nanospindles have assembled onto both the outer and inner surface of TNAs without the formation of large particles or aggregates, as shown in **Figure 4.4**a-c. Being in good agreement with the FESEM examination, the FeOOH nanospindles are relatively short with a small diameter of several nanometers. The composition of each component of the TNAs@FeOOH hybrid structure can be changed after a thermal treatment. Via a slow annealing process at 400 °C, TNAs@Fe_2O_3 can be obtained through the dehydroxylation of FeOOH to hollow α-Fe_2O_3 on robust TNAs without obvious structural damage, as shown in Figure 4.4d, e.

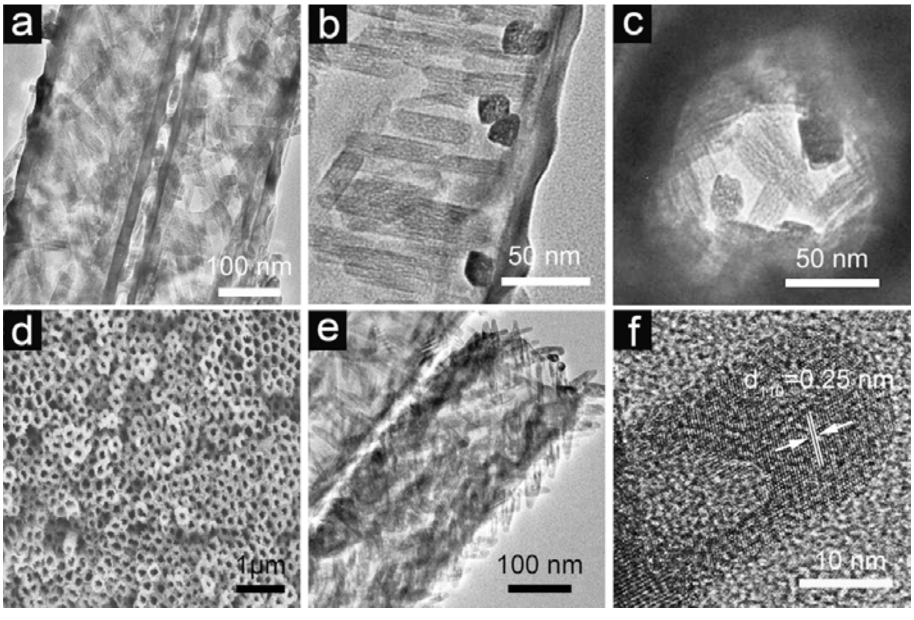

Figure 4.4 (a) TEM images of TNAs@FeOOH structure; (b) several free-standing FeOOH nanospindles on the surface of TiO_2 nanotube; (c) a top-view TEM image showing the formation of FeOOH on the inner and outer surface of TNAs; (d) FESEM and (e, f) TEM images of TNAs@Fe_2O_3 architecture; (f) HRTEM image of Fe_2O_3 nanorod on TNAs@Fe_2O_3 hybrid structure.

After annealing, the hollow interior is generated in the resultant Fe_2O_3 structures because the volume contraction during the phase transition from FeOOH with low density (3 g cm^{-3}) to hematite with a denser density of 5.3 g cm^{-3} (Figure 4.4e). Thanks to the structural similarity of FeOOH nanospindles and Fe_2O_3 nanorods, the hybrid experiences a topotactic transition process, eliminating of the effect of huge mass loss. With high porosity, the Fe_2O_3 hollow nanorods might be beneficial in providing enough interfaces to promote the electrolyte absorption and electrochemical performance on TNAs.[78, 86] Further high resolution TEM (HRTEM) examination on the Fe_2O_3 hollow nanorod is also provided in Figure 4.4f. Consistent with XRD analysis, there is a distinct set of visible lattice fringes in TNAs@Fe_2O_3 with an inter-planar distance of 0.25 nm, which correspond to (110) plane of α-Fe_2O_3. Both the XRD and HRTEM analyses demonstrate the existence of crystalline α-Fe_2O_3 in the TNAs@Fe_2O_3 heterostructures.

4.3.2. Electrochemical Measurements

It is widely accepted that the electrochemical property relies on the inherent crystalline structure, surface functional groups, and integrated states of electroactive substance(s). In TNAs@Fe_2O_3, the electrochemically active TiO_2 nanotube arrays can act as a stable 3D framework to support the growth of Fe_2O_3 hollow nanorods that deliver extra capacity for lithium storage. The unique tubular structure provides open channels for high lithium ion flux across the entire electrode and reduces the internal stress. Due to the individual growth on the TNAs, the Fe_2O_3 nanorods are mostly out of touch from each other, ensuring the enough space for fully contact with lithium ions during the reaction. Compared with the planar nanoparticle-based electrode, the potential agglomeration can be prevented and protect maximized active sites for electrochemical reactions. Meanwhile, the free-standing nanosized nanorods, adequate inter-space between them, and the formation of hollow interiors could efficient address the internal volume stress to enhance the mechanical stability of the electrode. Considering the above structural advantages, we then study the electrochemical performance of TNAs@Fe_2O_3 as a potential anode material in microscale LIBs at ambient temperature.

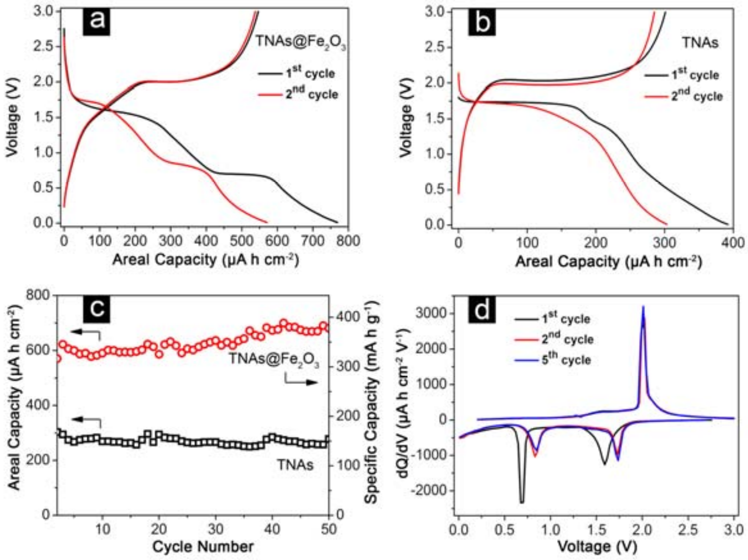

Figure 4.5 Galvanostatic discharge/charge profiles of (a) TNAs@Fe_2O_3 and (b) TNAs for the first two cycles; (c) comparative cycling performances of TNAs@Fe_2O_3 with bare TNAs; (d) the differential capacity versus voltage plots of TNAs@Fe_2O_3. All tests were carried out in the voltage window of 0.05-3.0 V at a current density of 100 μA cm^{-2}.

Figure 4.5a displays the respective discharge/charge voltage curves of TNAs@Fe_2O_3, taken at the current density of 100 μA cm^{-2} within a cut-off voltage window of 0.05-3.0 V. Due to the presence of iron oxides, the TNAs@Fe_2O_3 sample exhibits high initial discharge and charge capacities of 770 and 550 μA h cm^{-2}, respectively; whereas the bare TNAs can only deliver nearly half of the values (Figure 4.5b). The large irreversible capacity fading of 28 % is observed, which is a common phenomenon for most anode materials. The situation can be explained by the inevitable appearance of inorganic solid electrolyte interface (SEI) film and decomposition of the electrolyte. From the 2nd cycle, the areal capacity of TNAs@Fe_2O_3 hierarchical structures increases gradually from 570 μAh cm^{-2} to 680 μAh cm^{-2} within 50 cycles, as shown in Figure 4.5c. This result is superior to most reported TiO_2-based 3D electrodes.[26, 87-89] The specific capacity of TNAs@Fe_2O_3 hierarchical structures is also estimated and revealed by the ordinate at the right side of Figure 4.5c, where it increases gradually with a comparable specific capacity of about 400 mAh g^{-1} at the same current density for 50 cycles. The capacity rise during cycling process is a normal phenomenon for many nanosized metal oxide materials.[78, 90, 91] Firstly, the formation of organic polymeric/gel-like layer around the active materials accompanied by the decomposition of electrolyte can contribute to the extra capacity due to the so-called "pseudo-capacitance-type behaviour".[92] For cobalt and iron oxides, that layer can generate the faint capacity increase step by step along with the cycling process.[78, 90] Besides, the gradually activated active substance might also make a contribution to the extra lithium storage for metal oxide based electrode. With the aim of demonstrating the advantages of TNAs@Fe_2O_3 architectures on the capacity, the electrochemical stability of bare TNAs is also studied by repeated discharge/charge process. The hybrid reveals an initial discharge capacity of 400 μAh cm^{-2}, and maintains at about 300 μAh cm^{-2} after 50 cycles. In addition, the impedance test is also carried out at the open potential for both the TNAs and the hybrid. The results are shown in **Figure 4.6**, the reduced radius of the arc size indicates the faster charge transfer within the composite than the pure TNAs. These inspiring results further demonstrate the superiorities of the TNAs@Fe_2O_3.

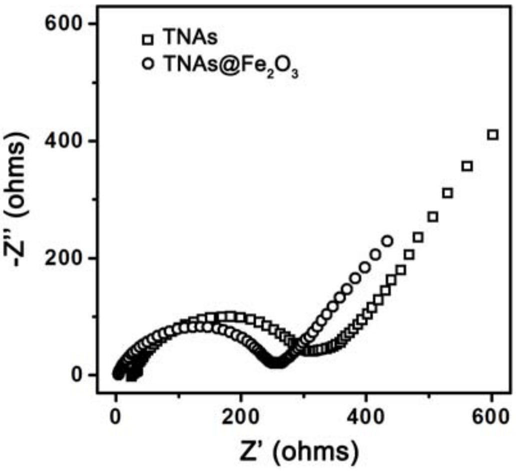

Figure 4.6 Impedance test for TNAs and TNAs@Fe_2O_3 at the open potential.

4.3.3. Lithium Storage Mechanism

In order to further understand lithium storage mechanism within TNAs@Fe_2O_3, the differential capacity versus voltage profiles for the 1st, 2nd and 5th cycles are investigated (Figure 4.5d). During the initial cycle, two peaks at 1.6 V and 0.7 V can be identified, which are related to the insertion of lithium into the Fe_2O_3/TiO_2 and complete reduction of Fe_2O_3 to metallic Fe and SEI film formation, respectively.[93, 94] Another peak at 2.0 V is corresponded to the delithiation of TiO_2 (from orthorhombic Li_xTiO_2 to tetragonal anatase) and the restoration of iron oxides.[88, 95] The subsequent curves show good reproducibility with two cathodic peaks at 0.9 and 1.75 V, and an anodic peak at 2.0 V. The slightly shift of the two cathodic peaks to higher potential is probably due to the possible structural rearrangement, and more facile lithium insertion and redox reactions after the initial cycles, which has also been observed in previous reports.[11, 12, 96] Apparently, the storage mechanism in TNAs@Fe_2O_3 is analogous to that in other iron oxides and TiO_2 electrodes.[88, 90]

4.4. Summary

In summary, a three-dimensional (3D) metal oxide electrode is fabricated by assembling FeOOH nanospindles onto both the inner and outer surface of well-aligned TiO_2 nanotube arrays, followed by thermal conversion to Fe_2O_3 hollow nanorods. The good contact between Fe_2O_3 nanostructures and TiO_2 nanotubes ensures the structural integrity as a binder-free integrated electrode for microscale lithium-ion batteries. Benefitting from the desirable architecture, the core-shelled TiO_2@Fe_2O_3 hybrid can deliver high capacities of over 600 μAh cm^{-2} at a current density of 100 μA cm^{-2} with good cycle life. The lithium storage property is much better compared with most of the reported TiO_2-based 3D electrodes. Clearly, the combination of the 3D nanostructure and electrochemical active metal oxides could be useful for the design of next-generation high-efficiency lithium storage devices.

Chapter 5. Hierarchical $NiCo_2O_4$@MnO_2 Core-shell Heterostructured Nanowire Arrays on Ni Foam as High-performance Supercapacitor Electrodes†

5.1. Introduction

Among the electrode materials for HSCs, ternary $NiCo_2O_4$[37, 65, 67, 97-100] and MnO_2[53, 101] are the two attractive candidates due to various advantages. Particularly, $NiCo_2O_4$ has been reported to own much superior conductivity and richer chemistry compared with simple nickel oxides or cobalt oxides. Recently, individual capacitive performance for each material has been extensively studied. However, only external surface of electroactive substance can be useful to the overall capacitance and the rest part is inactive because of the short diffusion distance (~20 nm) for electrolytes ions, resulting in an unsatisfactory areal specific capacitance (ASC). As we mentioned in Chapter 2, an emerging attractive avenue to solve the above problem is to fabricate integrated structures combined with at least two kinds of active materials on conducting matrix as binder-free arrays because of their numerous structural superiorities. Therefore, it is highly desirable to fabricate well-defined hybrid combined by $NiCo_2O_4$ and MnO_2 and investigate its electrochemical performance of their integrated electrodes to boost ASC.

---

† Reproduced and modified from [L. Yu, G. Q. Zhang, C. Z. Yuan, X. W. Lou, *Chem. Commun.* 49, 137-139] by permission from *The Royal Society of Chemistry*. Copyright 2013.

In this Chapter, we develop a facile method to build heterogeneous arrays on conductive Ni matrix composed of $NiCo_2O_4$@MnO_2 core-shell nanowires as a binder-free cathode for high-efficiency HSCs, where the slim mesoporous $NiCo_2O_4$ NWs as the "core" and ultrathin MnO_2 NFs as the "shell" layer. The smartly designed heterostructured NW arrays on Ni foam own multiple apparent advantages as a HSC electrode: (I) Ultrathin MnO_2 NFs grown on exterior of $NiCo_2O_4$ NW ensure a quick diffusion of electrolyte ions and an enhanced structure stability of the core during repeated electrochemical reactions; (II) the highly conductive $NiCo_2O_4$ NWs can be applied as traffic path for the charge delivery owing to its close contact to the current collector, making full utilization of outer MnO_2 shell, and mesoporous merits provide enough electroactive sites; (III) the outer and inner oxides can react with cations (Li^+) and anions (OH^-) in the electrolyte, respectively, both of which could contribute to the overall capacitance; (IV) the core-shell heterostructured NWs are well separated and strongly contacted with the conductive matrix, preventing the usage of inactive binders and conductive agent and leading to good contact with the electrolyte. Benefitting from synergism of individual component, the fully accessible core-shell arrays exhibit large ASC of 3.31 F cm^{-2}, with remarkable rate stability and long cycle life in a 1 M LiOH solution.

5.2. Materials Synthesis

5.2.1. Synthesis of Ni-Co Precursor Nanowire (NW) Arrays

In a typical synthesis, Ni foam (rectangle shape: 2 cm x 10 cm) was pretreated in acid solution to get rid of the outermost oxidized material. 1.16 g of $Co(NO_3)_2·6H_2O$, 0.58 g of $Ni(NO_3)_2·6H_2O$ and 1.44 g of urea were added in 160 mL of mixed solution with ethanol and DI water (V/V = 1:1) to generate a transparent pink solution at ambient temperature. The solution was moved into a 250 mL bottle, and the pretreated Ni foam was placed in the bottle. Then, the capped bottle was heated to 90 ^{o}C for 8 h in an electric oven. After ultrasonication process to get rid of attachment and dehydration at 60 ^{o}C, the Ni foam with grown precursor was obtained.

5.2.2. Synthesis of $NiCo_2O_4$@MnO_2 core-shell NW Arrays

The Ni-Co precursor arrays were further put into a Teflon-lined stainless steel autoclave (40 mL in volume) with 1.6 mM $KMnO_4$ solution. Then the whole device was heated to at 160 °C and maintained for 30 min. For comparison, 14 and 28 mM $KMnO_4$ solutions were further used to fabricate other $NiCo_2O_4$@MnO_2 core-shell NW arrays. At the end, the integrated hybrid precursor arrays were heated at 350 ^{o}C for 2 h to obtain hierarchical $NiCo_2O_4$@MnO_2 NW arrays on Ni foam. As a control, the $NiCo_2O_4$ NW arrays supported on Ni foam were also obtained after similar heating process without the coating of the MnO_2 shell.

5.3. Results and Discussion

5.3.1. Formation of $NiCo_2O_4$@MnO_2 Arrays and Material Characterizations

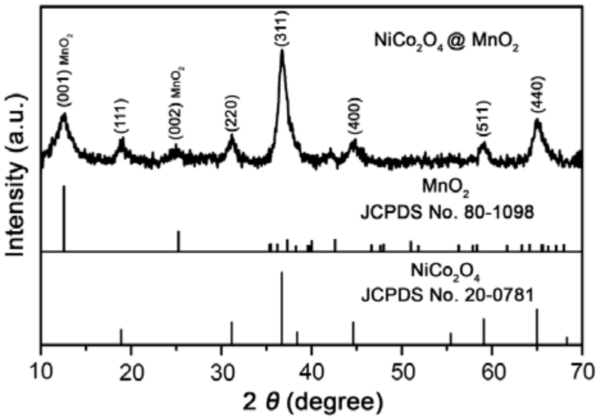

Figure 5.1 XRD pattern of hierarchical $NiCo_2O_4$@MnO_2 NW arrays scratched from current collector.

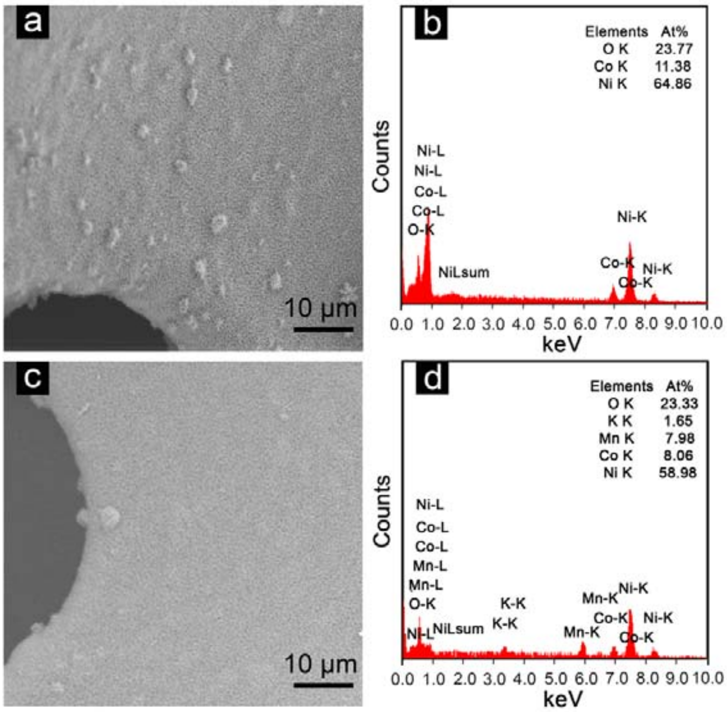

Figure 5.2 Large-scale FESEM images and corresponding EDX data of (a, b) $NiCo_2O_4$ and (c, d) hierarchical hybrid arrays grown on conductive Ni matrix.

Hierarchical $NiCo_2O_4$@MnO_2 core-shell heterostructured NW arrays are synthesized via a solution based strategy together with a subsequent annealing process. To reduce the peak signals of the current collector from the XRD pattern, hierarchical $NiCo_2O_4$@MnO_2 core-shell heterostructured NW powders are scratched from conductive matrix before XRD test. The XRD spectrum (**Figure 5.1**) confirms the existence of the spinel $NiCo_2O_4$ phase (JCPDS Card No. 20-0781) and crystalline birnessite-type MnO_2 (JCPDS Card No. 80-1098). The energy dispersive X-ray spectroscopy (EDX) results (**Figure 5.2**) further verifies the Mn species present in the core-shell arrays.

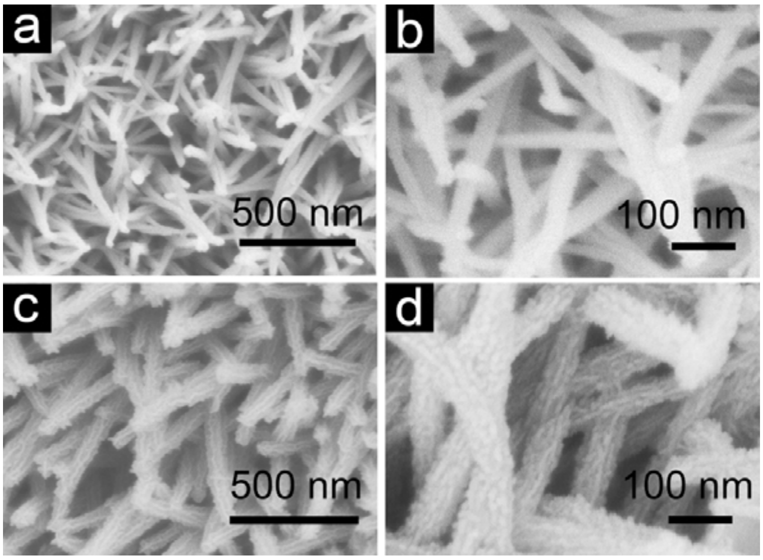

Figure 5.3 FESEM images of (a, b) $NiCo_2O_4$ NW structures and (c, d) hierarchical $NiCo_2O_4$@MnO_2 arrays on conductive Ni matrix.

Figure 5.3a, b demonstrate the top-view FESEM images of the $NiCo_2O_4$ NW arrays grown on conductive nickel matrix. Apparently, the slim $NiCo_2O_4$ NWs with sharp tips are separated from each other, generating a unique array structure with highly porous features. Figure 5.3c, d show the typical FESEM images of final $NiCo_2O_4$@MnO_2 core-shell arrays grown on conductive matrix. Clearly, no MnO_2 is piled up in the void between the NWs, indicating that MnO_2 NFs are selectively deposited on the $NiCo_2O_4$ NWs surface. Thus, the uniform coverage of MnO_2 NFs on each $NiCo_2O_4$ NW surface can be seen. Of importance, even combined with MnO_2 NFs, the wire-like array architecture is well kept and recognizable. Thus, almost all the hierarchical NWs keep good contact with the electrolyte for further faradic redox reaction owing to the ultrathin features of the NW and MnO_2 nanoflake (NF).

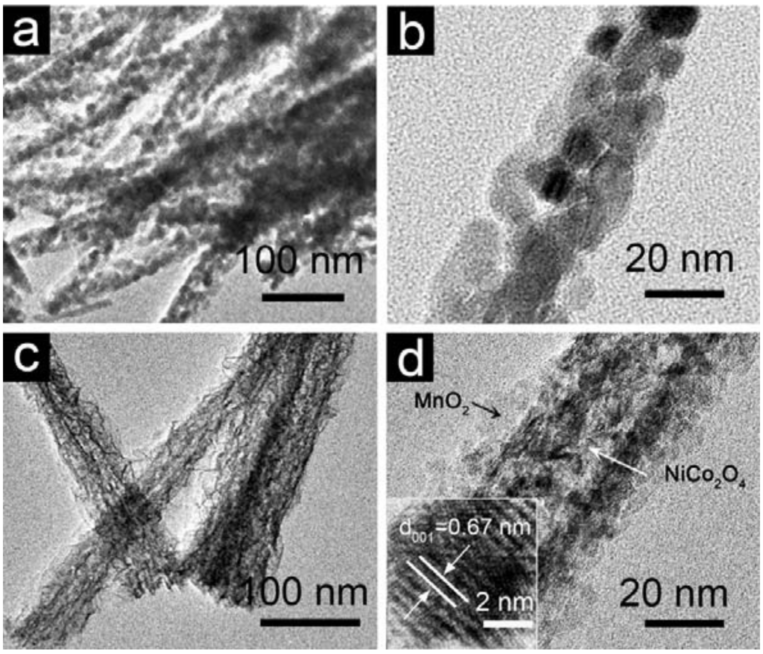

Figure 5.4 TEM images of (a, b) $NiCo_2O_4$ NWs and (c, d) $NiCo_2O_4$@MnO_2 hetero-structures scratched from current collector. Inset in (d) shows the HRTEM image of MnO_2 NFs.

As displayed in the TEM observation of the $NiCo_2O_4$ NWs (**Figure 5.4**a, b), these highly porous needle-like NWs consist of nanosized subunits (about 7-10 nm) with small mesopores (about 3-5 nm). From Figure 5.4c, d, it is obvious that the mesoporous $NiCo_2O_4$ “nanocore” is totally covered with leave-like ultrathin MnO_2 NFs to produce a typical heterostructured core-shell structure. A close observation reveals that the outer symmetric MnO_2 shell layer has a thickness about 10 nm. The high resolution TEM (HRTEM) examination in Figure 5.4d demonstrates that an inter-planar space about 0.67 nm for the apparent pair of lattice fringes, indicating the existence of the (001) plane of birnessite-type MnO_2. Moreover, the thickness of MnO_2 shell can be easily controlled via adjustment of the $KMnO_4$ concentration (**Figure 5.5**). Clearly, when the higher concentration of $KMnO_4$ is used, much thicker MnO_2 layer can be seen. In the case of 14 mM $KMnO_4$, the shell thickness of ultrathin MnO_2 NFs is ca. 50 nm. When the $KMnO_4$ concentration is increased to 28 mM, the thickness of MnO_2 layer increases up to ca. 100 nm.

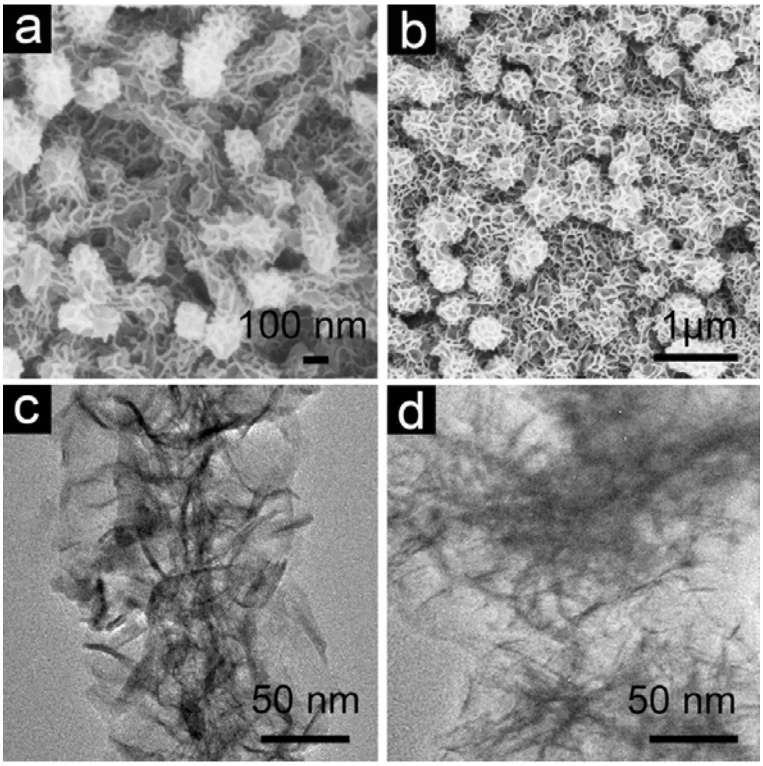

Figure 5.5 FESEM and TEM images of as-fabricated hierarchical $NiCo_2O_4@MnO_2$ core-shell NW arrays grown on conductive matrix by using $KMnO_4$ solutions with different concentrations: (a, c) 14 mM and (b, d) 28 mM.

5.3.2. Electrochemical Measurements

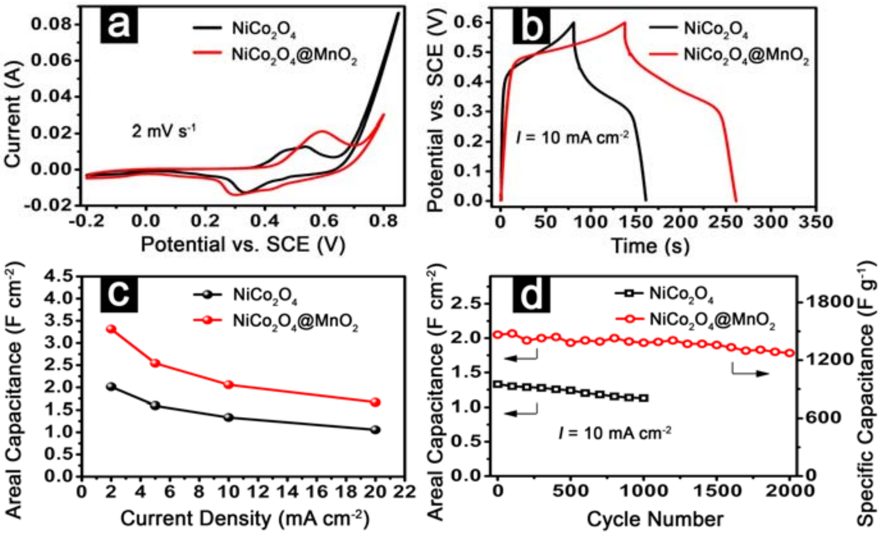

Figure 5.6 (a) CV curves, (b) CP plots, (c) areal capacitances capacitance as a function of current density and (d) capacitance as a function of cycle number for NiCo$_2$O$_4$ NW arrays and heterogeneous arrays on conductive Ni matrix composed of NiCo$_2$O$_4$@MnO$_2$ core-shell NWs.

Next, we directly apply the heterogeneous arrays on conductive Ni matrix composed of NiCo$_2$O$_4$@MnO$_2$ core-shell nanowires as a binder-free electrode to demonstrate the superiorities of the distinctive hybrid with 1 M LiOH as the electrolyte. Cyclic voltammograms (CVs) of the NiCo$_2$O$_4$, and NiCo$_2$O$_4$@MnO$_2$ arrays supported on conductive matrix at a scan rate of 2 mV s^{-1} are shown in **Figure 5.6**a. Two apparent redox peaks can be found for the NiCo$_2$O$_4$ NW arrays electrode, which are derived from the M-O/M-O-OH (M means Ni and Co ions) related Faradaic reactions.[65, 102, 103] Besides, a similar CV geometry can be seen for the core-shell composite arrays, indicating the surface MnO$_2$ NFs don't hinder the utilization of the inner NiCo$_2$O$_4$ NWs in LiOH solution. Meanwhile, the integrated area within the CV curves for the core-shell NW arrays is much larger than that of individual NiCo$_2$O$_4$

arrays, indicating to a much enhanced capacitance. It can be deduced to the additional contribution by the MnO_2 NFs, which would absorb Li^+ cations on the surface of electrode and/or possibly intercalate and deintercalate Li^+ ions.[53] Also, with the scan rates increased up to 50 mV s^{-1}, the CV curves change little (**Figure 5.7**), revealing the excellent high-rate performance of the unique core-shell NW arrays. What's more, the coating of MnO_2 nanoflakes leads to a smaller charge transfer resistance of the hybrid electrode (**Figure 5.8**), which may further enhance the electrochemical performance.

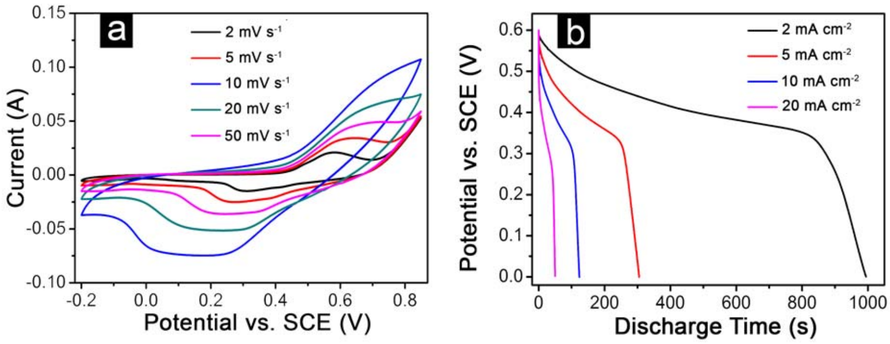

Figure 5.7 Electrochemical performance of the heterogeneous arrays on conductive Ni matrix composed of $NiCo_2O_4@MnO_2$ core-shell nanowires: (a) CVs curves at various scan rates ranging from 2 to 50 mV s^{-1}, (b) CP profiles at different current densities.

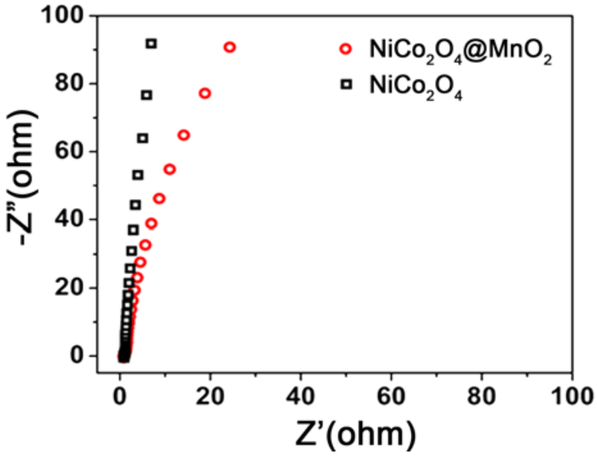

Figure 5.8 Impedance Nyquist plots of the MnO_2, $NiCo_2O_4$ NW arrays and the $NiCo_2O_4$@MnO_2 core-shell arrays grown on conductive matrix at open circuit potential.

Galvanostatic charge-discharge tests are conducted in the 1 M LiOH solution from 0 and 0.6 V (*vs.* SCE) to evaluate the ASC of the individual and hybrid arrays. Evidently, the $NiCo_2O_4$@MnO_2 core-shell NW arrays deliver higher ASC than $NiCo_2O_4$ NW arrays (Figure 5.6b). Also, the ASC results of the core-shell hetero-structures based on the chronopotentiometry (CP) curves (Figure 5.7b) are displayed in Figure 5.6c. Of note, the hetero-structures present higher ASC of 3.31, 2.54, 2.06 and 1.66 F cm^{-2} at current densities of 2, 5, 10 and 20 mA cm^{-2}, respectively, compared to only 2.01 and 1.05 F cm^{-2} at 2 and 20 mA cm^{-2} respectively for the $NiCo_2O_4$ NW arrays. Furthermore, the ASC reported here is much superior compared with those of traditional carbon-based materials,[52] and even better than those of former reported directly-grown battery-like array nanoarchitectures, for examples, NiO-TiO_2 nanotube arrays (3 F cm^{-2} at 0.4 mA cm^{-2}),[104] Co_3O_4-MnO_2 NW/nanosheet core-shell arrays (0.56 F cm^{-2} at 11.25 mA cm^{-2}),[53] Co_3O_4-NiO core-shell NW arrays (1.35 F cm^{-2} at 6 mA cm^{-2}),[100] MnO_2-NiO core-shell NW arrays (0.35 F cm^{-2} at 9.5 mA cm^{-2}),[104] *etc*.. Such good activities at high current densities again demonstrate the superiorities of the $NiCo_2O_4$@MnO_2 core-shell hybrid.

The electrochemical stability of $NiCo_2O_4$@MnO_2 core-shell NW arrays is examined by charging-discharging process. As shown in Figure 5.6d, it is certain that both the capacitance and cycling performance are largely improved for the core-shell NW arrays on conductive Ni matrix. The ASC increase from 1.33 F cm^{-2} in bare

$NiCo_2O_4$ NW arrays to 2.05 F cm^{-2} in core-shell composite on conductive Ni foam. The overall capacitance loss for $NiCo_2O_4$ NW arrays is about 15% after 1000 cycles. Meanwhile, it's only 12% after 2000 cycles for the core-shell NW arrays. The specific capacitance for the core-shell NW arrays is degraded from 1471.4 to 1273.8 F g^{-1} (Right vertical axis, Figure 5.6d). Therefore, the distinct arrays exhibit high electrochemical stability with long-life span at high current densities.

5.4. Summary

In this Chapter, a facile method has been reported to design and build heterogeneous arrays on conductive Ni matrix composed of $NiCo_2O_4$@MnO_2 core-shell nanowires as electrode for hybrid supercapacitors with enhanced performance. The as-fabricated core-shell heterostructured NW arrays electrode delivers high capacitance of 1.66 F cm^{-2} even at 20 mA cm^{-2} and remarkable rate performance and electrochemical stability. Compared with the individual $NiCo_2O_4$ arrays, the electroactivity is largely improved. The inspiring results can be attributed to the special hierarchical core-shell configuration and the combined effects on capacitive contributions from both the mesoporous $NiCo_2O_4$ NW core and the MnO_2 shell layer with ultrathin features. This work reveals the feasibility and advantages of structural design of smart integrated electrodes for high-efficiency hybrid supercapacitors.

Chapter 6. Controlled Synthesis of Hierarchical $Co_xMn_{3-x}O_4$ Micro-/Nanostructures Array as Integrated Electrode for Lithium-ion Batteries[†]

6.1. Introduction

$Co_xMn_{3-x}O_4$ is a potential candidate as electrode materials for next generation of LIBs, benefitting from its superior features inheriting from Co-based and Mn-based metal oxides. Co-based metal oxides such as CoO own almost twice capacity of traditional graphite anode.[105, 106] Meanwhile, Mn-based oxides can operate at lower voltages for lithium extraction. Moreover, manganese element is rich in nature and relatively low cost compared to expensive cobalt species.[40, 107] As mentioned in Chapter 2, complex metal oxides are superior to simple binary oxides owing to the synergistic effect, which could optimize the essential properties of each component.[38, 108-110] Nonetheless, the bulk Co-based and Mn-based metal oxides often suffer from short calendar life and/or poor rate capability.

One of the effective strategies to prolong the cycling lifespan is to adjust the overall size of electroactive substances into the nanometer-scale.[12, 19, 21, 90, 111] Nanosized structures endow the metal oxides with a shortened diffusion length for Li ions and increased specific surface area for good contact with the electrolyte, leading

---

[†] Reproduced and modified from [L. Yu, L. Zhang, H. B. Wu, G. Q. Zhang, X. W. Lou, *Energy Environ. Sci.*, 6, 2664-2671 (2013)] by permission from *The Royal Society of Chemistry*. Copyright 2013.

to enhanced rate capability. However, nanometer-sized particles with high surface energy undergo obvious structural agglomeration during repeated discharge/charge process. Moreover, high surface area has been proved to increase the chance of unnecessary reactions including decomposition of electrolyte, which gives rise to great irreversible capacity and poor cycle performance. In order to address the above question, the usage of micro-/nanostructured electrode configuration has been considered as an elegant avenue. The hierarchical architectures can combine the advantages of nanosized subunits and overall micro-/submicrosized framework, resulting in negligible diffusion time and improved cycling performance.[21, 112, 113] Recently, different research groups have developed hierarchical $Co_xMn_{3-x}O_4$ micro-/nanostructures and applied them as anode materials for LIBs with encouraging results. Chen's group has developed hierarchical $CoMn_2O_4$ microspheres assembled with porous nanosheets, which shows a high discharge capacity of 894 mAh g^{-1} over 65 cycles at a current density of 100 mA g^{-1}.[35] Our group has developed double-shelled $CoMn_2O_4$ hollow microcubes composed of nanometer-sized primary particles which can retain a reversible capacity of 624 mAh g^{-1} over 50 cycles at a current of 200 mA g^{-1}.[63] Xiong and coworkers synthesized the $Mn_{1.5}Co_{1.5}O_4$ core-shell microspheres with a capacity of about of 618 mAh g^{-1} over long-term cycling process (about 300 cycles).[114] Besides, the same group recently fabricated porous $Co_xMn_{3-x}O_4$ spinel quasi-hollow spheres with controlled pore structure and a quasi-hollow interior via an effective solvothermal method. The obtained $MnCo_2O_4$

samples could maintain a specific capacity of 610 mAh g^{-1} with good retention over 100 cycles.[66]

Notwithstanding continuous efforts, the research about hierarchical $Co_xMn_{3-x}O_4$ micro-/nanostructures is quite limited. What's more, current $Co_xMn_{3-x}O_4$ powder materials have to be mixed with highly exothermic polymeric binders and conductivity agents for the electrode preparation, adding undesirable interfaces and redundant weight to the electrode, which inevitably compromises the overall energy storage capacity.[115] To address these obstacle, an emerging strategy is direct growth of active materials with well-defined nanosized architectures on current collector to form as 3D binder-free electrodes with improved energy density for the LIBs.[8, 54, 116, 117] Furthermore, such integrated 3D nanoframes can also be used as the efficient transport channel for electrons.[8] However, up to now, the growth of free-standing $Co_xMn_{3-x}O_4$ materials directly on conductive substrate with well-fined hierarchical structure has not been realized. And thus, it will be highly desirable to study effective and straightforward approaches to directly fabricate hierarchical $Co_xMn_{3-x}O_4$ micro-/nanostructures on conductive substrates for superior lithium storage properties.

Based on the above considerations, we develop a facile solvothermal route to fabricate arrays of Co-Mn precursor based hierarchical structures on stainless steel matrix, and transformed into porous $Co_xMn_{3-x}O_4$ arrays via a post thermal treatment. By rationally controlling the composition of the solvent, the structure of the products can be tailored from hierarchical nanowires to hierarchical nanosheets. Meanwhile, the molar ratio of Co to Mn can be tuned from 2:1 to 1:2 within the final product. The as-formed hierarchical structures of porous $CoMn_2O_4$ nanowires and $MnCo_2O_4$ nanosheets keep good contact with the current collector and therefore they could be directly applied as the electrode without further treatment. Remarkably, the as-synthesized 3D hierarchical structures of $CoMn_2O_4$ nanowires and $MnCo_2O_4$ nanosheets manifest excellent electrochemical performance, making them promising electrodes for LIBs.

6.2 Materials Synthesis

6.2.1. Synthesis of 3D Co-Mn Precursor Arrays On Conductive Substrate

In a typical synthesis, stainless steel foil (rectangle shape: 2 cm x 7 cm) was pretreated in acid solution to get rid of the outermost oxidized material. 1 mmol of $Co(NO_3)_2 \cdot 6H_2O$ and 2 mmol of $MnSO_4 \cdot H_2O$ were added into a mixed solution of 10 mL ethanol and 70 mL DI water generate a transparent pink solution (total volume: 80 mL) at ambient temperature. After that, 12 mmol of urea was dissolved as of additives for hydrolysis of metal salts. The usage of ethanol was further tuned from 0 to 70 mL. The solution was moved into a 250 mL bottle, and the pretreated stainless steel or titanium foil was added. Afterwards, the capped bottle was heated to 90 ^{o}C for 6 h in an electric oven. After ultrasonication process to get rid of attachment and dehydration at 60 ^{o}C, the substrate with grown precursor was obtained.

6.2.2. Synthesis of $Co_xMn_{3-x}O_4$ Hierarchical Arrays as Binder-free Electrode

In order to get crystallized $Co_xMn_{3-x}O_4$ nanostructures, the stainless steel with the precursor hierarchical structures were further heated in air to 600 ºC with a slow ramp rate of 1 ºC min^{-1} and kept at the same temperature for 4 h. In average, the mass loading of the $Co_xMn_{3-x}O_4$ nanostructures is about 0.38 mg on per 1 cm × 1 cm of stainless steel foil, weighted after calcination with caution.

6.3 Results and Discussion

6.3.1. Formation of 3D Co-Mn Precursor Arrays with Controlled Morphologies

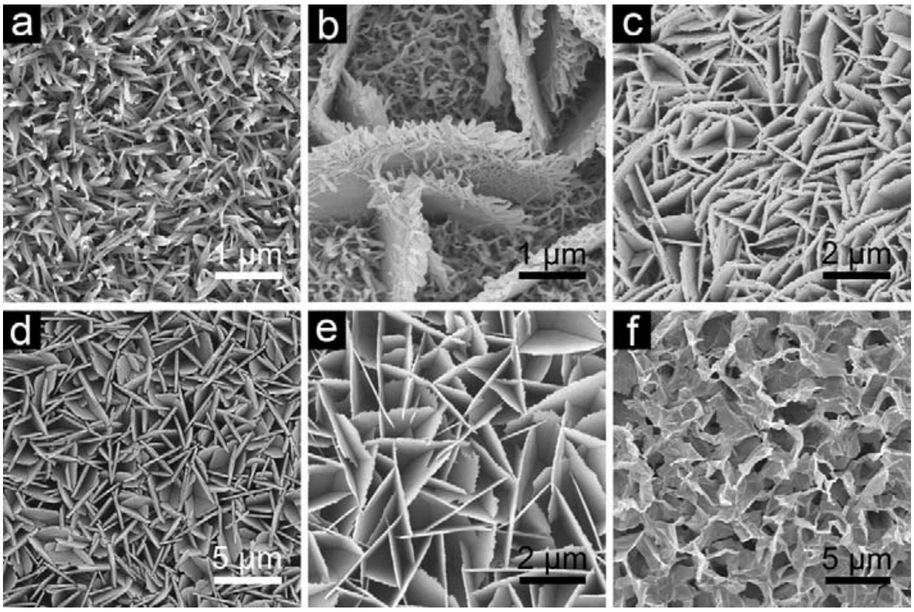

Figure 6.1 FESEM images of $Co_xMn_{3-x}O_4$ precursor based structures grown on stainless steel foil with the change of the volume ratio of ethanol to DI water: (a) CMP-0, $V(EtOH)/V(H_2O) = 0/80$; (b) CMP-30, $V(EtOH)/V(H_2O) = 30/50$; (c) CMP-40, $V(EtOH)/V(H_2O) = 40/40$; (d) CMP-50, $V(EtOH)/V(H_2O) = 50/30$; (e) CMP-60, $V(EtOH)/V(H_2O) = 60/20$ and (f) CMP-70, $V(EtOH)/V(H_2O) = 70/10$.

In our synthesis strategy, two steps are involved: the urea assisted solvothermal route to obtain hierarchical structures on stainless steel substrate composed of Co-Mn precursor (CMP) together with a subsequent annealing process to produce corresponding hierarchical structured $Co_xMn_{3-x}O_4$. The shapes of the Co-Mn precursor are firstly studied by FESEM, as shown in **Figure 6.1**. It is well accepted that polarity of reaction system and solubility of reactants can largely affect the supersaturation for nucleation and crystal growth of product. Therefore, the morphology of Co-Mn precursor nanostructures can be readily controlled by tailoring the volumetric ratio of ethanol/water in the mixed solution.

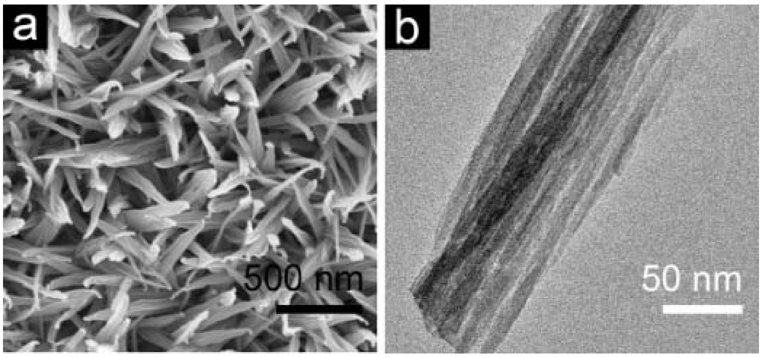

Figure 6.2 (a) FESEM image of CMP-0 nanowires array grown on stainless steel foil and (b) TEM image of an individual CMP-0 nanowire.

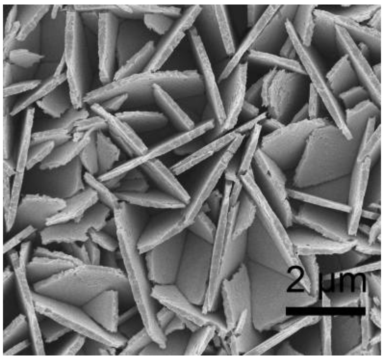

Figure 6.3 FESEM image of CMP-50 nanosheets array grown on stainless steel foil.

For the reaction system of pure DI water, the 1D Co-Mn precursor structures (labeled as CMP-0) with a wire-like shape are vertically introduced on the substrate to generate a uniform array over a large scale. Interesting, from the enlarged top-view and transmission electron microscope (TEM) image of CMP-0 in the **Figure 6.2**, it can be observed that the hierarchical nanowires are composed by secondary bundle subunits with clear texture, diameter of which at the tip is about 50 to 100 nm. The introduction of ethanol leads the formation of huge nanosheet structures vertically on the surface of the substrate. When the volumetric ratio of ethanol/water reaches 30/50, as displayed in Figure 6.1b, nanowires can also be found with some scattered nanosheets on the surface. When the solvent is changed to the mixture combined with equal volume of ethanol and DI water, more stagger nanosheets come up to generate a dense wall-like structure without other impurities (Figure 6.1c). When the usage of ethanol is further increased to 50 mL, the sheet-like structure becomes even larger in size compared to CMP-40, producing an ordered array with a highly open and porous structure (Figure 6.1d). As illustrated in **Figure 6.3**, the nanosheets exhibit a smooth surface with some cracks at the edge, the thickness of which is about 100 nm. Due to the low solubility of $MnSO_4$ in ethanol, less water in the mixed solvent (V/V = 60/20 and 70/10) produces a translucent pink sol instead of a clear solution before reaction. The resulting CMP-60 sample possesses a sheet-like structure with loose connection. Meanwhile, CMP-70 sample owns a nanosheet structure with rippled silk morphology due to its ultrathin feature. X-ray diffraction (XRD) analysis confirms that these Co-Mn precursor nanostructures can be mainly assigned to Co-Mn carbonate or oxide hydrate (**Figure 6.4**). The X-ray diffraction (XRD) pattern for the typical hierarchical nanowires structure, CMP-0, can be assigned to the $Co_{0.33}Mn_{0.67}CO_3$ (JCPDS Card No. 44-1472). Meanwhile, the main phrase of the typical hierarchical nanosheets structure, CMP-50, can be assigned to (Co, Mn)OOH (JCPDS Card No. 30-1022). In order to investigate the role of substrate in the formation of these nanostructures, further experiments have been carried out without the help of stainless steel substrate. Besides, Ti foil has been also applied as the substrate to synthesis these nanostructures with exactly the same reaction conditions. The synthesis of the nanowires and nanosheets precursors are not affected much by Ti foil or in the absence of the substrate. Hierarchical nanowires can still be formed in DI water. Meanwhile, uniform nanosheets structure could also be found in the mixture of ethanol and water. From the results above, we can deduce that the driving force for the variation in morphology of these nanostructures is the alteration of solvent components. The introduction of substrate doesn’t affect the formation of these nanostructures in this case. The stainless steel or Ti foil simply serves as an inert substrate to allow the heterogeneous growth of Co-Mn precursor nanostructures, indicating the versatility of the present system.

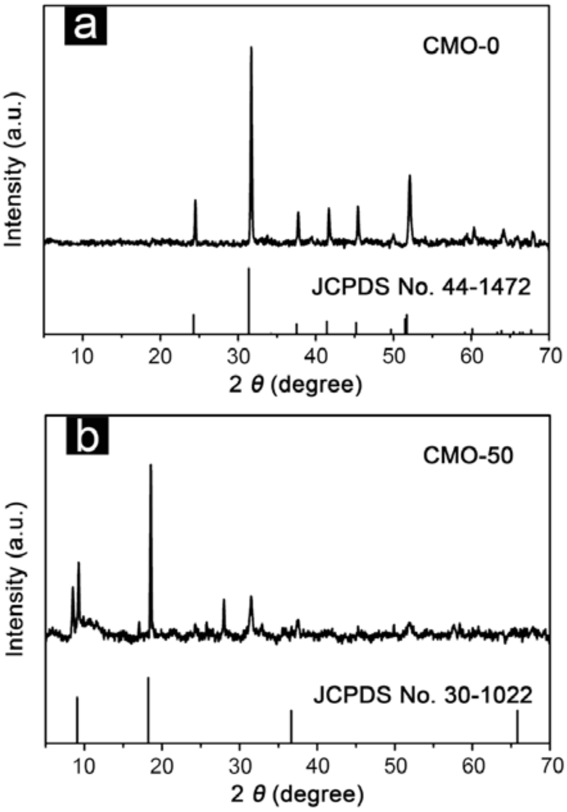

Figure 6.4 XRD patterns of (a) hierarchical nanowires (CMP-0) and (b) nanosheets (CMP-50) scratched from stainless steel foil.

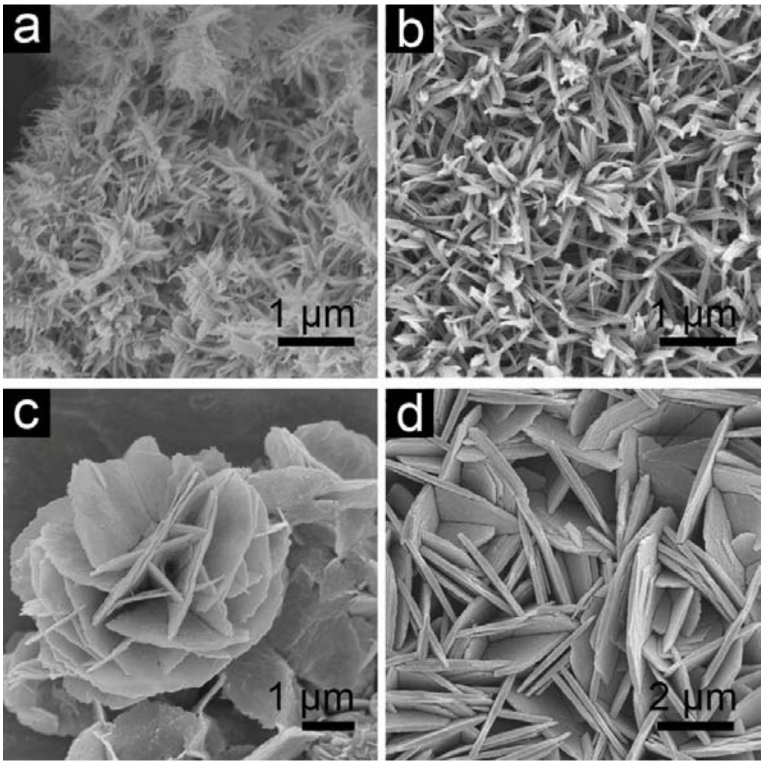

Figure 6.5 FESEM images of Co-Mn precursor structures obtained without substrate (a, c) and on the surface of Ti foil (b, d). The synthesis solvent for (a, b) is water.

Meanwhile, the synthesis solvent for (c, d) is the mixed solvent of EtOH/H_2O (50mL/30mL).

Also, the formation of Co-Mn precursor based hierarchical structures is contributed by both Co and Mn precursor salts (**Figure 6.6**). Without the Mn precursor salts, the resulting Co-based precursors are inhomogeneous needle and sheet combined structures in DI water or pure needle-like nanostructures with smooth surface in complex solvent. In a sharp contrast, the Mn-based precursors can hardly grow on the stainless steel. Only some irregular octahedra-like or bud-like particles can distribute on the surface. We can deduce that Co^{2+} ions may offer contact points between Co-Mn precursor nanostructures and stainless steel to induce anisotropic crystal growth on the substrate.

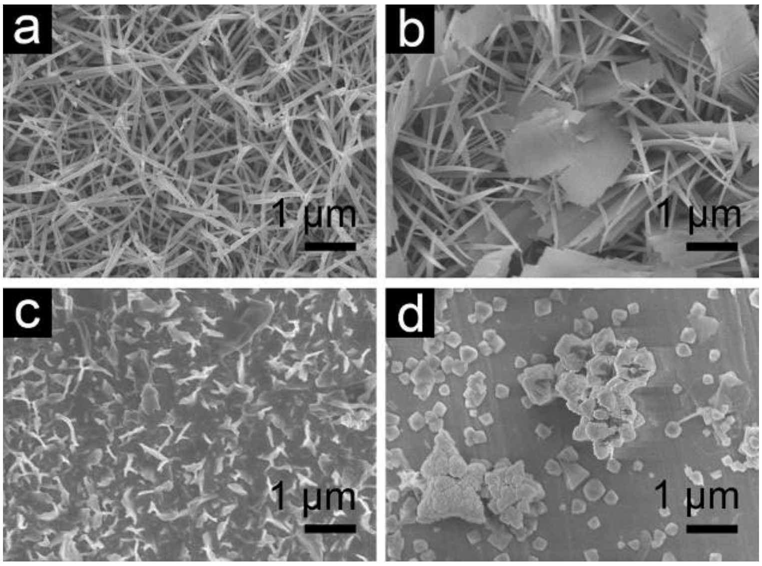

Figure 6.6 FESEM images of Co-related and Mn-related precursor nanostructures grown on stainless steel foil with change of the volume ratio of ethanol to DI water: (a) Co precursor, V(EtOH)/V(H_2O) = 50/30; (b) Co precursor, V(EtOH)/V(H_2O) = 0/80; (c) Mn precursor, V(EtOH)/V(H_2O) = 50/30; (d) Mn precursor, V(EtOH)/V(H_2O) = 0/80.

X-ray photoelectron (XPS) measurement suggests the co-existence of Mn^{2+}/Mn^{3+}

and Co^{2+}/Co^{3+} cations in both the $CoMn_2O_4$ and $MnCo_2O_4$ samples (**Figure 6.7**). To be specific, the Mn 2p spectrum of $CoMn_2O_4$ contains two main spin-orbit lines of $2p_{3/2}$ at 642.2 eV and $2p_{1/2}$ at 653.6 eV. Meanwhile, for the $MnCo_2O_4$, the Mn 2p spectrum also shows two major peaks with binding energies values at 642.0 and 653.5 eV, assigned to the Mn $2p_{3/2}$ and Mn $2p_{1/2}$ peaks, respectively. Both Mn 2p spectra can be assigned to the existence of Mn^{2+} and Mn^{3+} cations.[66] The Co 2p spectra for both $CoMn_2O_4$ and $MnCo_2O_4$ also consist of two spin-orbit doublets and three shakeup satellites (denoted as "Sat."), characteristic of Co^{2+} and Co^{3+} cations.[106]

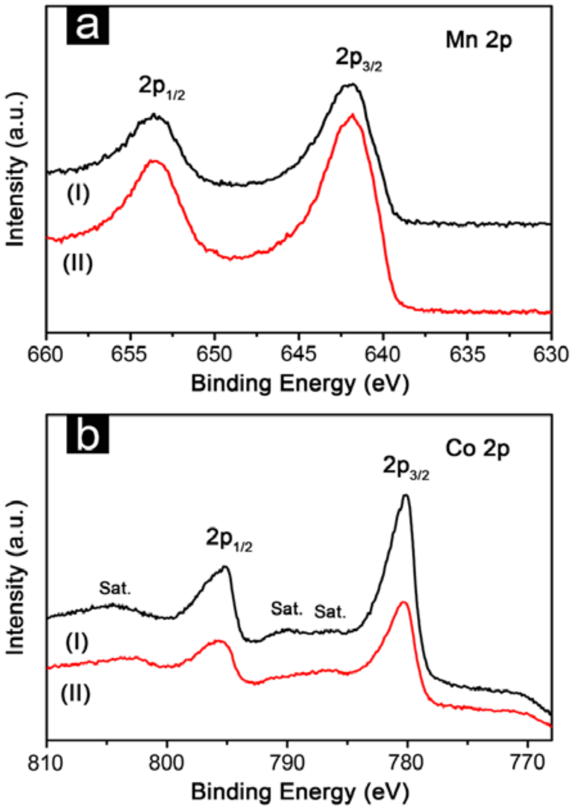

Figure 6.7 XPS spectra of (a) Mn 2p, (b) Co 2p for the hierarchical $CoMn_2O_4$ nanowires (in black line) and $MnCo_2O_4$ nanosheets (in red line) grown on stainless steel foil.

6.3.2. Conversion of Precursors to $Co_xMn_{3-x}O_4$ Micro-/Nanostructures

According to previous study on the related $Co_xMn_{3-x}O_4$ materials, we choose 600 ºC as the calcination temperature for the final composite oxides. For the convenience of the discussion, in this part, two ternary metal oxides from CMP-0 and CMP-50 are involved as the representatives for the hierarchical nanowires and nanosheets. The crystallographic structures of these two products are firstly studied via XRD test (**Figure 6.8**). To reduce the peak signals of the current collector from the XRD pattern, hierarchical $Co_xMn_{3-x}O_4$ structures are scratched from conductive matrix before XRD test. All of the reflections of hierarchical nanowires calcined from CMP-0 could be assigned to body-centered-tetragonal $CoMn_2O_4$ (JCPDS Card No. 77-0471, space group: $I4_1/amd$, $a = b = 5.784$ Å, $c = 9.091$ Å, $\alpha = \beta = \gamma = 90^o$). There is no obvious residues or contaminants can be detected.[109]

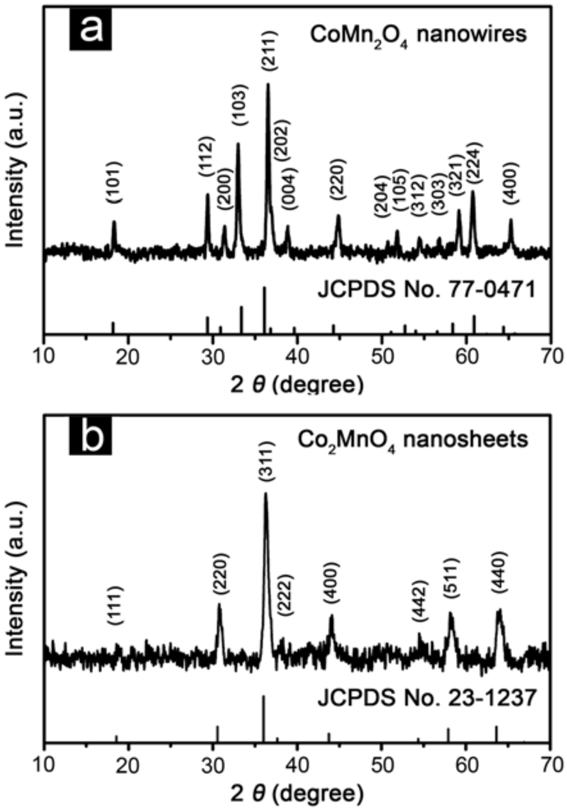

Figure 6.8 XRD patterns of (a) hierarchical $CoMn_2O_4$ nanowires (calcined from CMP-0) and (b) $MnCo_2O_4$ nanosheets (calcined from CMP-50) scratched from stainless steel foil.

The EDX result (**Figure 6.9**) indicates the Co/Mn ratio for the hierarchical nanowires structure is about 0.5, which is close to the theoretical value. Whereas, the XRD pattern for nanosheets structure calcined from CMP-50 confirms the existence of the face-centered-cubic $MnCo_2O_4$ phase (JCPDS Card No. 23-1237, space group: *Fd3m*, $a = b = c = 8.269$ Å, $\alpha = \beta = \gamma = 90^o$). Both the two structures adopt distorted spinel structures, in which manganese and cobalt ions are distributed over octahedral and tetrahedral stacking interstices. The crystallite sizes of $CoMn_2O_4$ and $MnCo_2O_4$ nanostructures determined using the Scherrer equation are about 26.0 nm and 15.5 nm, respectively, which indicates that the $Co_xMn_{3-x}O_4$ samples are composed of nanocrystalline building blocks. Meanwhile, the elemental composition of the nanosheets structure characterized by EDX shows a different atomic Co/Mn ratio of 2/1, although it has the same initial concentration of Co-Mn precursor with CMP-0. We can speculate that Mn^{2+} ion may face more resistance to precipitate compared to Co^{2+} ions when ethanol plays a dominate role in the reaction solvent.

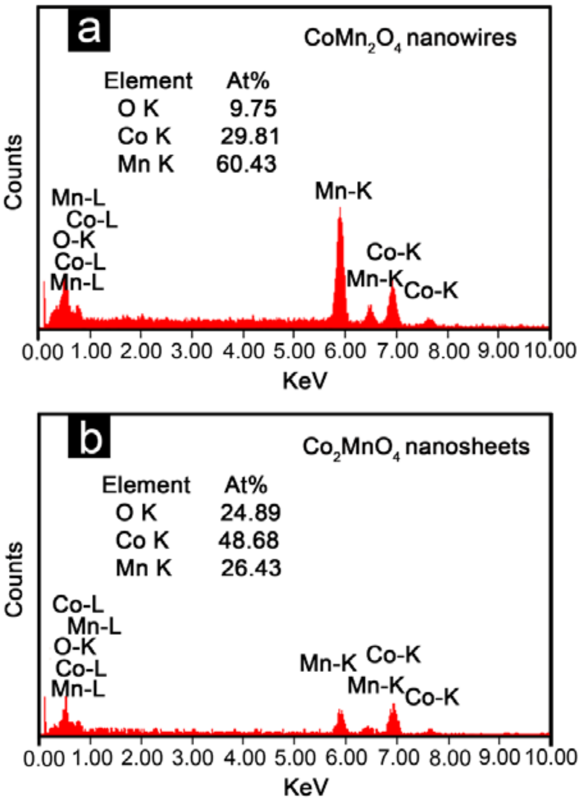

Figure 6.9 EDX spectra of (a) hierarchical CoMn$_2$O$_4$ nanowires and (b) MnCo$_2$O$_4$ nanosheets scratched from stainless steel foil.

FESEM and TEM studies offer further information about the elaborate morphologies of the as-prepared hierarchical structures of Co$_x$Mn$_{3-x}$O$_4$. As depicted in **Figure 6.10**, after thermal process in air with a heating speed of 1 °C min^{-1}, the integral architectures of these Co-Mn precursors can be well inherited within the crystalline Co$_x$Mn$_{3-x}$O$_4$ structures without obvious destruction. The hierarchical CoMn$_2$O$_4$ nanowires exhibit similar one-dimensional features from the precursor with a rougher exterior. As elucidated by TEM observation in Figure 6.10c, each CoMn$_2$O$_4$ nanowire is constructed by many primary particles in nanosize. As determined by N$_2$ sorption measurement at 77 K (**Figure 6.11**), the open pores formed by the arrays and small mesopores among the nanosized subunits endow the hierarchical CoMn$_2$O$_4$ nanowires with a high BET surface area of 70 m^2 g^{-1}, providing enough contact area with electrolyte for the convention reactions with lithium ions. The HRTEM observation in Figure 6.11d demonstrates that an inter-planar space about 0.49 nm for the apparent pair of lattice fringes, indicating the existence of the (101) plane of $CoMn_2O_4$ crystals. Meanwhile, from the FESEM images in Figure 6.11e, the sheet-like morphology of the CMP-50 is perfectly retained during the thermal conversion for the hierarchical $MnCo_2O_4$ nanosheets with a negligible change in size. A more interesting feature is observed from the high-resolution SEM image (Figure 6.11f) and further confirmed by TEM examination (Figure 6.11g), the surface of the product becomes rather rough, indicating the generation of porous structures through annealing treatment. Nonetheless, these porous structures only exhibit relatively low BET surface about 19 m^2 g^{-1}, which is probably due to the large size of the hierarchical $MnCo_2O_4$ nanosheets. The selected-area electron diffraction (SAED) pattern viewed along the <$1\bar{1}1$> zone axis (Figure 6.11h) reveals the single-crystal nature, and also indicates that the dominant exposed surfaces of the synthesized nanosheet are (220) facets.

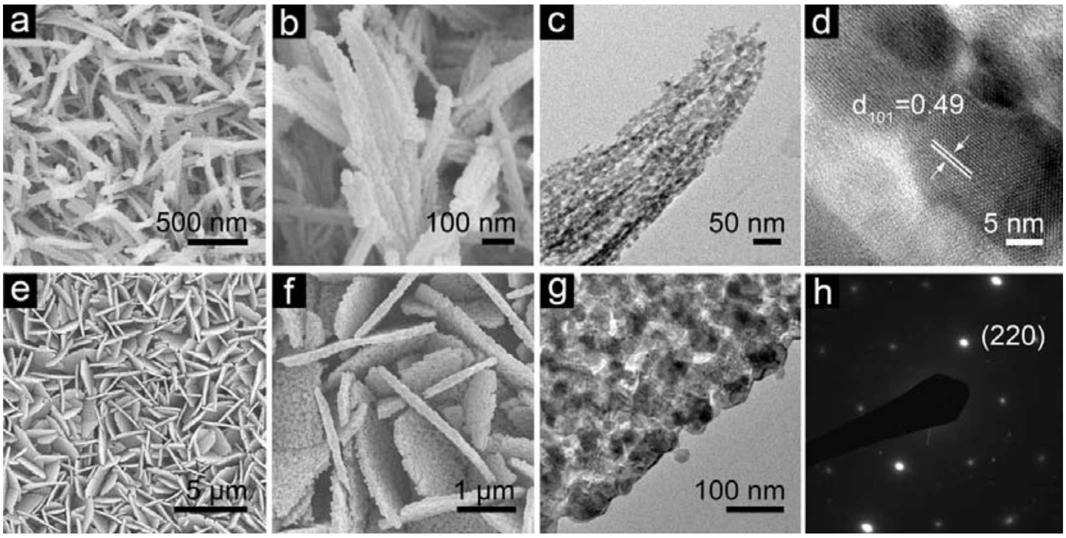

Figure 6.10 SEM and TEM characterization of crystallized $CoMn_2O_4$ nanowires array

and $MnCo_2O_4$ nanosheets array grown on stainless steel foil: (a) top view and (b) partial enlarged view of nanowires array; (c) TEM image of an individual crystallized $CoMn_2O_4$ nanowire. (d) Lattice fringes performed on the nanowire. (e, f) FESEM of hierarchical nanosheets array. (h) TEM image of a dispersed $MnCo_2O_4$ nanosheet and (f) the corresponding SEAD pattern.

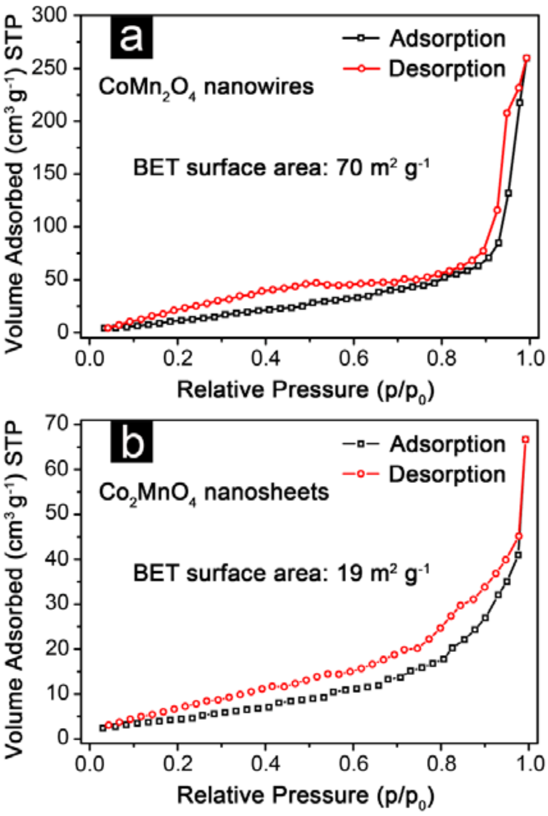

Figure 6.11 N_2 adsorption-desorption isotherm at 77 K of (a) hierarchical $CoMn_2O_4$ nanowires and (b) $MnCo_2O_4$ nanosheets scratched from stainless steel foil.

6.3.3. Electrochemical measurements

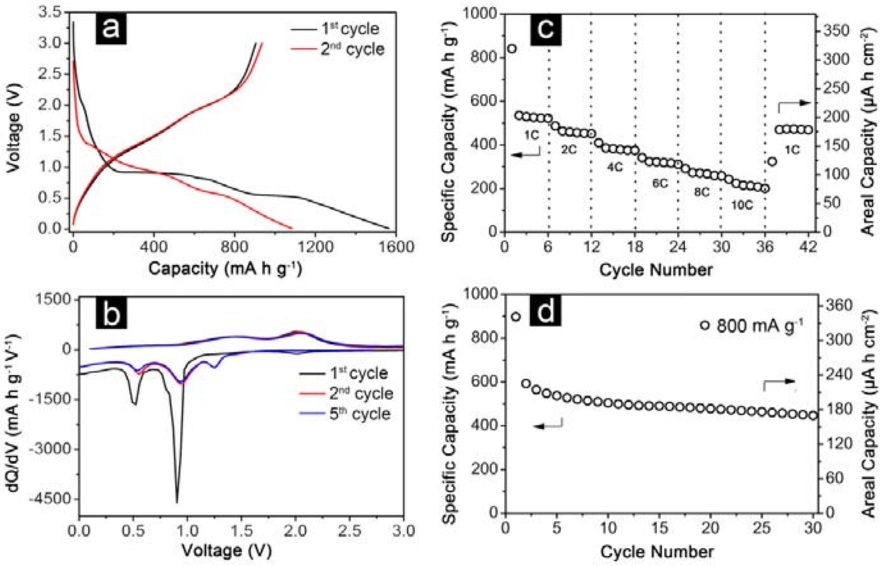

Figure 6.12 Electrochemical properties of hierarchical $CoMn_2O_4$ nanowires array grown on stainless steel foil: (a) galvanostatic discharge/charge curves for the 1st and 2nd cycles; (b) differential capacity *vs.* voltage profiles for the 1st, 2nd and 5th cycles; (c) discharge capacity at various current densities; (d) cycling test a constant current of 800 mA g^{-1}. All tests were conducted in the voltage range of 0.05-3.0 V.

As we mentioned in Chapter 4, the electrochemical property relies on the inherent crystalline structure, surface functional groups, and integrated states of electroactive substance(s). Apparently, the generation of well-defined arrays with tunable morphology is vital to the lithium storage properties of the hierarchical $Co_xMn_{3-x}O_4$ micro-/nanostructures. The direct growth of well-separated hierarchical porous microstructures of wires or sheets on current collector could ensure robust physical contact and good electrical contact in such binder-free electrodes. The as-formed stable 3D framework exhibits loose texture and abundant open space to guarantee fast lithium ion flux across the interface. In other words, these hierarchical structures promise efficient ion transport into the active substances even at large current. On the other hand, open and porous frames could enhance the structural stability and better address the volume variation during repeated discharge/charge process. Meanwhile, the microstructure could reduce the surface energy and prevent the nanosized subunits from agglomeration. Moreover, the numerous nanosized crystallites provide reduced Li^+ ion diffusion length, and thus greatly enhance the electrochemical kinetics.

Inspired by these architecture merits, we then study the energy storage performance of hierarchical $Co_xMn_{3-x}O_4$ structures for their potential application as binder-free integrated electrodes in LIBs. The representative galvanostatic lithium insertion/extraction profiles at the cut-off voltage window of 0.05-3.0 V for the hierarchical $CoMn_2O_4$ nanowires at a current of 100 mA g^{-1} are illustrated **Figure 6.12**a. It is interesting that the as-synthesized hierarchical nanowires of $CoMn_2O_4$ exhibit extremely high original discharge and charge capacities of 1560 mAh g^{-1} and 900 mAh g^{-1}, respectively. Both of them are superior to the theoretical value (691 mAh g^{-1}) and there may be two plausible explanations for this discrepancy. Firstly, the excess capacities could be related with reversible generation/degradation of solid electrolyte interphase (SEI) layer from the decomposition of electrolyte, which frequently encounters in many binary metal oxides or ternary metal oxides based anode.[61, 71, 110, 118] Moreover, further oxidation of MnO to Mn_3O_4 or even Mn_2O_3 may also contribute to the total capacity, as reported by Kim on $ZnMn_2O_4$ nanowires.[33] The pronounced capacity reduction at the initial cycle can be caused by incomplete dissolution of the pre-formed SEI film. In order to further study the energy storage principle in hierarchical $CoMn_2O_4$ nanowires, differential capacity *vs.* voltage curves obtained at first few cycles (Figure 6.12b) are investigated with caution. During the discharge process at the first cycle, three distinguished peaks at 0.5 V, 0.9 V and 2.0 V are found, related with the formation of metallic Mn and Co nanocrystals from MnO and CoO, plus irreversible SEI film formation, respectively.[63, 78] The slight shift of these two cathodic peaks to higher potentials from the 2nd cycles onwards may correspond to the activation effect induced by the insertion of lithium ions during the 1st cycle, as observed in previous reports.[8, 11, 63, 112] Besides, an additional reduction peak centered at about 1.2 V appears ever since the second cycle, which may be attributed to reduction of Mn^{3+} to Mn^{2+}.[119] This extra electrochemical activity is possibly due to the enhanced kinetics of the nanowire electrode, leading to additive contributions to the total reversible capacity. There are two oxidation peaks with good reproducibility in the subsequent Li^+ ions extraction process: the one at about 1.4 V relates with the oxidation of Mn nanocrystals to MnO and the other one at 2.00 V is caused by the formation of CoO from metallic Co. The incorporation of Mn element would reduce the average voltage of the $Co_xMn_{3-x}O_4$ electrodes due to its lower lithium extraction voltage plateau, thus increasing the output of a LIB cell. Owing to the unique structure, the hierarchical nanowires manifest excellent capacity retention at continuously varying current densities. Galvanostatic charging-discharging measurements (Figure 6.12c) demonstrate that the $CoMn_2O_4$ nanowires on stainless steel can be reversibly cycled at 1-10 C (1C = 700 mA g^{-1}), with remarkable retained capacities of 530-215 mAh g^{-1}. To evaluate the cycling performance, the $CoMn_2O_4$ nanowires based electrode is charged and discharged at a current density of 800 mA g^{-1} over the voltage range 0.05-3.0 V, as depicted in Figure 6.12d. Despite the relatively huge capacity reduction in the second cycle, the electrode shows good capacity retention from the 2nd cycle onwards and eventually delivers an invertible capacity of 450 mAh g^{-1} over 30 cycles, which is 75.4% of the second cycle discharge capacity. The areal capacity of the hierarchical nanowires is also displayed by the vertical axis on the right in Figure 6.12d, where it decreases to about 171 μA h cm^{-1} over 30 cycles step by step. Taking account of no ancillary agents are employed in the electrode, the reversible rate capability and cycling stability shown above for the hierarchical nanowires arrays are quite attractive compared to previously reported $CoMn_2O_4$ electrodes.[35, 63, 109, 114, 119, 120]

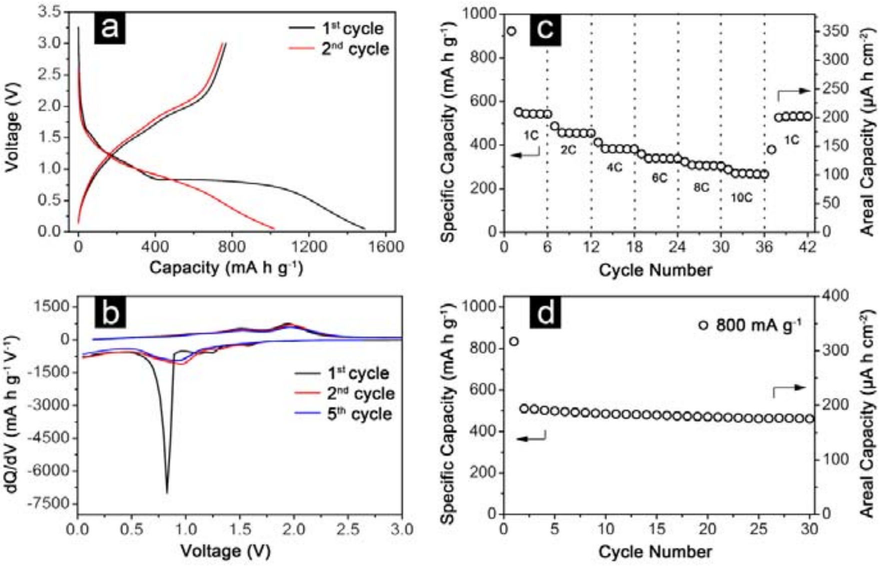

Figure 6.13 Electrochemical properties of hierarchical $MnCo_2O_4$ nanosheets array grown on stainless steel foil: (a) galvanostatic discharge/charge curves for the first and second cycles; (b) differential capacity *vs.* voltage profiles for the 1st, 2nd and 5th cycles; (c) discharge capacity at various current densities; (d) cycling test at a constant current of 800 mA g^{-1}. All tests were conducted in the voltage range of 0.05-3.0 V.

With hierarchical $MnCo_2O_4$ nanosheets, the structural advantages are proved once again in terms of remarkable electrochemical performance. As shown in **Figure 6.13**a and b, the discharge process of these $MnCo_2O_4$ nanosheets is quite different with that in the $CoMn_2O_4$ nanowires electrode (Figure 6.12a and b). Specifically, there is only one major cathodic peak found at around 0.8 V in the first cycle and 0.9-1.0 V in the next cycles. Also there is no distinct peak related to the Mn^{2+}/Mn^{3+} redox couple observed in the differential curves (Figure 6.13b). The exact reason for the differences observed in the electrochemical behaviour of the two electrodes appears unclear at this point. From the rate capability test shown in Figure 6.13c, the average specific capacities of hierarchical $MnCo_2O_4$ nanosheets are 540, 455, 380, 340 and 305 mAh g^{-1} at the current densities of 1C, 2C, 4C, 6C, and 8C, respectively (1C = 700 mA g^{-1}). Even at a relatively high rate of 10 C, the specific charge capacity can be maintained as 270 mAh g^{-1}. Moreover, the capacity could return to nearly the initial value of 530 mAh g^{-1} as the current is back to 1 C, indicating the well invertibility of the electrodes. In addition, the hierarchical $MnCo_2O_4$ nanosheets possess excellent cycling performance even at a higher current density of 800 mA g^{-1}, with capacity retention of 460 mAh g^{-1} over 30 cycles (Figure 6.13d).

To further understand the enhanced lithium storage performance of $Co_xMn_{3-x}O_4$ samples, electrochemical impedance measurements are carried out before and after charge-discharge experiments (**Figure 6.14**). It is obvious that the samples have lower charge-transfer impedance after discharging and recharging for 10 cycles at 800 mA g^{-1} than that of the fresh cells, which might be ascribed to the activation and re-construction of the $Co_xMn_{3\text{-}x}O_4$ structures in the first few cycles. It is also noteworthy that the charge-transfer impedance of $MnCo_2O_4$ nanosheets is always lower than that of $CoMn_2O_4$ nanowires, which might result in the improved electrode reaction kinetics and cycling stability. More importantly, after charging-discharging for 10 cycles at 800 mA g^{-1} (**Figure 6.15**), the morphologies and structures of the $Co_xMn_{3-x}O_4$ samples can be generally retained with slight aggregation observed. This observation is a good demonstration of the bulk structural stability of $Co_xMn_{3-x}O_4$ micro-/nanostructures, and thus leading to enhanced cycling stability.

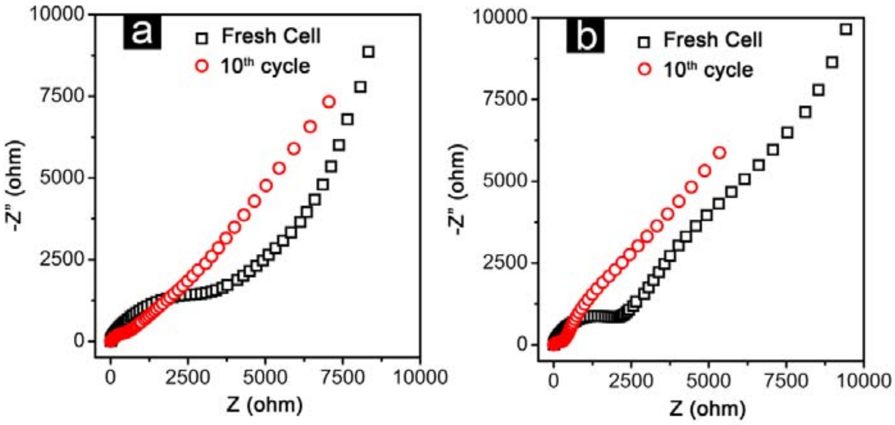

Figure 6.14 Nyquist plots of (a) hierarchical $CoMn_2O_4$ nanowires and (b) $MnCo_2O_4$ nanosheets grown on stainless steel foil before discharge process (in black squares) and after 10th cycles (in red circles).

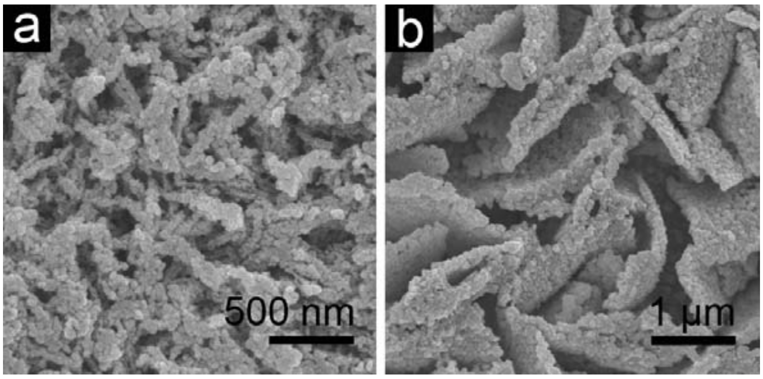

Figure 6.15 FESEM images of $Co_xMn_{3-x}O_4$ nanostructures after 10 discharge-charge cycles at 800 mA g^{-1}. (a) $CoMn_2O_4$ nanowires and (b) $MnCo_2O_4$ nanosheets grown on stainless steel foil.

Evidently, owing to their unique structural features, the hierarchical $Co_xMn_{3-x}O_4$ micro-/nanostructures grown on conductive substrates have been shown to exhibit interesting properties as potential integrated electrodes for LIBs. In the end, we should mention that to specific capacity can't be calculated accurately because the difficulty to weigh the little active substance on the relatively heavy matrix.

6.4 Summary

In this Chapter, we develop a straightforward method for the preparation of morphology-controlled hierarchical $Co_xMn_{3-x}O_4$ micro-/nanostructures with controllable compositions directly on current collector. The as-formed stable 3D framework is composed of direct growth of well-separated wires or sheets hierarchical porous microstructures, exploiting both the superiorities of nanosized subunits and micro-/submicrosized assemblies. In favor of the synergy and their intrinsic structural features, the hierarchical $Co_xMn_{3-x}O_4$ structures exhibit predominant electrochemical performances demonstrated by comparable specific capacities (540-207 mAh g^{-1}) at different current densities (1-10 C). These integrated functional materials might be promising for the construction of advanced electrodes for binder free energy storage devices with high performance.

Chapter 7. Morphology-controlled synthesis of hierarchical mesoporous $NiCo_2O_4$ micro-/nanostructures for advanced electrochemical capacitors[†]

7.1. Introduction

In recent years, tremendous research interest has been aroused worldwide on the development of advanced energy conversion and storage devices to meet the surging energy demand in consumer mobile electronics and electric vehicles.[8, 17, 19, 121-124] As we mentioned before, HSCs have been regarded as one of the most promising candidates for high-efficiency EES devices.[7, 122, 125] To improve the performance of HSCs, the key challenge is to improve the electrochemical activity and kinetic feature of the electrode itself.[122, 126] Compared to the bulk materials, the employment of micro-/nanostructures, especially three dimensional (3D) hierarchical porous architectures assembled from low dimensional nanosized building blocks, provides a promising and efficient avenue to boost the electrochemical performance of electrode materials. The micro-/nanostructures inherit the appealing advantages from both the pristine building blocks and superior secondary sub-units, and thus ensure enough pore space to keep electrolytes, short transport pathways for reaction ions, sufficient electrochemical active sites to modify the reaction activity and potential capability of

---

[†] Reproduced and modified from [L. Yu, H. Wu, T. Wu, C. Z. Yuan, *RSC Adv.*, 3, 23709-23714 (2013)] by permission from *The Royal Society of Chemistry*. Copyright 2013.

addressing the volumetric variation accompanied by the repeated electrochemical reactions.[1, 9, 10, 20, 21] Nevertheless, the practical performance is still far from expectation due to the intrinsic poor electrical conductivity of the TMOs themselves. Therefore, tremendous efforts are still desired to develop alternative cheap electrode materials, rather than the high-cost RuO_2-based materials,[53, 100, 102, 126] with intriguing electrical conductivity and 3D hierarchical porous micro-/nanostructures for the next-generation HSCs.

In Chapter 2, we have mentioned about the superiorities of $NiCo_2O_4$ materials for EES applications.[102] The previously reported hierarchical porous $NiCo_2O_4$ architectures with nanometer-sized primary building blocks as electrode materials are quite inspiring.[98, 99, 127-129] These instructive studies show that the fine control of size and morphology is currently a key but efficient aspect to further optimize the electrochemical performance of the $NiCo_2O_4$ electrodes. Despite these advances mentioned above, the synthesis of hierarchical porous $NiCo_2O_4$ micro-/nanostructures is still limited so far, and even some of the reported require the assistance of special instruments.[128] Therefore, it is very important to seek large-scale synthetic strategy to fabricate hierarchical porous $NiCo_2O_4$ micro-/nanostructures with controllable morphologies at a relative cost.

Inspired by the above considerations, we highlight herein a facile yet efficient two-step method for the controllable synthesis of hierarchical porous $NiCo_2O_4$ micro-/nanostructures constructed with mesoporous NW or NS building blocks. In particular, the morphology evolution is achieved through simple regulation of the reaction solvents. Remarkably, the intriguing hierarchical mesoporous micro-/nanostructure feature endows the as-synthesized $NiCo_2O_4$ electrodes with superior HSCs and desirable cycling stability as electroactive materials for advanced EESs.

7.2. Materials Synthesis

In a typical synthetic procedure for hierarchical $NiCo_2O_4$ superstructures composed of NW building blocks, 1 mmol of $Ni(NO_3)_2 \cdot 6H_2O$ and 2 mmol of $Co(NO_3)_2 \cdot 6H_2O$ were added into a mixed solution of 30 mL ethanol and 30 mL DI water generate a transparent pink solution (total volume: 80 mL) at ambient temperature. After that, 16 mmol of urea was dissolved as of additives for hydrolysis of metal salts. The Ni-Co precursor arrays were further put into a Teflon-lined stainless steel autoclave (90 mL in volume) and heated to at 105 °C and maintained for 12 h. Then, the resulting pink products were harvested via centrifugation and rinse with ethanol for several times. And the hierarchical $NiCo_2O_4$ superstructures composed of NSs were synthesized by a similar procedure just with the pure ethanol as the reaction solvent. The usage of ethanol was further tuned from 0 to 80 mL while keeping the same volume ratio of each component. After annealing the above precursors in air at 350 ^{o}C with a slow heating rate of 1 ^{o}C min^{-1} for 2 h, hierarchical $NiCo_2O_4$ micro-/nanostructures with NW or NS building blocks were finally obtained.

7.3. Results and Discussion

7.3.1. Formation of Hierarchical $NiCo_2O_4$ Micro-/Nanostructures

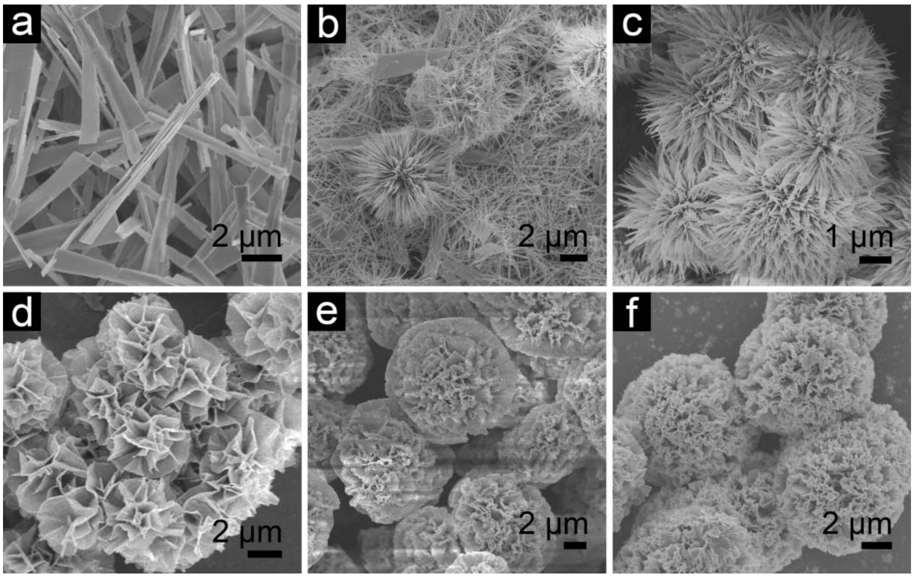

Figure 7.1 FESEM images of Ni-Co precursors with different solvents: (a) NC-EH-80, V($EtOH/H_2O$) = 40/40mL; (b) NC-EH-70, V($EtOH/H_2O$) = 35/35mL; (c) NC-EH-60, V($EtOH/H_2O$) = 30/30mL; (d) NC-E-60, V(EtOH) = 60mL; (e) NC-E-20, V(EtOH) = 20mL and (f) NC-E-10, V(EtOH) = 10mL.

Hierarchical mesoporous $NiCo_2O_4$ micro-/nanostructures were fabricated through a straightforward solvothermal process together with a post calcination treatment. It is well accepted that polarity of reaction system and solubility of reactants can largely affect the supersaturation for nucleation and crystal growth of product. Therefore, the morphology of Ni-Co precursor nanostructures can be readily controlled by tailoring the volumetric ratio of ethanol/water in the mixed solution.[130, 131] The typical FESEM images for the as-obtained Ni-Co precursors of the $NiCo_2O_4$ micro-/nanostructures are shown in **Figure 7.1**. As evident in Figure 7.1a-c, the Ni-Co precursors composed of one-dimensional (1D) belt-like or wire-like subunits are formed over a large area when the mixed water/ethanol reaction solvents were applied. Interestingly, the removal of DI water during the synthetic procedure, as seen in Figure 7.1d-f, results in the formation of hierarchical microspheres consisted of two-dimensional (2D) NSs. Of particular note, we also find that the volume of the reaction solvent can further significantly influence the final morphologies of the products, especially the assembly state of the building blocks. As shown in Figure 7.1a, individual nanobelts (NBs) as well as some assembling bundles of NBs, which is denoted as NC-EH-80, could be clearly observed when the volume of the mixed water/ethanol solvent is 80 mL. A reduction of the solvent volume leads to the appearance of the unique NWs with large aspect ratio. Moreover, even some NWs can be organized into a more complex hierarchical urchin-like sphere (Figure 7.1b). When the usage of the mixed solvent is further reduced to 60 mL, highly uniform spherical architectures assembled by ultra-long NWs are obtained with no any dispersed fragment (Figure 7.1c). In addition, the packing density reaches a maximum value in this condition; therefore, there are no more distinct morphological changes with further decrease of the solvent volume. Meanwhile, as for the pure ethanol system, the shape evolution of the Ni-Co precursor is not sensitive after the solvent volume is more than 60 mL, keeping the similar hierarchical flower-like structures to that of the NC-E-60 sample, which is composed of NS sub-units with rippled silk morphology (Figure 7.1d). However, the subsequent volume shrinkage gives rise to dense packing density of the NS subunits when the solvent volume is applied less than 60 mL. When the volume of ethanol is down to 20 mL, the formed NSs become even smaller in size and more compact with each other (Figure 7.1e), resulting in a larger hierarchical structure in contrast with the NC-E-60 with a hexagonal outline. Further lowering the dosage of the ethanol to 10 mL, 3D hierarchical flower-like microspheres with crowded NSs are observed on the resultant surface (Figure 7.1f).

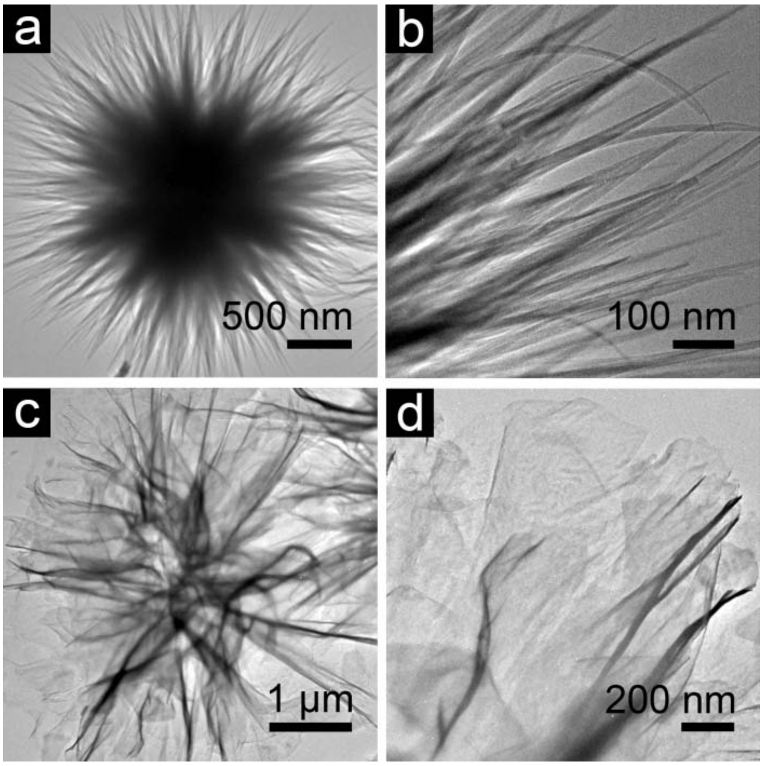

Figure 7.2 TEM characterizations of the representative Ni-Co precursors composed by different building blocks: (a, b) NWs (NC-EH-60) and (c, d) NSs (NC-E-60).

TEM analysis is further carried out to provide more insight into the detailed microstructures of the as-prepared samples. For the convenience of discussion, herein we mainly focus upon NC-EH-60 and NC-E-60 samples as the representative products for the hierarchical Ni-CO precursors composed of NWs or NSs. The low-magnification TEM image shown in **Figure 7.2**a presents a panoramic view of an individual hierarchical spherical structure of NC-EH-60 with a diameter of ~4 μm, which is assembled by high-density NW sub-units with uniform diameter and length. And these oriented NW sub-units are separated well in a radial form, creating abundant "V-type" porous pathways for the quick transport of the electrolyte ions into the open architecture. An enlarged view (Figure 7.2b) clearly demonstrates the solid and dense nature of the NWs possessing a needle-like geometric form with a cutting-edge around several nanometers. Whereas, a typical sphere of NC-E-60 sample with a diameter of ~3 μm is loosely packed by ultrathin NSs with the folding silk-like shapes of bending, curling, and crumpling, because of much bigger lateral size than the thickness, as observed in Figure 7.2c. The dark strips distributed across the whole sphere generally show the folded edges or wrinkles of the NSs. A closer TEM observation around the edge of the hierarchical spheres (Figure 7.2d) further indicates the ultrathin nature of a single flat-lying NS with almost transparent feature.

Besides the solvent compositions, the co-existence of both Co^{2+} and Ni^{2+} in the reaction solution also has a significant role in the generation of the resulting hierarchical $NiCo_2O_4$ micro-/nanostructures (**Figure 7.3**). Specifically, in the absence of the Ni^{2+}, the resulting Co-based products are simple mixtures of 1D NBs and hierarchical spheres in the mixed solvent (Figure 7.3a), or some non-uniform microstructures with NSs-assembled nanohorns (Figure 7.3b) on the exterior surface in pure ethanol system. In a sharp contrast, there are only some irregular hierarchical structures with tiny NSs on the surfaces of the Ni-based products in either mixed (Figure 7.3c) or pure solvent system (Figure 7.3d) when the Co^{2+} was absent in the reaction solution.

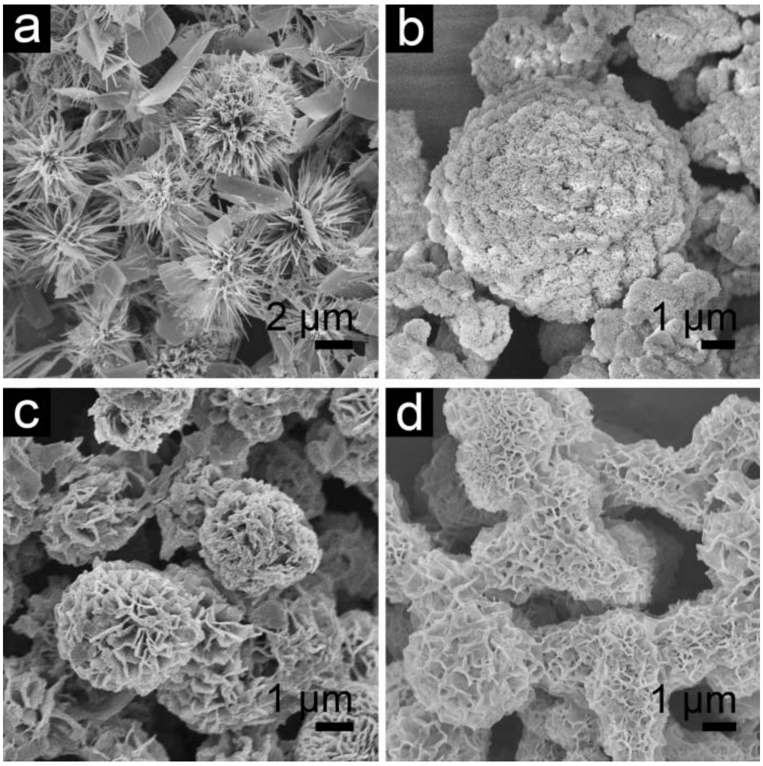

Figure 7.3 FESEM images of the Co-based precursor obtained using (a) the mixed solvent of EtOH/H_2O (30mL/30mL), and (b) EtOH as the solvent Ni-based precursor structures obtained using (c) the mixed solvent of EtOH/H_2O (30mL/30mL), and (d) EtOH as the solvent.

After a careful annealing treatment in air, crystallized $NiCo_2O_4$ can be easily derived from these Ni-Co precursors without noticeable alteration in the overall morphology. The corresponding crystallographic structures of the as-synthesized $NiCo_2O_4$ are confirmed by XRD analysis in **Figure 7.4**. All the well-defined diffraction peaks of hierarchical urchin-like (denoted as NCO-NWs) and flower-like (designed as NCO-NSs) micro-/nanostructures derived from the NC-EH-60 and NC-E-60 precursors, respectively, correspond to the cubic $NiCo_2O_4$ phase (JCPDS Card No. 20-0781, space group: *F*3* (202)). And no any noticeable peaks from impurities or contaminants are observed.

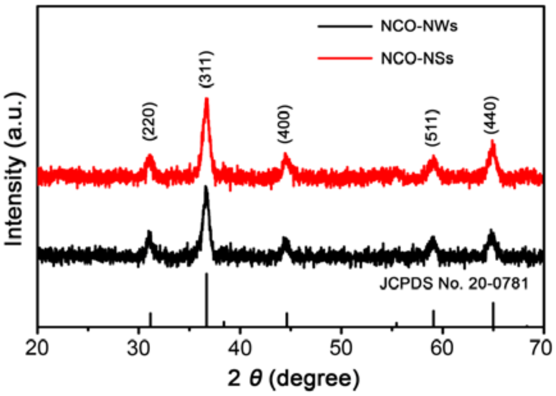

Figure 7.4 XRD patterns of the NCO-NWs and the NCO-NSs as indicated.

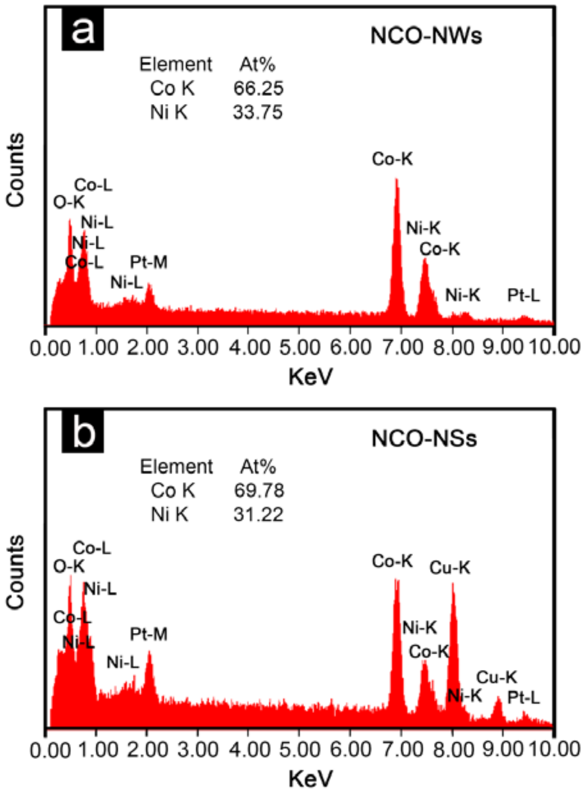

Figure 7.5 EDX spectra of (a) the NCO-NWs and (b) the NCO-NSs.

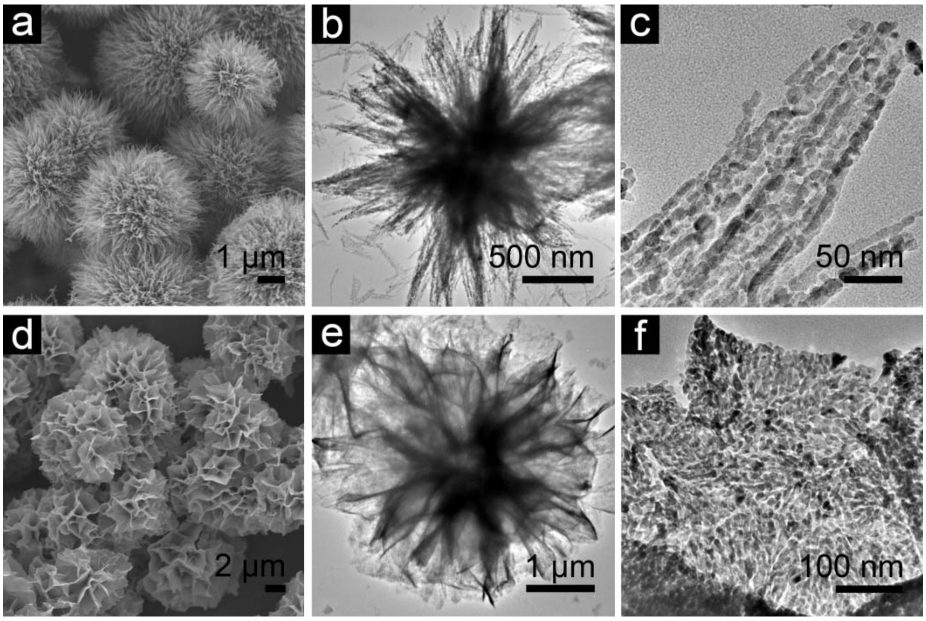

Figure 7.6 FESEM and TEM characterizations of crystallized $NiCo_2O_4$ hierarchical structures: (a-c) NCO-NWs and (d-f) NCO-NSs.

The EDX data (**Figure 7.5**a) reveals that the Ni/Co atomic ratio of the NCO-NWs is 1:1.96, fitting well with the theoretical value. Meanwhile, the elemental composition of the NCO-NSs characterized by EDX reveals a Ni/Co atomic ratio of 1:2.23 (Figure 7.5b). The trace difference of the atomic ratio between the two samples might be attributed to the different precipitate rate of Ni^{2+} and Co^{2+} ions in diverse solvents. The detailed geometrical characteristics of the hierarchical NCO-NWs and NCO-NSs micro-/nanostructures are further elucidated by FESEM and TEM observations (**Figure 7.6**), confirming that the hierarchical $NiCo_2O_4$ micro-/nanostructures inherit well the original 3D features from their precursors without significant aggregation or collapse. In good agreement with the above FESEM image (Figure 7.6a), it can be seen in the low-magnification TEM image (Figure 7.6b) that the NCO-NWs possess the hierarchical urchin-like spherical superstructure, similar to the NC-EH-60 precursor, but slightly smaller in size. Of note, a magnified view of the NCO-NWs (Figure 7.6c) clearly indicates the NW building block is composed of numerous primary nanoparticles (NPs) with a size of tens of nanometers, resulting in some tiny mesopores between these NPs.

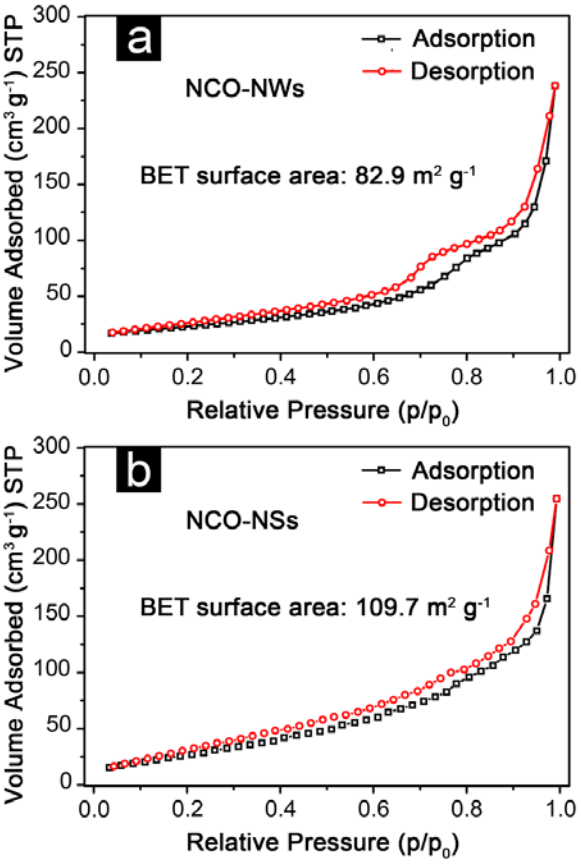

Figure 7.7 N_2 adsorption-desorption isotherms at 77 K of (a) the NCO-NWs and (b) the NCO-NSs.

The unique mesoporous characteristic grants the NCO-NWs a relatively large specific surface area (SSA) of 82.9 m^2 g^{-1}, determined by N_2 sorption measurement (**Figure 7.7**a). Meanwhile, the representative FESEM and TEM images of well-dispersed NCO-NSs microspheres (Figure 7.6d, e) further demonstrates that the flower-like morphology of NC-E-60 is perfectly retained after the thermal conversion into the NCO-NSs with a negligible change in size. More significantly, numerous of mesopores can be clearly identified on the surface of the NSs from the high-magnification TEM image (Figure 7.6f), which may be created by gas release during the thermal transformation. Owing to the 2D ultra-thin and porous structural feature, the NCO-NSs sample exhibits a much higher SSA of ~109.7 m^2 g^{-1}.

7.3.2. Electrochemical Measurements

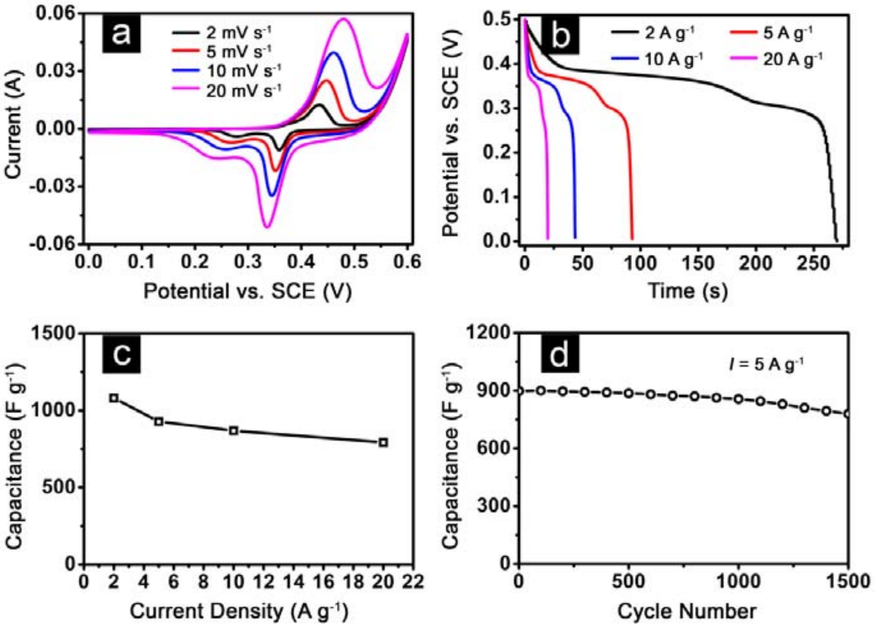

Figure 7.8 Electrochemical properties of the NCO-NWs: (a) CV curves at different scan speeds from 2 to 20 mV s^{-1}. (b) Discharge voltage curves at variable current densities from 2 to 20 A g^{-1}. (c) Specific capacitance as a function of current density; (d) Cycling test at a fixed current density of 5 A g^{-1}.

The two unique hierarchical micro-/nanostructures with mesoporous and nanoscale NW or NS building blocks endow sufficient electroactive sites, convenient diffusion channels favorable for electrolyte transport and fast penetration of ion/electron, leading to potentially enhanced electrochemical reactivity for high-performance HSCs.[7, 21, 122] Motivated by these attracting merits, next, we systematically investigate the electrochemical performance of these two diverse hierarchical mesoporous $NiCo_2O_4$ micro-/nanostructures as electrode materials for advanced HSCs. The electrochemical tests were carried out in 2 M KOH solution. **Figure 7.8**a shows the representative cyclic voltammograms (CVs) of the NCO-NWs at variable scan speeds from 2 to 20 mV s^{-1}. Usually, the EDLCs exhibit CV profiles with a nearly rectangular shape,[132] whereas the CV curves of NCO-NWs with an apparent set of redox peaks over various scan rates obviously reveal its battery-like characteristics. Galvanostatic charge-discharge measurement are carried out in the voltage window of 0-0.5 V (*vs.* SCE) to further evaluate the performance of the NCO-NWs electrode. The corresponding discharge voltage *vs.* time plots at various current densities are presented in Figure 7.8b. Obviously, there are voltage plateaus in all these discharge plots at ~0.4 V (*vs.* SCE), consistent with the CV curves, further supporting its typical Faradaic redox reactions. The calculated specific capacitances as a function of the discharge current density from chronopotentiometry curves are collected and plotted in Figure 7.8c. Impressively, the porous NCO-NWs sample delivers high specific capacitance values of 1080.2, 912.9, 868, and 792 F g^{-1} at the discharge current densities of 2, 5, 10, and 20 A g^{-1}, respectively, suggesting that ~73% of the capacitance is maintained with the increase of the current density from 2 to 20 A g^{-1}. Such good electrochemical activity of the NCO-NWs electrode should benefit from its unique urchin-like porous micro-/nanostructures. The abundant open and porous diffusion channels existing in the unique urchin-like architecture can act as an “ion reservoir”, which ensures a steady supply of OH^- ions, and the fast and effective access of electrolyte to each NW at high rates, and the rapid Faradic reaction for efficient energy storage. The electrochemical stability (Figure 7.8d) is further studied through the repeated electrochemical reactions at a fixed current of 5 A g^{-1}. The specific capacitance is around 903 F g^{-1} in the 1st cycle and it gradually decreases to 780.8 F g^{-1} after cycling over 1500 times. The total capacitance loss is ~13.5%.

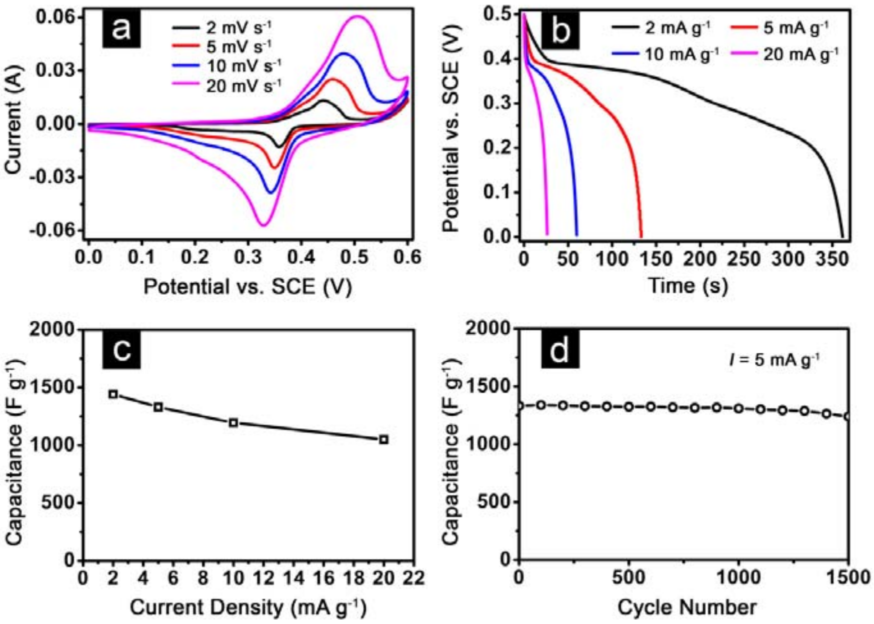

Figure 7.9 Electrochemical properties of the NCO-NSs: (a) CV curves at different scan speeds from 2 to 20 mV s^{-1}; (b) Discharge voltage curves at variable current densities from 2 to 20 A g^{-1}; (c) Specific capacitance as a function of current density; (d) Cycling test at a fixed current density of 5 A g^{-1}.

To further demonstrate the structural advantages, the electrochemical activities of the NCO-NSs is studied under the same conditions. As shown **Figure 7.9**a, the representative CV curves for the NCO-NSs electrode are similar with those of the NCO-NWs, demonstrating its battery-like property that comes from the reversible Faradaic reactions related to M-O/M-O-OH (M means Ni and Co ions) during the charge-discharge processes.[103] Figure 7.9b shows the discharge curves at various current densities. Notably, the flower-like NCO-NSs sample demonstrates enhanced capacitances of 1440.2, 1333, 1193.8, and 1048.7 F g^{-1} at the discharge current densities of 2, 5, 10, and 20 A g^{-1}, respectively, as shown in Figure 7.9c. More remarkably, the specific capacitance of the NCO-NSs decreases from 1333 to 1240.3 F g^{-1} after 1500 repeated cycles at a fixed current of 5 A g^{-1} (Figure 7.9d), that is, the NCO-NWs sample displays an enhanced capacitance retention of ~94%. Of particular note, the electrochemical date mentioned above confirms that the unique NCO-NSs electrode shows even larger specific capacitances as well as better electrochemical stability at high current densities for long-term HSCs application when compared to the NCO-NWs sample. The striking enhancement in electrochemical capacitance of the unique NCO-NSs electrode could be ascribed to the ultra-thin and mesoporous feature of its NS building blocks, which hold great promise in offering more electroactive points to facilitate electrochemical reactions and more efficient transport of the electrolyte into the electroactive substances. Besides, the unique NS morphology is advantageous for better addressing the volumetric change due to the smaller crystal size within the NSs compared to the NWs.[7, 133]

7.4. Summary

In this Chapter, we successfully developed a straightforward strategy to synthesis hierarchical mesoporous $NiCo_2O_4$ micro-/nanostructures with NWs or NSs building blocks. The specific morphologies were easily tuned through simple regulation of the composition and volume of the reaction solvent. Benefiting from the appealing hierarchical mesoporous micro-/nanostructure features, the two $NiCo_2O_4$ electrodes exhibited appealing electrochemical performance as advanced electrodes for high-performance HSCs. In particular, the as-fabricated NSs-assembled flower-like hierarchical $NiCo_2O_4$ micro-spherical architecture delivered a higher specific capacitance of 1333 F g^{-1}, and much better cycling stability with a low capacitance loss of only 6% at a current density of 5 A g^{-1} after 1500 cycles. Considering the remarkable electrochemical activities and the facile synthesis at relatively low cost, these hierarchical $NiCo_2O_4$ micro-/nanostructures might offer significant promise for the large-scale fabrication of next-generation HSCs, and even for advanced Li-ion batteries.

Chapter 8. Formation of Yolk-shelled Ni-Co Mixed Oxide Nanoprisms with Enhanced Electrochemical Performance for Hybrid Supercapacitors and Lithium ion Batteries†

8.1. Introduction

With the surging demand for clean and renewable energy sources to address urgent issues about impendent shortage of fossilized energy and severe environmental contamination, electrical energy storage (EES) systems will play a more vital role in the future than at any time in the past.[1, 134] Among EES technologies, hybrid supercapacitors (HSCs) and lithium ion batteries (LIBs) have aroused widespread concern in virtue of their high power/energy density with long life span.[118, 135] However, conventional bulk electrode materials are approaching the theoretical limits and their performance is lagging far behind the requirements for large-scale energy applications.[1, 134, 136] In this regard, massive research efforts have been devoted for the design and fabrication of new attractive electrode materials that can store and deliver more energy efficiently to improve the electrochemical performance of EES devices.[3, 122, 136]

As mentioned in Chapter 2, Ni-Co based mixed oxides, especially the nickel cobaltites ($NiCo_2O_4$), have been intensely investigated as attractive alternatives for

---

† Reproduced and modified from [L. Yu, B. Y. Guan, W. Xiao, X. W. Lou, *Adv. Energy Mater.*, in pressed (2015)] by permission from *John Wiley and Sons*. Copyright 2015.

HSCs owing to their favorable characteristics.[102, 136-140] Superior to monometallic nickel oxide or cobalt oxide, Ni-Co mixed oxides can synergistically improve the electrochemical properties in terms of enhanced electrical/ionic conductivity, mechanical stability and richer redox reactions involving different ions, which are believed to be of huge benefit for electrode materials in both HSCs and LIBs.[102, 141, 142]

Besides the control in composition, the realization of high-efficiency energy storage also depends on the rational design of electrode structures.[8, 11, 122] One of the effective strategies is the employment of hollow architectures with complex interiors as advanced electrodes, such as core-shell, yolk-shell and multi-shell configurations, because these special structures could own the merits from both nanosized subunits and hollow structures.[24, 143-146] Particularly, nanoscale-sized subunits can shorten the diffusion pathway, making it possible to charge faster or to draw high current in a short time. Meanwhile, the hollow space between the shells can not only act as a barrier to prevent the encapsulated electroactive nanoparticles from aggregation, but also accommodate the large expansion that leads to failure and short cycle life of electrodes.[145, 147, 148] Furthermore, the core structure in the complex hollow particles will effectively boost the energy density of the electrodes by enlarging the weight fraction of electrochemically active component.[149] For example, Wang's group highlighted the fabrication of multi-shelled Co_3O_4 hollow spheres using carbon spheres as hard template. The as-prepared multi-shelled particles display superior lithium storage performance compared to single-shelled Co_3O_4 spheres.[145] Also, as demonstrated by Kang and co-workers, yolk-shelled SnO_2 spheres prepared by scalable spray pyrolysis exhibit better cycling performance than densely structured particles as electrode materials for LIBs.[149] Recently, our group developed an effective self-templated strategy to obtain $NiCo_2O_4$ complex hollow spheres from metal glycerate spheres with remarkable electrochemical performance as electrode materials for both HSCs and LIBs.[139] Notwithstanding the above advances, the research on specially structured Ni-Co oxide hollow particles is still quite limited so far because of various difficulties.[11, 41]

Inspired by above considerations, in this Chapter, we highlight a facile synthesis of mesoporous yolk-shelled Ni-Co oxide nanoprisms based on simple annealing of pre-formed metal acetate hydroxide precursors. Besides, the composition of the final yolk-shelled products can be easily controlled through the adjustment of molar ratio of Ni/Co in the precursor. Due to the unique architectures, the optimal Ni-Co oxide sample exhibits exceptional electrochemical performance as advanced electrodes with high capacitance/capacity and excellent cycling stability.

8.2 Materials Synthesis

8.2.1. Synthesis of Ni-Co Precursor Prisms

In a typical synthesis, polyvinylpyrrolidone (PVP, PVP10, MW ~ 10000, 3.0 g) and a mixture of metal acetate tetrahydrate (0.64 g) with different molar ratios of Ni/Co (1:2 to 2:1) were dissolved into 200 mL of ethanol (Aik Moh Paints & Chemicals) at room temperature to generate a transparent solution. The solution was then heated up to 85 ^{o}C under refluxing for 10 h. Then, the as-obtained precipitate was rinsed with ethanol once before being fully dried in the oven at 60 ^{o}C.

8.2.2. Synthesis of Yolk-shelled Ni-Co Mixed Oxide Nanoprisms

For the formation of mesoporous Ni-Co mixed oxide yolk-shell nanoprisms, the above Ni-Co precursors were calcined in air at 350 ^{o}C for 2 h with an andante ramping speed of 2 ^{o}C min^{-1}.

8.3. Results and Discussion

8.3.1. Formation of Yolk-shelled Ni-Co Mixed Oxide Nanoprisms

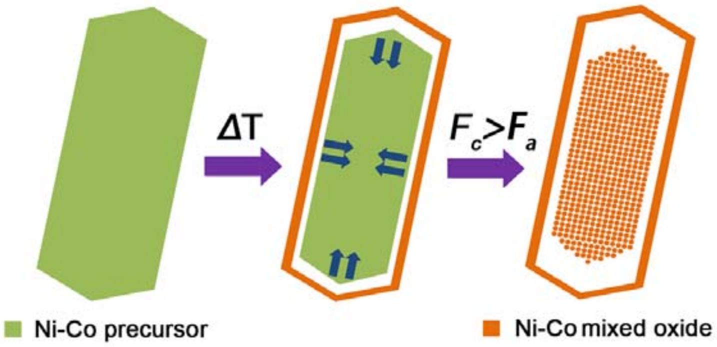

Figure 8.1 Schematic diagram of the formation of mesoporous yolk-shelled Ni-Co mixed oxide prisms. F_c: contraction force; F_a: adhesive force.

These novel mesoporous yolk-shelled Ni-Co oxide nanoprisms are formed through a contraction process driven by thermodynamics. As depicted in **Figure 8.1**, the formation procedure is composed of two steps. By utilizing a certain amount polyvinylpyrrolidone (PVP) as structure-stabilizing agent, monodisperse Ni-Co precursor particles with tetragonal prism-like structure are firstly prepared by a modified co-precipitation method.[150] Benefitting from the strong coordination competence of PVP to metal cations via the -N and/or C=O function groups, the usage of PVP is crucial for the successful formation of highly uniform and discrete precursor particles (**Figure 8.2**).[40] When the amount of PVP is not enough, similar prisms can be produced with a wide-size distribution.

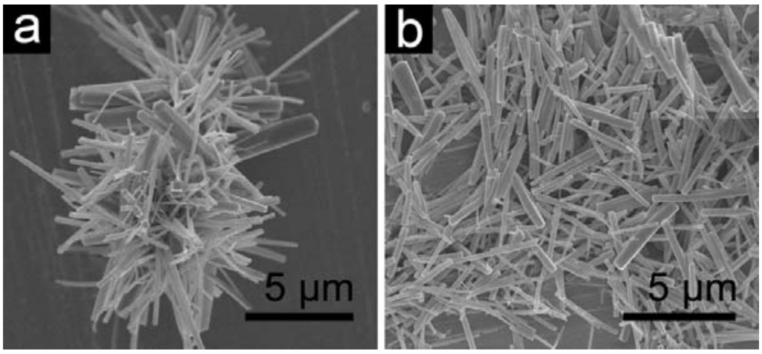

Figure 8.2 FESEM images of Ni-Co precursors (the molar ratio of Ni/Co is 0.5 in the initial reactants) with different amounts of PVP: (a) 0 g and (b) 1.0 g.

Then, a thermal process in air at 350 °C with a heating rate of 2 ºC min^{-1} is applied to transform the Ni-Co precursor into Ni-Co mixed oxide. The formation mechanism of mesoporous yolk-shelled structure can be interpreted as the heterogeneous contraction accompanied by non-equilibrium thermal annealing.[151] More specifically, the phase composition of Ni-Co precursor investigated by XRD (**Figure 8.3**) can be assigned to the tetragonal nickel-cobalt acetate hydroxide, which means the Ni-Co precursor contains a large fraction of organic species including acetate and attached PVP on the surface.[152] As further verified by TGA (**Figure 8.4**), there is a large mass loss (~55.3%) during thermal decomposition of Ni-Co precursor at high temperature, indicating a huge volume shrinkage during the annealing treatment.

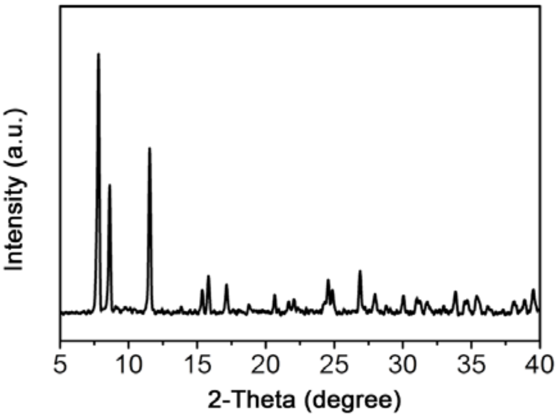

Figure 8.3 XRD pattern of Ni-Co precursor synthesized with the Ni/Co molar ratio of 0.5 in the initial reactants.

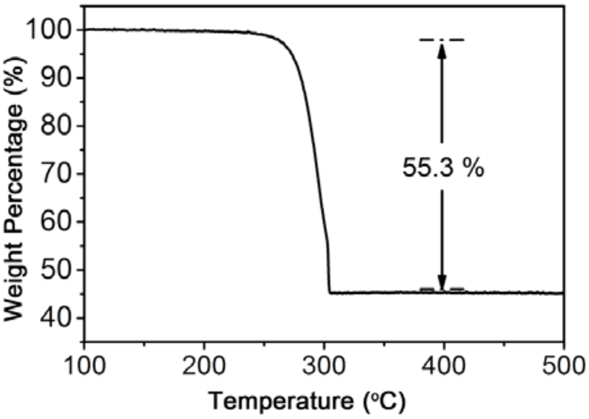

Figure 8.4 TGA curve of the Ni-Co precursor synthesized with the Ni/Co molar ratio of 0.5 in the initial reactants under air flow with a heating rate of 10 °C min^{-1}.

At the beginning of annealing process, a large temperature gradient (ΔT) leads to the generation of a dense Ni-Co oxide shell at the outermost shell of the Ni-Co precursor. Then, the interface between the Ni-Co oxide shell and the Ni-Co precursor core will simultaneously have two opposite actions (the so-called heterogeneous contraction). One is the contraction force (F_c) caused by the large weight loss during oxidative decomposition of the organic species, which promotes the inward shrinkage of the Ni-Co precursor core. Meanwhile, the other is the opposite adhesive force (F_a)

related with the formation of Ni-Co oxide and the CO_2 gas released during annealing treatment, which keep off the inward contraction. With a large ΔT, F_c surpasses F_a at the beginning. Therefore, the inner part shrinks inward and disaffiliates itself from the pre-formed outer shell. It is rational to deduce that ΔT attenuates from the outermost layer to the inner part. As a result, the ΔT at the new interface is too weak to induce the formation of another dense shell on the detached internal part. As a result, the inner part of the precursor decomposes into a solid structure to form yolk-shell architecture.

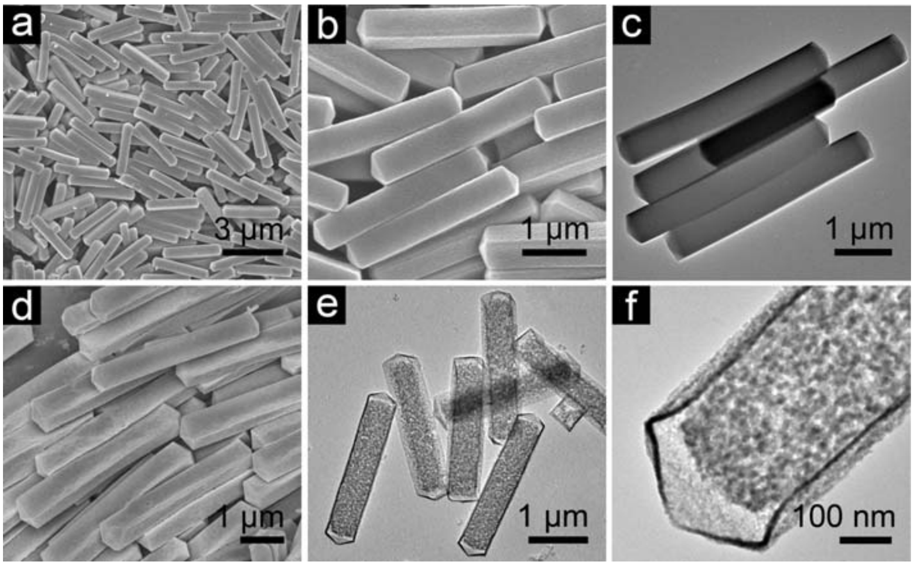

Figure 8.5 FESEM and TEM images of (a-c) Ni-Co precursor particles and (d-f) as-obtained mesoporous $Ni_{0.37}$Co-oxide prisms after an annealing treatment at 350 ^oC with a slow speed of 2 ^oC min^{-1} in air.

The morphology and microstructure of Ni-Co precursor and corresponding yolk-shelled Ni-Co oxide particles are first characterized by FESEM and TEM. As shown in **Figure 8.5**a, these Ni-Co precursor particles consist of well-defined nanoprisms with a narrow size distribution. Meanwhile, as revealed by the enlarged FESEM image (Figure 8.5b), the Ni-Co precursor particles possess a rather smooth surface with a high aspect ratio, suggesting their single-crystal-like character. In addition, each tetragonal nanoprism has an average length of ~2.8 μm with a pyramid-shaped apex at both ends. These precursor particles are solid as confirmed by TEM observation (Figure 8.5c) without discernible porosity. After the annealing treatment in air, the Ni-Co precursor particles are transformed into Ni-Co oxide with well-retained prism-like morphology (Figure 8.5d). The yolk-shelled architecture and detailed geometrical feature of as-obtained nano-prisms are directly studied by TEM observation. The panoramic TEM image (Figure 8.5e) shows that uniform yolk-shelled structures can be observed with the relatively light contrast of the inner yolk structure. Owing to the large aspect ratio of the Ni-Co precursor, the shrinkage degree varies for different directions. Specially, the contraction along the long axis of prism is much more pronounced than the short axis, creating a more prominent void at both ends. TEM image of one end (Figure 8.5f) at high magnification clearly reveals the yolk-shell feature with a distinct void space between the exterior layer and the inner part. The shell structure with an average thickness around 20-30 nm is of sufficient robustness to endure the thermal decomposition process. Furthermore, it can also be observed that the interior core is highly porous consisting of numerous polycrystalline primary particles with size of tens of nanometers. In addition, the PVP does not contribute to the formation of the yolk-shell structure and similar yolk-shelled Ni-Co oxide in a wide range of particle size distributions from annealing Ni-Co precursors without PVP can be observed (**Figure 8.6**).

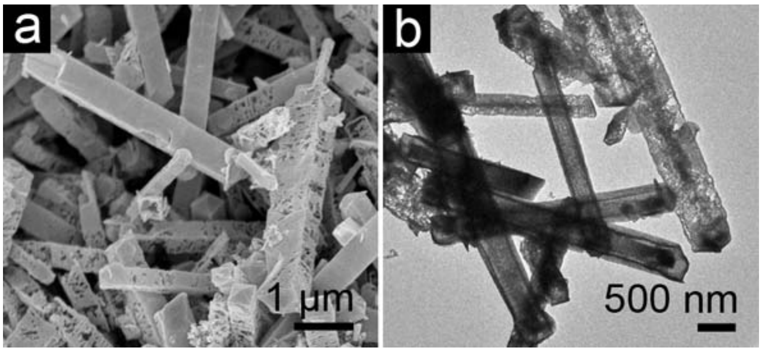

Figure 8.6 FESEM and TEM image of yolk-shelled Ni-Co oxide in a wide range of particle size distributions from annealing Ni-Co precursors (the molar ratio of Ni/Co is 0.5 in the initial reactants) without PVP.

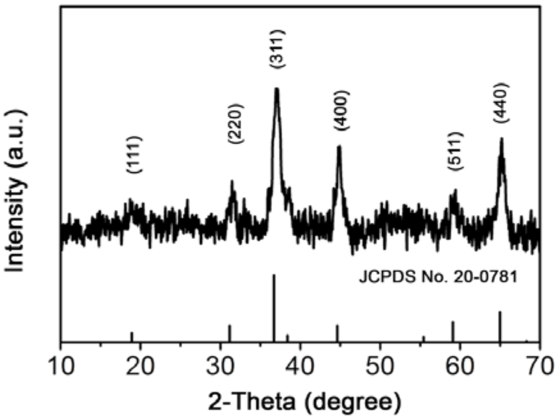

Figure 8.7 XRD pattern of crystallized yolk-shelled $Ni_{0.37}$Co-oxide nanoprisms after annealing treatment in air.

As confirmed by XRD (**Figure 8.7**), all the peaks in the diffraction pattern can be satisfactorily attributed to the cubic $NiCo_2O_4$ phase (JCPDS Card No. 20-0781) although the peak intensity is not very strong.[153] The average crystallite size calculated using the Scherrer equation is about 13.67 nm, revealing that yolk-shelled structures consist of nanocrystalline building blocks. EDX result (**Figure 8.8**) shows that the Ni/Co atomic ratio in the yolk-shelled structure is about 0.37 (thereafter the sample is designated as $Ni_{0.37}$Co-oxide), while the Ni/Co atomic ratio of the reactants is 0.5. The chemical composition of the sample is further measured using ICP optical emission spectroscopy. The Ni/Co atomic ratio for the $Ni_{0.37}Co$-oxide sample determined by the ICP analysis is about 0.38, close to EDX result. It might be hypothesized that it is more difficult for Ni^{2+} ions to precipitate in ethanol compared to Co^{2+} ions during the precursor synthesis.

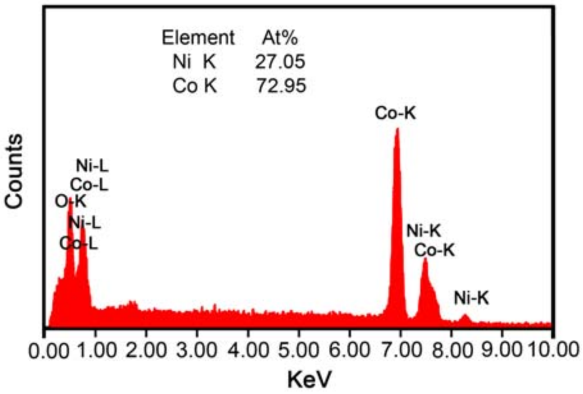

Figure 8.8 EDX spectrum of crystallized yolk-shelled $Ni_{0.37}Co$-oxide nanoprisms.

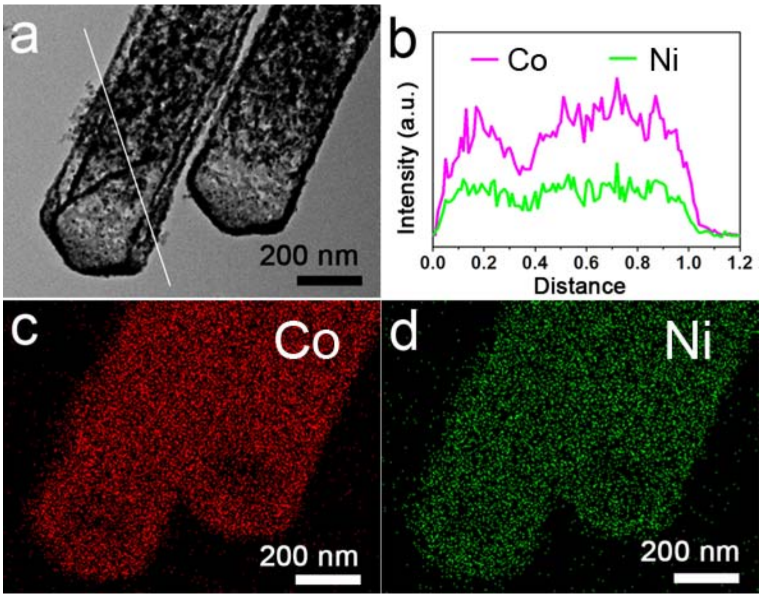

Figure 8.9 HAADF-STEM and elemental mapping of $Ni_{0.37}Co$-oxide nanoprisms.

High-angle annular dark-field STEM (HAADF-STEM) and elemental mapping results demonstrate the generally uniform distribution of Ni and Co throughout the core and shell structures (**Figure 8.9**). As determined by N_2 sorption measurement at

77 K (**Figure 8.10**), the open pores formed by the void between the shell and the core combined with the mesopores among the nanometer-sized primary particles endow the $Ni_{0.37}$Co-oxide nanoprisms with a high BET specific surface area of 56.1 m^2 g^{-1}. Such a yolk-shelled structure can be expected to provide enough active sites for electrochemical reactions and ensure the transport of the electrolyte into the electroactive substances.[148]

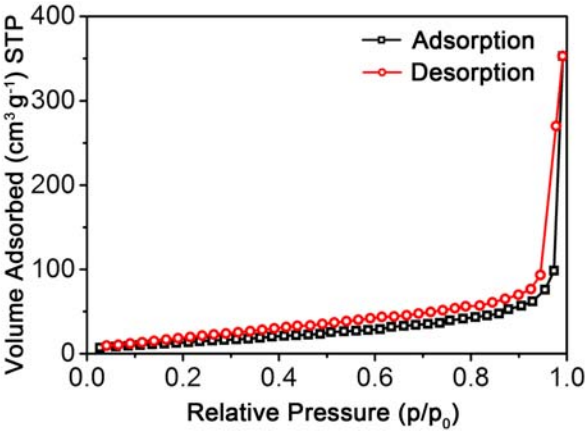

Figure 8.10 N_2 adsorption-desorption isotherms of $Ni_{0.37}$Co-oxide nanoprisms.

It is worth to mention that the composition of Ni-Co precursor particles can be easily tuned by varying the molar ratio of Ni/Co in the reactants. As a result, this synthesis strategy can afford yolk-shelled nanoprisms of Ni-Co mixed oxides with diverse composition. FESEM and corresponding TEM images (**Figure 8.11**) show that the Ni-Co precursors with diverse Ni/Co molar ratios manifest similar shape. Meanwhile, with the increase of Ni element in the final product, the aspect ratio of the prism is gradually reduced. After the same calcination treatment, the outer surface of the final product becomes quite rough especially for the Ni-rich oxide, as presented in **Figure 8.12**a, c.

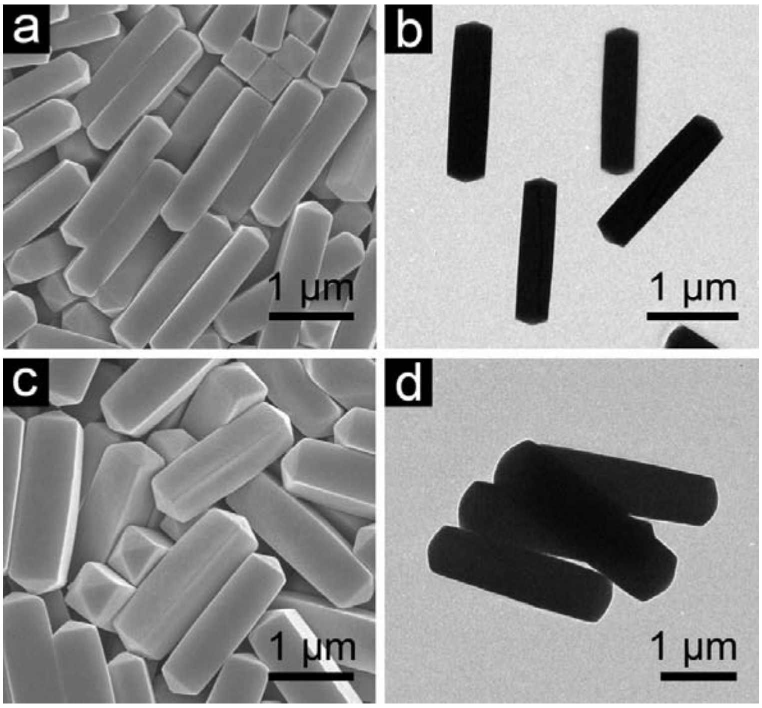

Figure 8.11 FESEM and TEM characterizations of Ni-Co precursors obtained with Ni/Co molar ratios of (a, b) 1/1 and (c, d) 2/1 in the initial reactants.

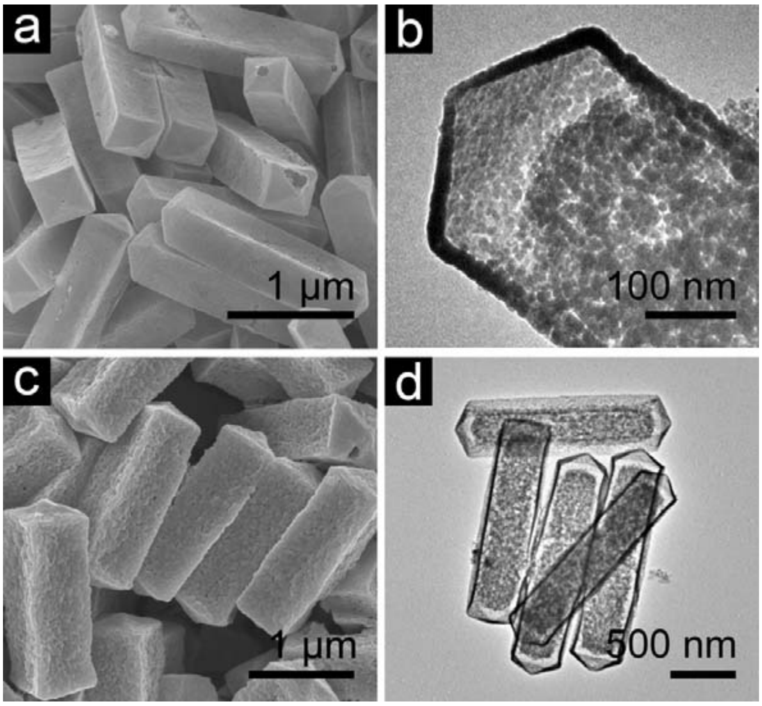

Figure 8.12 FESEM and TEM characterizations of Ni-Co oxides with Ni/Co molar ratios of (a, b) 0.82 and (c, d) 1.38.

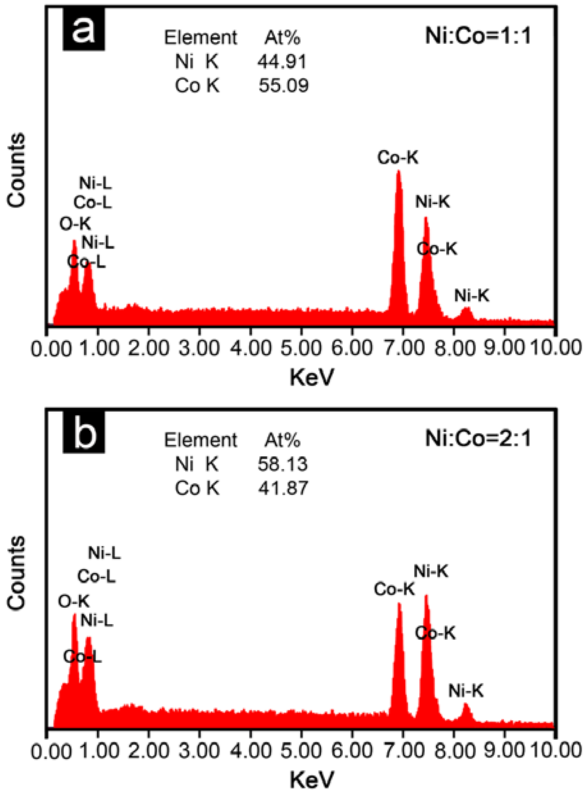

Figure 8.13 EDX spectra of crystallized Ni-Co oxides obtained with diverse molar ratios of Ni/Co in the initial reactants: (a) 1/1; (b) 2/1.

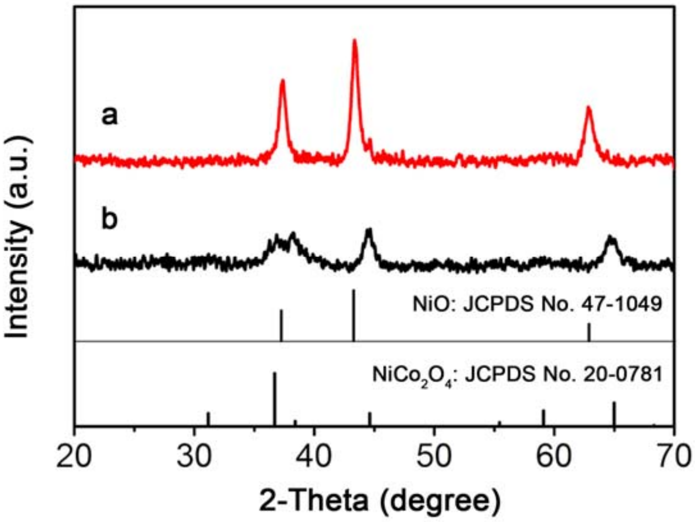

Figure 8.14 XRD patterns of (a) $Ni_{1.38}$Co-oxide and (b) $Ni_{0.82}$Co-oxide.

The EDX data (**Figure 8.13**) for these Ni-Co oxides reveal that the Ni/Co atomic ratios are 0.82 and 1.38 corresponding to the Ni/Co atomic ratios of 1.0 and 2.0 in the reactants respectively. Accordingly, these two samples are thereafter designated as $Ni_{0.82}$Co-oxide and $Ni_{1.38}$Co-oxide. Interestingly, there is some differences observed in the phase of these two samples. According to the XRD patterns (**Figure 8.14**), there is a phase separation within the Co-rich oxide, which might be explained by the different lattice parameters of NiO and Co_3O_4.[154] By contrast, the XRD pattern of Ni-rich oxide might be assigned to NiO. The absence of any diffraction peak from cobalt oxides might suggest the complete incorporation of Co into lattice of NiO. TEM images (Figure 8.12b, d) provide the direct evidence that yolk-shelled structures are formed for both samples with different compositions.

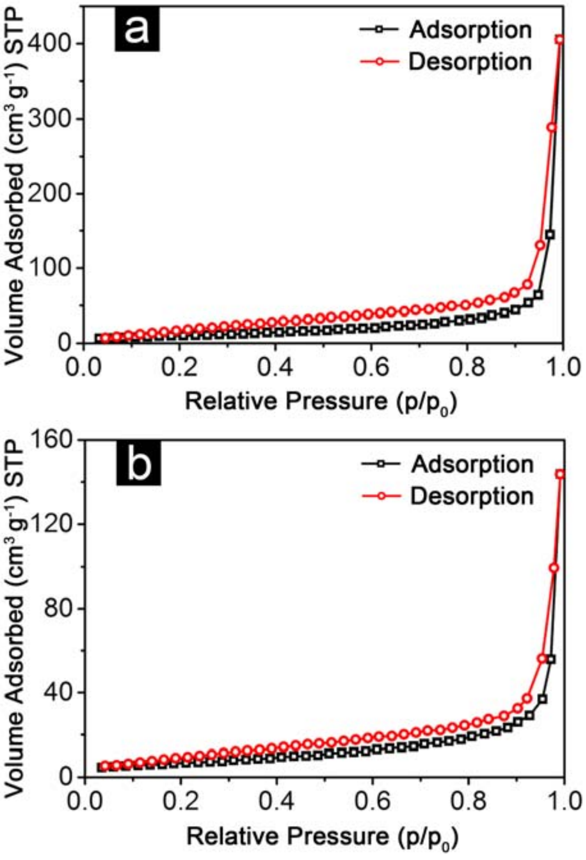

Figure 8.15 N_2 adsorption-desorption isotherms of (a) $Ni_{0.82}$Co-oxide and (b) $Ni_{1.38}$Co-oxide.

Similar to the previous $Ni_{0.37}Co$-oxide structures, the interparticle mesopores are uniformly distributed throughout the internal core for both samples. However, both samples possess relatively low BET specific surface area of 38.6 $m^2\ g^{-1}$ for $Ni_{0.82}Co$-oxide and 24.1 $m^2\ g^{-1}$ for $Ni_{1.38}Co$-oxide (**Figure 8.15**).

8.3.2. Electrochemical Measurements

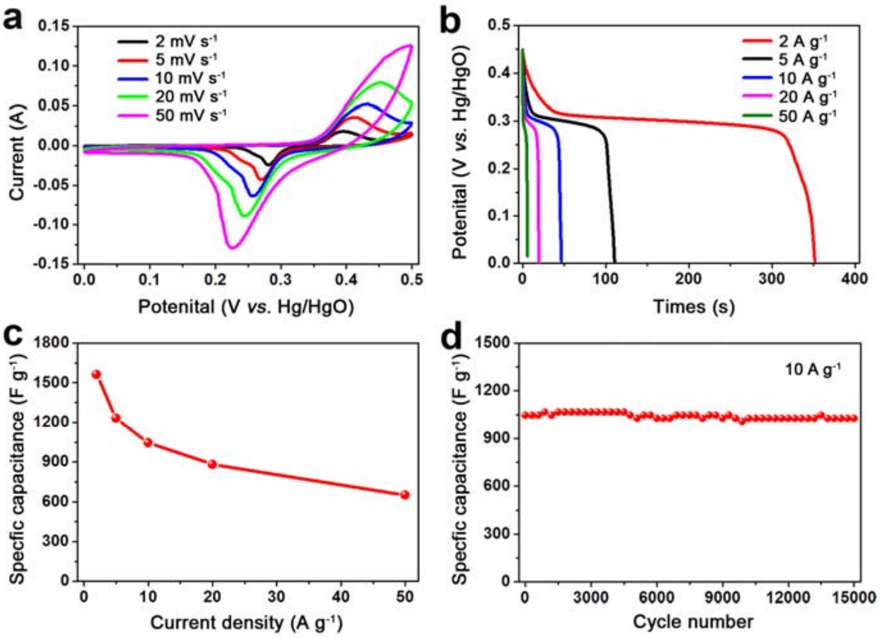

Figure 8.16 Electrochemical performance of yolk-shelled $Ni_{0.37}Co$-oxide nanoprisms as electrodes for HSCs: (a) CV curves at different scan rates, (b) discharge voltage profiles at different current densities, (c) capacitance as a function of current density, and (d) cycling performance at a current density of 10 A g^{-1}.

We have evaluated the electrochemical properties of the yolk-shelled $Ni_{0.37}Co$-oxide sample as an electrode material for HSCs in 6.0 M KOH solution. **Figure 8.16**a shows the representative CV tests of the $Ni_{0.37}Co$-oxide electrode with a cut-off voltage range of 0-0.50 V versus the Hg/HgO/1.0 M KOH reference electrode.

A set of pronounced redox peaks referring to Faradaic reactions of M-O/M-O-OH (M means Ni or Co) can be observed, which indicates the typical Faradaic behaviour of a battery-type electrode.[6, 155-158] With the increase of scan speed from 2 to 50 mV s^{-1}, the current density improves accordingly and the appearance of the CV profiles is well kept, indicating that the $Ni_{0.37}$Co-oxide electrode is favorable for ultrafast redox reactions. Galvanostatic charge-discharge tests are carried out in the cut-off potential range from 0 to 0.45 V (*vs.* Hg/HgO). The corresponding discharge curves tested at different current densities are shown in Figure 8.16b. Apparently, there are well-defined voltage platforms in all these discharge profiles, which further verifies its typical Faradaic nature. The capacitance as a function of the discharge current density is shown in Figure 8.16c. Encouragingly, the yolk-shelled $Ni_{0.37}$Co-oxide electrode delivers splendid specific capacitance of 1563, 1232, 1043 and 882 F g^{-1} at the discharge current densities of 2, 5, 10 and 20 A g^{-1}, respectively. Even at higher current density of 50 A g^{-1}, the value remains as high as 651 F g^{-1}. The cycling stability is further evaluated under repeated galvanostatic charge-discharge conditions at a fixed current of 10 A g^{-1}. Impressively, the electrode is very stable with a specific capacitance of 1026 F g^{-1} retained over 15,000 cycles, corresponding to a loss of only 2% (Figure 8.16d). As shown in **Figure 8.17**, the whole electrode maintains the integrity of the structure during the electrochemical reaction. As a comparison, the Ni-rich oxide ($Ni_{1.38}$Co-oxide) can also serve as a battery-type electrode with similar Faradaic behavior (**Figure 8.18**). Meanwhile, chronopotentiometry (CP) curves and cycle test indicate the $Ni_{1.38}$Co-oxide exhibits lower capacitance with much inferior electrochemical stability. Overall, the electrochemical performance of the yolk-shelled $Ni_{0.37}Co$-oxide electrode in the present study is comparable to many other Ni-Co mixed oxide based electrodes.[32, 98, 99, 139]

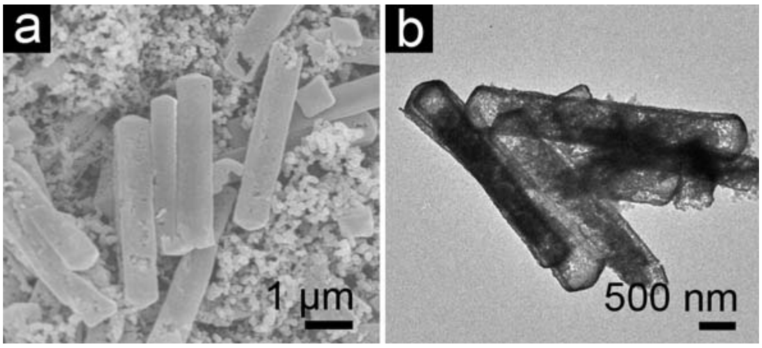

Figure 8.17 FESEM and TEM image of $Ni_{0.37}Co$-oxide prisms after 2000 discharge-charge cycles at 10 A g^{-1} as electrode for HSCs.

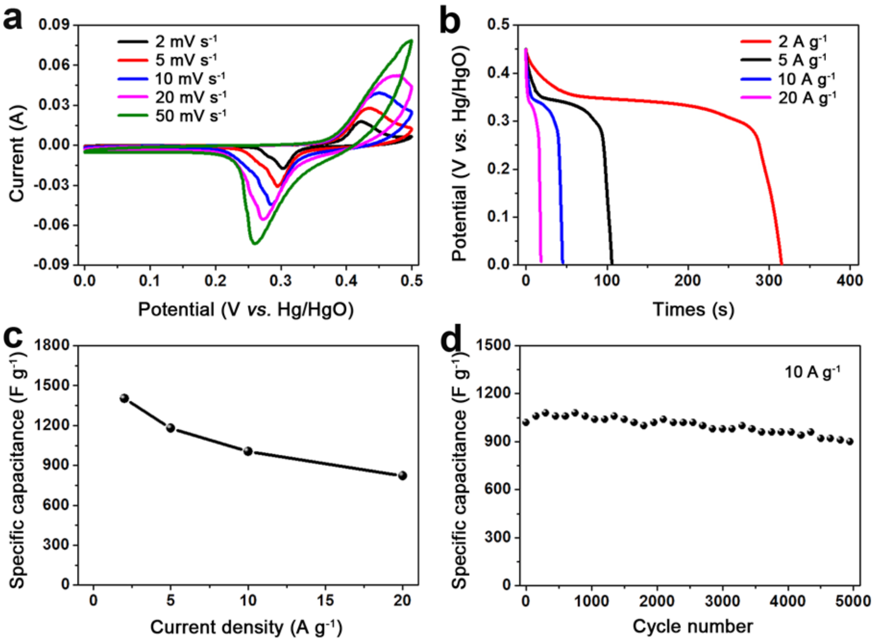

Figure 8.18 Electrochemical performance of yolk-shelled $Ni_{1.38}Co$-oxide nanoprisms as electrodes for HSCs: (a) CV curves at diverse sweep rates, (b) discharge voltage profiles at various current densities, (c) capacitance as a function of current density, and (d) cycling performance at a current density of 10 A g^{-1}.

Such desirable electrochemical activities with remarkable capacitance and outstanding cycle performance might be attributed to the distinct yolk-shell hollow structure. Specifically, the porous structure provides sufficient amount of electroactive sites and more effective transport of electrolyte through the active substance. Moreover, the yolk-shelled particles are structurally robust for accommodating the volume variation hence improving the cycling stability.

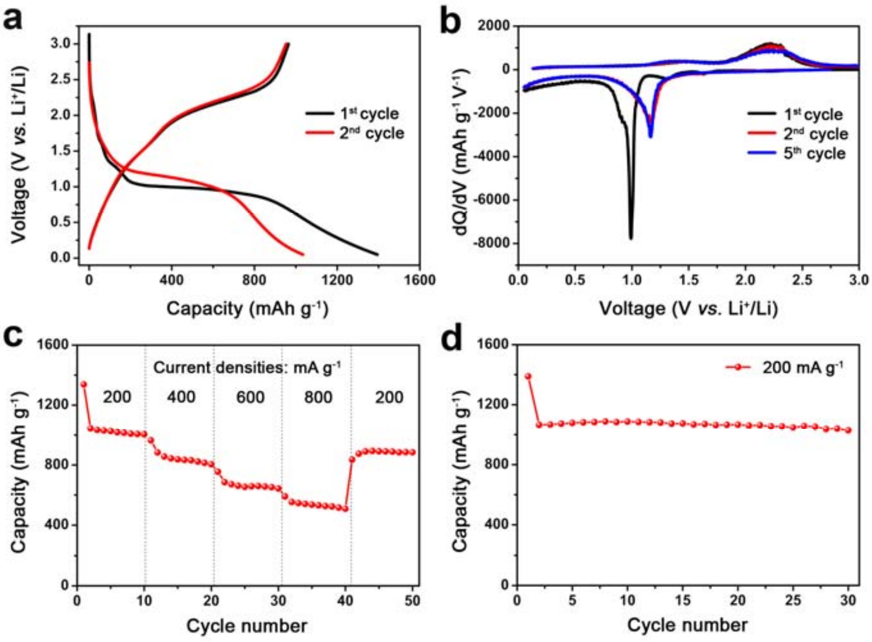

Figure 8.19 Electrochemical performance of yolk-shelled Ni$_{0.37}$Co-oxide nanoprisms for lithium storage: (a) galvanostatic discharge-charge voltage curves for the 1st and 2nd cycles, (b) the differential capacity *vs.* voltage profiles for the 1st, 2nd and 5th cycles at a constant current of 200 mA g^{-1}, (c) rate capability test at diverse current densities, and (d) cycling test at a constant current of 200 mA g^{-1}. All tests were carried out over the voltage range of 0.05-3.0 V vs. Li/Li$^+$.

Furthermore, we also evaluate their electrochemical properties as anodes for LIBs. The typical galvanostatic discharge-charge voltage curves at a fixed current of 200 mA g^{-1} are provided in **Figure 8.19**a. Notably, the yolk-shelled Ni$_{0.37}$Co-oxide particles deliver high initial discharge and charge capacities of 1394.4 and 964.5 mAh g^{-1}, respectively. The large inevitable capacity loss and low Coulombic efficiency for the 1st cycle are mainly attributed to irreversible side reactions within electrodes including the incomplete decomposition of the as-formed SEI film and restoration of metallic Ni and Co into the original oxides.[139, 159] To further study the mechanism of lithium storage in this $Ni_{0.37}$Co-oxide electrode, differential capacity *vs* voltage curves obtained at various cycles (Figure 8.19b) are carefully investigated. During the discharge process in the 1st cycle, a dominant inevitable cathodic peak located at 1.0 V can be observed, corresponding to reduction of NiO_x and CoO_x to metallic Ni and Co nanocrystals, respectively.[140, 160, 161] The decay in the peak current from next scans onwards reveals that some inevitable reactions might take place during the first cycle. The slight offset of peak location to higher potential might be due to the activation effect induced by the Li^+ insertion, as reported in previous works.[54, 112] Meanwhile, the two oxidation peaks with good reproducibility in the Li^+ ions extraction process centered at 1.4 V and 2.1 V can be attributed to oxidation of Ni and Co nanocrystals, respectively. Remarkably, the discharge and charge curves overlap very well from the second cycle onwards, demonstrating the well reversibility of the convention reactions. Galvanostatic measurements in Figure 8.19c demonstrate that these mesoporous yolk-shelled $Ni_{0.37}$Co-oxide particles can be reversibly cycled at 200 to 800 mA g^{-1} with high specific capacities of 1025 to 535 mAh g^{-1}. Of particular note, a high capacity of 884 mAh g^{-1} can be delivered as the current density finally returns to 200 mA g^{-1}, illustrating excellent stability. To assess the cycling stability, the electrode is charged and discharged at a fixed current of 200 mA g^{-1} at the potential from 0.05 to 3.0 V, as depicted in Figure 8.19d. Apart from the capacity loss during the 1st cycle, the discharge capacity of the anode decreases slightly and eventually delivers an invertible capacity of about 1028.5 mAh g^{-1} over 30 cycles, corresponding to 96% of the 2nd cycle discharge capacity.

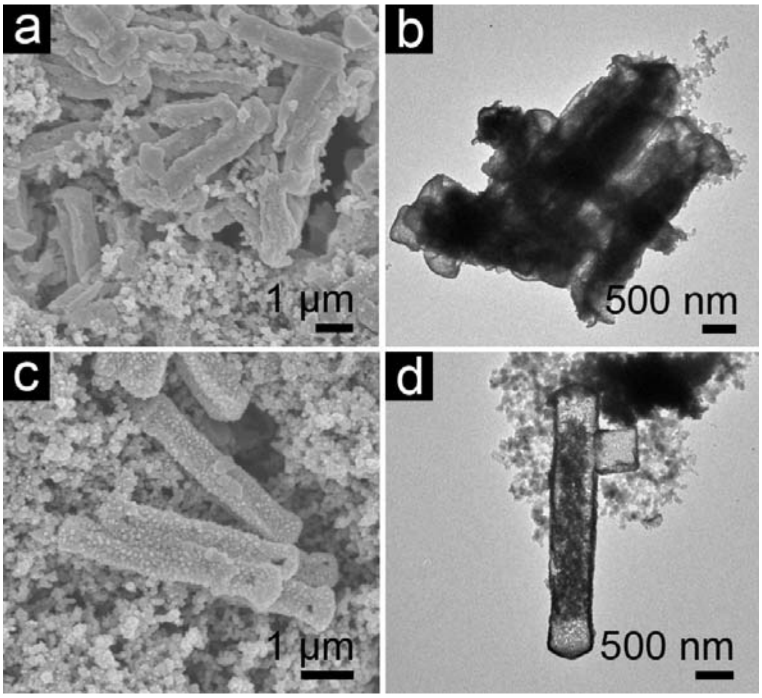

Figure 8.20 FESEM and TEM image of $Ni_{0.37}$Co-oxide prisms after 10 discharge-charge cycles at 200 mA g^{-1} as electrode for LIBs: (a, b) in their lithiated state; (c, d) in their delithiated state.

The post-mortem study indicates the yolk-shell structures can be generally retained with slight distortion after the conversion reactions, suggesting the robust nature of the architecture (**Figure 8.20**). As references, when employed as electrodes for lithium storage, the cycling performance for both the $Ni_{0.82}$Co-oxide and $Ni_{1.38}$Co-oxide is not so good compared to that of the $Ni_{0.37}$Co-oxide with poor capacity retention (**Figure 8.21**). Again, the enhanced lithium storage properties of these porous yolk-shelled $Ni_{0.37}$Co-oxide particles might be attributed to the special structural merits. Apparently, the small primary nanoparticles and pores provide shortened diffusion length of ions and boosted reaction kinetics. Besides, the hollow and porous feature could efficiently accommodate the structural expansion/contraction upon the repeated lithium uptake and removal processes.

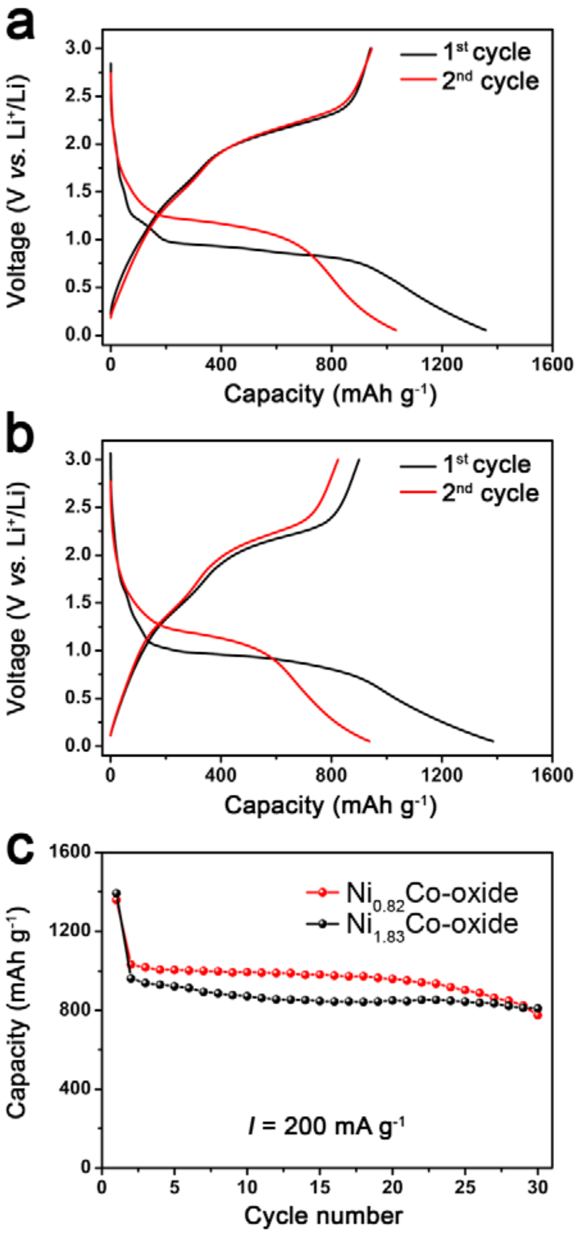

Figure 8.21 Electrochemical performance of $Ni_{0.82}$Co-oxide and $Ni_{1.38}$Co-oxide for lithium storage: galvanostatic discharge-charge voltage profiles for the 1st and 2nd cycles for (a) $Ni_{0.82}$Co-oxide and (b) $Ni_{1.38}$Co-oxide; (c) cycling test. All measurements were conducted over the potential range of 0.05-3.0 V *vs.* Li/Li^+ at a constant current of 200 mA g^{-1}.

8.4. Summary

In this Chapter, we prepare unique mesoporous Ni-Co mixed oxide nanoprisms with a yolk-shelled structure. The synthesis involves a facile solvothermal method for preparation of precursor particles and a following annealing process. The formation of the yolk-shell structure could be interpreted as a contraction process driven by thermodynamics. Owing to the unique structural features and desirable composition, the resultant mesoporous yolk-shell Ni-Co mixed oxides exhibit interesting electrochemical performance as electrodes for both hybrid supercapacitors and lithium ion batteries. Impressively, the $Ni_{0.37}Co$-oxide sample shows very high specific capacitance of over 1000 F g^{-1} and excellent long-term stability with capacitance retention of 98.0% after 15,000 charge-discharge cycles. Besides, these yolk-shelled $Ni_{0.37}Co$-oxide particles also manifest enhanced lithium storage properties.

Chapter 9. Concluding Remarks and Outlook

9.1. Concluding Remarks

As two typical electrical energy storage (EES) devices, lithium ion batteries (LIBs) and hybrid supercapacitors (HSCs) are promising technological choices for large-scale applications. The development of complex metal oxide brings the possibility to realize new generations of high-efficiency EES devices. This research project focuses the rational design and synthesis of two representative types of complex metal oxide including hybrid systems and ternary metal oxides with tailorable micro-/nanostructures, as well as their electrochemical performance as electrode material for LIBs and HSCs. The main results and critical findings are summarized as follows.

I. The construction of TiO_2@Fe_2O_3 and $NiCo_2O_4$@MnO_2 core-shell arrays as typical hybrid metal oxide systems.

In this research project, we report two hybrid metal oxide systems including TiO_2@Fe_2O_3 integrated electrodes and $NiCo_2O_4$@MnO_2 core-shell structures.

In the former case, we have designed a smart nanocomposite composed of aligned TiO_2 nanotube arrays (TNAs) with attached Fe_2O_3 hollow nanorods on both the outer and inner surface. The unique core-shell architecture has been created by introducing FeOOH nanospindles onto the TNAs with a follow-up thermal treatment in air. Benefitting from the desirable architecture and expected synergistic effects between components, the obtained hybrid structure exhibits enhanced conductivity and lithium storage properties compared with the individual TiO_2 nanotube arrays and most of the reported TiO_2-based 3D electrodes.

In order to further improve the conductivity of the entire hybrid system, we choose high conductive $NiCo_2O_4$ arrays on Ni foam as the 3D frame to build the heterogeneous $NiCo_2O_4$@MnO_2 core-shell nanowires via a facile solution based method. Owing to the hybrid effect on the conductivity and combined capacitive contribution from the mesoporous $NiCo_2O_4$ NW core and the ultrathin MnO_2 shell, the heterostructured arrays electrode delivers superior capacitance of 1.66 F cm^{-2} even at 20 mA cm^{-2} and remarkable rate performance and electrochemical stability as electrode for HSCs, which is much better than single $NiCo_2O_4$ arrays. These two examples demonstrate the feasibility and advantages of structural design of smart integrated hybrid metal oxides for high-efficiency EES system.

II. The formation of hierarchical $Co_xMn_{3-x}O_4$ arrays, $NiCo_2O_4$ micro-/nanostructures and yolk-shelled Ni-Co mixed oxides as representative ternary metal oxides.

Herein, we develop the three typical examples of ternary metal oxides systems are $Co_xMn_{3-x}O_4$ micro-/nanostructures array, $NiCo_2O_4$ hierarchical structures and yolk-shelled Ni-Co mixed oxide prisms.

Hierarchical $Co_xMn_{3-x}O_4$ micro-/nanostructures array has been developed through a facile two-step process. The obtained mesoporous $Co_xMn_{3-x}O_4$ micro-/nanostructures are composed of direct growth of well-separated wires or sheets, forming a stable 3D framework as a LIBs anode. The distinct micro-/nanostructures inherit both the superiorities of nanosized subunits and micro-/submicrosized assemblies. As a result, the hierarchical $Co_xMn_{3-x}O_4$ structures exhibit predominant electrochemical performances demonstrated by comparable specific capacities (540-207 mAh g^{-1}) at high rates (1-10 C).

Similar to $Co_xMn_{3-x}O_4$ system, hierarchical $NiCo_2O_4$ structures composed of NWs or NSs building blocks are successfully developed via a straightforward strategy without conductive substrates. The specific morphologies were easily tuned through simple regulation of the composition and volume of the reaction solvent. Owing to the structural merits, the two $NiCo_2O_4$ electrodes exhibit appealing electrochemical performance as advanced electrodes for HSCs. In particular, the flower-like hierarchical $NiCo_2O_4$ architecture delivers a higher specific capacitance of 1333 F g^{-1} with a low capacitance loss of over 1500 cycles. These two hierarchical systems reveal the huge advantages of micro-/nanostructures as potential electrodes for EES in term of better mechanical stability and boosted electrochemical activities.

Apart from the hierarchical micro-/nanostructures, hollow structures are one of classical configurations that can improve the performance of EES. Starting with prism-like metal acetate hydroxide, Ni-Co mixed oxide nanoprisms with yolk-shelled characteristic and tunable chemical element can be prepared by a simple oxidation process in air. The formation mechanism can be attributed to the fast thermally driven contraction process. Owing to the unique structural features and desirable composition, the resultant mesoporous yolk-shell Ni-Co mixed oxides exhibit interesting electrochemical performance as electrodes for both HSCs and LIBs. Impressively, the $Ni_{0.37}$Co-oxide sample shows very high specific capacitance of over 1000 F g^{-1} and excellent long-term stability over 15000 cycles. Besides, these yolk-shelled $Ni_{0.37}$Co-oxide particles also manifest enhanced lithium storage properties.

In summary the successes of above systems further confirm the superiorities of complex metal oxides as potential electrodes for EES systems. The synergistic effect from different components or compositions and the nanostructuring strategies are crucial to realize the preparation of electrodes with splendid energy storage performance. Generally speaking, the combined metal oxides with different energy storage mechanisms can make full use of electrolyte or afford additional capacity to total electrochemical energy storage. Moreover, each nanostructuring category has its specialty. To be specific, core-shelled hierarchical structure can ensure good electrical contact between active components and large surface area for the electrochemical reactions. Therefore, electron transport can be facilitated and more active sites are guaranteed. Meanwhile, yolk-shell structure is a special kind of hollow architectures. The hollow interior could not only act as a barrier to prevent the encapsulated electroactive nanoparticles from aggregation, but also efficiently alleviate pulverization of the electrode by accommodating the large volume variation associated with charge/discharge cycling. More importantly, compared to the single-shelled hollow structures, core-shell design can improve the volumetric energy density of the active material to further increase the volumetric energy and power densities of electrodes. The findings in this project greatly expand our knowledge in the rational design and synthesis of complex metal oxides, and also pave the way to overcome the bottlenecks of current electrode materials for next-generation LIBs and HSCs.

9.2. Outlook

Despite the great progress in the synthesis of complex metal oxides during the recent years and their applications for LIBs and HSCs, the deployment of advanced electrodes based on these complex metal oxides is still at its early stage. Therefore, researchers still face great challenges towards both the synthesis and practical application of these novel materials. Along these lines, several possible suggestions provided below for the future research on complex metal oxides in electrochemical energy storage applications.

1) To develop new facile and cost-effective methods to improve the loading mass of the integrated electrodes. From the investigations carried out by our group and many other researchers, the employment of chemical approaches for can acquire well-defined 3D arrays with controlled architectures. These binder-free systems can provide better electrical contact between the active materials and current collector. However, it's well accepted the loading mass of active materials from these synthetic methods is too low (usually less than 1 mg cm^{-2}) to meet the requirement for the practical applications (more than 10

mg cm^{-2}). Meanwhile, physical method can be applied for the large-scale production of distinct structures with high loading mass. Deficiencies are the relatively high cost. To integrate the chemical and physical approaches into the manufacture procedure might enable the possibility to obtain binder-free electrode with high loading mass.

2) In-depth investigation of the inner relationship between the structural features and the improved the electrochemical performance of complex metal oxides. Both experimental and theoretical analysis would be necessary to better illustrate the roles of structural/compositional features, for example, geometric shape, exposed facets, porosity and surface area on the electrochemical reactions such as ion transfer and diffusion, secondary reactions, mechanical variance, and so on. A better understanding of the fundamental chemistry would possibly offer some directions to optimize the material selection and structural design of complex metal oxides for the maximization of energy density and powder density of the devices.
3) The realization of full cell tests with complex metal oxide-based electrodes. Demonstration of prototype full cells using complex metal oxide-based would be of great value towards both the scientific research and practical use. Many technical issues should be addressed, such as the selection of counter electrode materials, proper electrolytes and specific packaging requirements. Moreover, with the rapid development of hand-held portable devices and wearable devices, the research on flexible power supply is highly desirable. And thus, to

fabricate the full flexible device using complex metal oxides is another fascinating topic.

Complete List of Publications

[1] **L. Yu**, B. Y. Xia, X. Wang,* X. W. Lou,* General Formation of M-MoS_3 (M = Co, Ni) Hollow Structures with Enhanced Electrocatalytic Activity for Hydrogen Evolution, ***Adv. Mater.***, DOI: 10.1002/adma.201504024 (**2015**).

[2] X. Y. Yu,+ **L. Yu**,+ X. W. Lou,* Metal Sulfide Hollow Nanostructures for Electrochemical Energy Storage, invited review, ***Adv. Energy Mater.***, DOI: 10.1002/aenm.201501333 (**2015**). (+ **Contribute equally**)

[3] **L. Yu**, B. Y. Guan, W. Xiao,* X. W. Lou,* Formation of Yolk-shelled Ni-Co Mixed Oxide Nanoprisms with Enhanced Electrochemical Performance for Hybrid Supercapacitors and Lithium ion Batteries, ***Adv. Energy Mater.***, 5, 1500981 (**2015**).

[4] L. F. Shen,+ **L. Yu**,+ H. B. Wu, X. Y. Yu, X. G. Zhang, X. W. Lou,* Formation of Nickel Cobalt Sulfide Ball-in-Ball Hollow Spheres with Enhanced Electrochemical Pseudocapacitive Properties, ***Nat. Commun.***, 6, 6694 (**2015**). (+ **Contribute equally**)

[5] **L. Yu**, L. Zhang, H. B. Wu, X. W. Lou,* Formation of $Ni_xCo_{3-x}S_4$ Hollow Nano-prisms with Enhanced Pseudo-capacitive Properties, ***Angew Chem. Int. Ed.***, 53, 3711 (**2014**). (**Highlighted as a VIP paper**)

[6] **L. Yu**, H. B. Wu, X. W. Lou,* Mesoporous $Li_4Ti_5O_{12}$ Hollow Spheres with Enhanced Lithium Storage Capability, ***Adv. Mater.***, *25*, 2296 (**2013)**.

[7] **L. Yu**, L. Zhang, H. B. Wu, G. Q. Zhang, X. W. Lou,* Controlled Synthesis of Hierarchical $Co_xMn_{3-x}O_4$ Array Micro-/Nanostructures as Integrated Electrodes for Lithium-ion Batteries, ***Energy Environ. Sci.***, *6*, 2664 (**2013**).

[8] **L. Yu**, G. Q. Zhang, C. Z. Yuan,* X. W. Lou,* Hierarchical $NiCo_2O_4$@MnO_2 Core-shell Heterostructured Nanowire Arrays on Ni foam as High-performance Supercapacitor Electrodes, ***Chem. Commun.***, 2, 137 (**2013**)

[9] **L. Yu,** H. Wu, T. Wu, C. Z. Yuan,* Morphology-controlled Fabrication of Hierarchical Mesoporous $NiCo_2O_4$ Micro-/Nanostructures and Their Intriguing Application in Electrochemical Capacitors, ***RSC Adv.***, 3, 23709 (**2013**).

[10] **L. Yu**, Z. Y. Wang, L. Zhang, H. B. Wu, X. W. Lou,* TiO_2 Nanotube Arrays Grafted with Fe_2O_3 Hollow Nanorods as Integrated Electrodes for Lithium-ion Batteries, ***J. Mater. Chem. A***, 1, 122 (**2013**).

[11] H. B. Wu$^+$, B. Y. Xia,$^+$ **L. Yu**, X. Y. Yu, X. W. Lou,* Porous Molybdenum Carbide Nano-octahedrons Synthesized via Confined Carburization in Metal-Organic Frameworks for Efficient Hydrogen Production, ***Nat. Commun.***, 6, 6512 (**2015**). ($^+$ **Contribute equally**)

[12] J. M. Wang$^+$, L. Zhang$^+$, **L. Yu**, Z. H. Jiao, H. Q. Xie, X. W. Lou,* X. W. Sun,* A Bi-functional Device for Self-powered Electrochromic Window and Self-rechargeable Transparent Battery, ***Nat. Commun.***, 5, 4921 (**2014**). ($^+$ **Contribute equally**)

[13] Y. Guo, **L. Yu**, C. Y. Wang, Z. Lin,* X. W. Lou,* Hierarchical Tubular Structures Composed of Mn-based Mixed Metal Oxide Nanoflakes with Enhanced Electrochemical Properties, ***Adv. Funct. Mater.***, in press (**2015**).

[14] H. Hu, **L. Yu**, X. H. Gao, Z. Lin,* X. W. Lou,* Hierarchical Tubular Structures Constructed from Ultrathin TiO_2(B) Nanosheets for Highly Reversible Lithium Storage, ***Energy Environ. Sci.***, 8, 1480 (**2015**).

[15] X. Y. Yu, **L. Yu**, H. B. Wu, X. W. Lou,* Formation of Nickel Sulfide Nanoframes from MOFs with Enhanced Pseudocapacitive and Electrocatalytic Properties, ***Angew Chem. Int. Ed.***, 54, 5331 (**2015**).

[16] X. Y. Yu, **L. Yu**, H. B. Wu, F. X. Ma, X. W. Lou,* Rutile TiO_2 Nanoboxes with Superior Lithium Storage Properties, ***Angew Chem. Int. Ed.***, *54*, 4001 (**2015**)

[17] L. F. Shen, **L. Yu**, X. Y. Yu, X. G. Zhang, X. W. Lou,* Self-templated Formation of Uniform $NiCo_2O_4$ Hollow Spheres with Complex Interior

Structure for Lithium-ion Batteries and Supercapacitors, ***Angew Chem. Int. Ed.***, *54,* 1868 (**2015**).

[18] X. Y. Yu, **L. Yu**, L. F. Shen, X. H. Song, H. Y. Chen, X. W. Lou,* General Formation of MS (M=Ni, Cu, Mn) Box-in-Box Hollow Structures with Enhanced Pseudocapacitive Properties, ***Adv. Funct. Mater.***, *24*, 7440 (**2014**).

[19] G. X. Gao, **L. Yu**, H. B. Wu, X. W. Lou,* Hierarchical Tubular Structures Constructed by Carbon-coated α-Fe_2O_3 Nanorods for Highly Reversible Lithium Storage, ***Small***, *10*, 1741 (**2014**).

[20] G. Q. Zhang, **L. Yu**, H. E. Hoster, X. W. Lou,* Synthesis of One-Dimensional Hierarchical NiO Hollow Nanostructure with Enhanced Supercapacitive Performance, ***Nanoscale***, 5, 877 (**2013**).

[21] G. Q. Zhang, **L. Yu**, H. B. Wu, H. E. Hoster, X. W. Lou,* Formation of Ball-in-ball Hollow $ZnMn_2O_4$ Microspheres as A High-performance Anode for Lithium-ion Batteries, ***Adv. Mater.***, 24, 4609 (**2012**).

[22] Y. Liu, **L. Yu**, Y. Hu,* C. F. Guo, F. M. Zhang, X. W. Lou,* A Magnetically Separable Photocatalyst based on Nest-Like γ-Fe_2O_3/ZnO Double-shelled Hollow Structures, ***Nanoscale***, 4, 183 (**2012**).

[23] H. B. Wu, G. Q. Zhang, **L. Yu**, X. W. Lou,* One-dimensional metal oxide-carbon hybrid nanostructures for electrochemical energy storage, invited review, submitted (**2015**).

[24] H. Y. Wang, F. X. Xiao, **L. Yu**, B. Liu,* X. W. Lou,* Hierarchical α-MnO_2 Nanowires@$Ni_{1-x}Mn_xO_y$ Nanoflakes Core-Shell Nanostructures for Supercapacitors, ***Small***, *10*, 3181 (**2014**).

[25] L. L. Li, H. B. Wu, **L. Yu**, S. Madhavi,* X. W. Lou,* A General Method to Grow Porous α-Fe_2O_3 Nanosheets on Substrates as Integrated Electrodes for Lithium-ion Batteries, ***Adv. Mater. Interfaces***, *1*, 1400050 (**2014**).

[26] A. Q. Pan, H. B. Wu, **L. Yu**, X. W. Lou,* Template-free Formation of Uniform VO_2 Hollow Microspheres with Different Interiors and Their Conversion to V_2O_5 for Lithium-ion Batteries, ***Angew Chem. Int. Ed.***, 52,

2226 (**2013**). (**Selected as a "hot" paper by the Editor**)

[27] B. Wang, H. B. Wu, **L. Yu**, R. Xu, T. T. Lim, X. W. Lou,* Template-free Formation of Uniform Urchin-like α-FeOOH Hollow Spheres with Superior Capability for Water Treatment, ***Adv. Mater.,*** 24, 1111 (**2012**).

[28] A. Q. Pan, H. B. Wu, **L. Yu**, T. Zhu, X. W. Lou,* Synthesis of Hierarchical 3D Vanadium Oxide Microstructures as High-capacity Cathode Materials for Lithium-ion Batteries, ***ACS Appl. Mater. Interfaces***, 4, 3874 (**2012**).

[29] L. L. Li, S. J. Peng, H. B. Wu, **L. Yu**, S. Madhavi,* X. W. Lou,* A Flexible Quasi-solid-state Asymmetric Electrochemical Capacitor Based on Hierarchical Porous V_2O_5 Nanosheets on Carbon Nanofibers, ***Adv. Energy Mater.***, Early View (**2015**).

[30] G. Q. Zhang, B. Y. Xia, C. Xiao, **L. Yu**, X. Wang, Y. Xie,* X. W. Lou,* General Formation of Complex Tubular Nanostructures of Metal Oxides for the Oxygen Reduction Reaction and Lithium-ion Batteries. ***Angew Chem. Int. Ed.***, *52*, 8643 (**2013**). (**Highlighted by the Editors as a "Hot" paper, and back Cover**)

[31] L. Zhang, G. Q. Zhang, H. B. Wu, **L. Yu**, X. W. Lou,* Hierarchical Tubular Structures Constructed by Carbon-coated SnO_2 Nanoplates for Lithium Storage, ***Adv. Mater.***, *25*, 2589 (**2013**).

[32] X. H. Song, T. Ding, L. Yao, M. Lin, R. L. S. Tan, C. C. Liu, K. Sokol, **L. Yu**, X. W. Lou, H. Y. Chen,* On the Origin and Underappreciated Effects of Ion Doping in Silica, ***Small***, Early View (**2015**).

References

[1] B. Dunn, H. Kamath, J. M. Tarascon, *Science* **2011**, *334*, 928.

[2] J. Liu, J. G. Zhang, Z. G. Yang, J. P. Lemmon, C. Imhoff, G. L. Graff, L. Y. Li, J. Z. Hu, C. M. Wang, J. Xiao, G. Xia, V. V. Viswanathan, S. Baskaran, V. Sprenkle, X. L. Li, Y. Y. Shao, B. Schwenzer, *Adv. Funct. Mater.* **2013**, *23*, 929.

[3] C. Z. Yuan, H. B. Wu, Y. Xie, X. W. Lou, *Angew. Chem. Int. Ed.* **2014**, *53*, 1488.

[4] A. L. M. Reddy, S. R. Gowda, M. M. Shaijumon, P. M. Ajayan, *Adv. Mater.* **2012**, *24*, 5045.

[5] D. P. Dubal, O. Ayyad, V. Ruiz, P. Gomez-Romero, *Chem. Soc. Rev.* **2015**, *44*, 1777.

[6] P. Simon, Y. Gogotsi, B. Dunn, *Science* **2014**, *343*, 1210.

[7] G. P. Wang, L. Zhang, J. J. Zhang, *Chem. Soc. Rev.* **2012**, *41*, 797.

[8] J. Jiang, Y. Y. Li, J. P. Liu, X. T. Huang, C. Z. Yuan, X. W. Lou, *Adv. Mater.* **2012**, *24*, 5166.

[9] T. T. Truong, Y. Z. Liu, Y. Ren, L. Trahey, Y. G. Sun, *ACS Nano* **2012**, *6*, 8067.

[10] Z. N. Yu, L. Tetard, L. Zhai, J. Thomas, *Energy Environ. Sci.* **2015**, *8*, 702.

[11] Z. Y. Wang, L. Zhou, X. W. Lou, *Adv. Mater.* **2012**, *24*, 1903.

[12] H. B. Wu, J. S. Chen, H. H. Hng, X. W. Lou, *Nanoscale* **2012**, *4*, 2526.

[13] X. Xu, W. Liu, Y. Kim, J. Cho, *Nano Today* **2014**, *9*, 604.

[14] X. H. Rui, H. T. Tan, Q. Y. Yan, *Nanoscale* **2014**, *6*, 9889.

[15] M. R. Gao, Y. F. Xu, J. Jiang, S. H. Yu, *Chem. Soc. Rev.* **2013**, *42*, 2986.

[16] P. Simon, Y. Gogotsi, B. Dunn, *Science* **2014**, *343*, 1210.

[17] P. Simon, Y. Gogotsi, *Nat. Mater.* **2008**, *7*, 845.

[18] M. Salari, S. H. Aboutalebi, K. Konstantinov, H. K. Liu, *Phys. Chem. Chem. Phys.* **2011**, *13*, 5038.

[19] A. S. Arico, P. Bruce, B. Scrosati, J. M. Tarascon, W. Van Schalkwijk, *Nat. Mater.* **2005**, *4*, 366.

[20] A. Debart, A. J. Paterson, J. Bao, P. G. Bruce, *Angew. Chem. Int. Ed.* **2008**, *47*, 4521.

[21] Y. G. Guo, J. S. Hu, L. J. Wan, *Adv. Mater.* **2008**, *20*, 2878.

[22] A. Manthiram, A. V. Murugan, A. Sarkar, T. Muraliganth, *Energy Environ. Sci.* **2008**, *1*, 621.

[23] F. Hao, J. Zhong, P. L. Liu, K. Y. You, C. Wei, H. J. Liu, H. A. Luo, *J. Mol. Catal. A: Chem.* **2011**, *351*, 210.

[24] X. Y. Lai, J. E. Halpert, D. Wang, *Energy Environ. Sci.* **2012**, *5*, 5604.

[25] W. Zhou, C. Cheng, J. P. Liu, Y. Y. Tay, J. Jiang, X. T. Jia, J. X. Zhang, H. Gong, H. H. Hng, T. Yu, H. J. Fan, *Adv. Funct. Mater.* **2011**, *21*, 2439.

[26] G. F. Ortiz, I. Hanzu, P. Lavela, P. Knauth, J. L. Tirado, T. Djenizian, *Chem. Mater.* **2010**, *22*, 1926.

[27] J. A. Yan, A. Sumboja, E. Khoo, P. S. Lee, *Adv. Mater.* **2011**, *23*, 746.

[28] J. P. Liu, J. Jiang, C. W. Cheng, H. X. Li, J. X. Zhang, H. Gong, H. J. Fan, *Adv. Mater.* **2011**, *23*, 2076.

[29] C. Guan, X. H. Xia, N. Meng, Z. Y. Zeng, X. H. Cao, C. Soci, H. Zhang, H. J. Fan, *Energy Environ. Sci.* **2012**, *5*, 9085.

[30] J. S. Chen, C. M. Li, W. W. Zhou, Q. Y. Yan, L. A. Archer, X. W. Lou, *Nanoscale* **2009**, *1*, 280.

[31] J. Liu, H. Xia, D. F. Xue, L. Lu, *J. Am. Chem. Soc.* **2009**, *131*, 12086.

[32] H. Hu, B. Y. Guan, B. Y. Xia, X. W. Lou, *J. Am. Chem. Soc.* **2015**, *137*, 5590.

[33] S. W. Kim, H. W. Lee, P. Muralidharan, D. H. Seo, W. S. Yoon, D. K. Kim, K. Kang, *Nano Res.* **2011**, *4*, 505.

[34] J. Pu, J. Wang, X. Q. Jin, F. L. Cui, E. H. Sheng, Z. H. Wang, *Electrochim. Acta* **2013**, *106*, 226.

[35] L. Hu, H. Zhong, X. R. Zheng, Y. M. Huang, P. Zhang, Q. W. Chen, *Sci. Rep.* **2012**, *2*, 986.

[36] C. Z. Yuan, J. Y. Li, L. R. Hou, L. Yang, L. F. Shen, X. G. Zhang, *J. Mater. Chem.* **2012**, *22*, 16084.

[37] G. Q. Zhang, X. W. Lou, *Adv. Mater.* **2013**, *25*, 976.

[38] B. Liu, J. Zhang, X. F. Wang, G. Chen, D. Chen, C. W. Zhou, G. Z. Shen, *Nano Lett.* **2012**, *12*, 3005.

[39] Y. F. Deng, Q. M. Zhang, S. D. Tang, L. T. Zhang, S. N. Deng, Z. C. Shi, G. H. Chen, *Chem. Commun.* **2011**, *47*, 6828.

[40] G. Q. Zhang, L. Yu, H. B. Wu, H. E. Hoster, X. W. Lou, *Adv. Mater.* **2012**, *24*, 4609.

[41] S. J. Peng, L. L. Li, Y. X. Hu, M. Srinivasan, F. Y. Cheng, J. Chen, S. Ramakrishna, *Acs Nano* **2015**, *9*, 1945.

[42] J. P. Liu, Y. Y. Li, H. J. Fan, Z. H. Zhu, J. Jiang, R. M. Ding, Y. Y. Hu, X. T. Huang, *Chem. Mater.* **2010**, *22*, 212.

[43] X. Y. Xue, Z. H. Chen, L. L. Xing, S. Yuan, Y. J. Chen, *Chem. Commun.* **2011**, *47*, 5205.

[44] Y. Sharma, N. Sharma, G. V. S. Rao, B. V. R. Chowdari, *Chem. Mater.* **2008**, *20*, 6829.

[45] G. D. Du, Z. P. Guo, P. Zhang, Y. Li, M. B. Chen, D. Wexler, H. K. Liu, *J. Mater. Chem.* **2010**, *20*, 5689.

[46] Y. L. Wang, J. J. Xu, H. Wu, M. Xu, Z. Peng, G. F. Zheng, *J. Mater. Chem.* **2012**, *22*, 21923.

[47] Z. Y. Wang, Z. C. Wang, S. Madhavi, X. W. Lou, *J. Mater. Chem.* **2012**, *22*, 2526.

[48] S. Park, S. D. Seo, S. Lee, S. W. Seo, K. S. Park, C. W. Lee, D. W. Kim, K. S. Hong, *J. Phys. Chem. C* **2012**, *116*, 21717.

[49] W. Q. Zeng, F. P. Zheng, R. Z. Li, Y. Zhan, Y. Y. Li, J. P. Liu, *Nanoscale* **2012**, *4*, 2760.

[50] Z. X. Yang, G. D. Du, Q. Meng, Z. P. Guo, X. B. Yu, Z. X. Chen, T. L. Guo, R. Zeng, *RSC Adv.* **2011**, *1*, 1834.

[51] Y. S. Luo, J. S. Luo, J. Jiang, W. W. Zhou, H. P. Yang, X. Y. Qi, H. Zhang, H. J. Fan, D. Y. W. Yu, C. M. Li, T. Yu, *Energy Environ. Sci.* **2012**, *5*, 6559.

[52] C. Guan, X. L. Li, Z. L. Wang, X. H. Cao, C. Soci, H. Zhang, H. J. Fan, *Adv.*

Mater. **2012**, *24*, 4186.

[53] X. H. Tang, H. J. Li, Z. H. Liu, Z. P. Yang, Z. L. Wang, *J. Power Sources* **2011**, *196*, 855.

[54] X. H. Lu, T. Zhai, X. H. Zhang, Y. Q. Shen, L. Y. Yuan, B. Hu, L. Gong, J. Chen, Y. H. Gao, J. Zhou, Y. X. Tong, Z. L. Wang, *Adv. Mater.* **2012**, *24*, 938.

[55] L. Q. Mai, F. Yang, Y. L. Zhao, X. Xu, L. Xu, Y. Z. Luo, *Nat. Commun.* **2011**, *2*, 381.

[56] L. H. Bao, J. F. Zang, X. D. Li, *Nano Lett.* **2011**, *11*, 1215.

[57] H. Pang, J. W. Deng, J. M. Du, S. J. Li, J. Li, Y. H. Ma, J. S. Zhang, J. Chen, *Dalton Trans.* **2012**, *41*, 10175.

[58] J. A. Yan, E. Khoo, A. Sumboja, P. S. Lee, *ACS Nano* **2010**, *4*, 4247.

[59] D. Morgan, A. Van der Ven, G. Ceder, *Electrochem. Solid-State Lett.* **2004**, *7*, A30.

[60] D. W. Kim, Y. D. Ko, J. G. Park, B. K. Kim, *Angew. Chem. Int. Ed.* **2007**, *46*, 6654.

[61] Y. Sharma, N. Sharma, G. V. S. Rao, B. V. R. Chowdari, *Adv. Funct. Mater.* **2007**, *17*, 2855.

[62] Y. Sharma, N. Sharma, G. V. S. Rao, B. V. R. Chowdari, *Electrochim. Acta* **2008**, *53*, 2380.

[63] L. Zhou, D. Y. Zhao, X. W. Lou, *Adv. Mater.* **2012**, *24*, 745.

[64] Y. Wang, D. W. Su, A. Ung, J. H. Ahn, G. X. Wang, *Nanotechnology* **2012**, *23*.

[65] C. Yuan, J. Li, L. Hou, X. Zhang, L. Shen, X. W. Lou, *Adv. Funct. Mater.* **2012**, *22*, 4592.

[66] J. F. Li, S. L. Xiong, X. W. Li, Y. T. Qian, *Nanoscale* **2013**, *5*, 2045.

[67] J. Liu, C. P. Liu, Y. L. Wan, W. Liu, Z. S. Ma, S. M. Ji, J. B. Wang, Y. C. Zhou, P. Hodgson, Y. C. Li, *Crystengcomm* **2013**, *15*, 1578.

[68] R. Alcantara, M. Jaraba, P. Lavela, J. L. Tirado, *Chem. Mater.* **2002**, *14*, 2847.

[69] L. Hu, H. Zhong, X. R. Zheng, Y. M. Huang, P. Zhang, Q. W. Chen, *Sci. Rep.* **2012**, *2*, 986.

[70] J. Chen, L. N. Xu, W. Y. Li, X. L. Gou, *Adv. Mater.* **2005**, *17*, 582.

[71] M. V. Reddy, T. Yu, C. H. Sow, Z. X. Shen, C. T. Lim, G. V. S. Rao, B. V. R. Chowdari, *Adv. Funct. Mater.* **2007**, *17*, 2792.

[72] W. M. Zhang, X. L. Wu, J. S. Hu, Y. G. Guo, L. J. Wan, *Adv. Funct. Mater.* **2008**, *18*, 3941.

[73] D. Larcher, C. Masquelier, D. Bonnin, Y. Chabre, V. Masson, J. B. Leriche, J. M. Tarascon, *J. Electrochem. Soc.* **2003**, *150*, A133.

[74] D. Larcher, D. Bonnin, R. Cortes, I. Rivals, L. Personnaz, J. M. Tarascon, *J. Electrochem. Soc.* **2003**, *150*, A1643.

[75] M. G. Kim, J. Cho, *Adv. Funct. Mater.* **2009**, *19*, 1497.

[76] C. Kim, M. Noh, M. Choi, J. Cho, B. Park, *Chem. Mater.* **2005**, *17*, 3297.

[77] B. Wang, J. S. Chen, H. B. Wu, Z. Y. Wang, X. W. Lou, *J. Am. Chem. Soc.* **2011**, *133*, 17146.

[78] Z. Y. Wang, D. Y. Luan, S. Madhavi, Y. Hu, X. W. Lou, *Energy Environ. Sci.* **2012**, *5*, 5252.

[79] Z. M. Cui, L. Y. Hang, W. G. Song, Y. G. Guo, *Chem. Mater.* **2009**, *21*, 1162.

[80] X. L. Wu, Y. G. Guo, L. J. Wan, C. W. Hu, *J. Phys. Chem. C* **2008**, *112*, 16824.

[81] H. Liu, G. X. Wang, J. Park, J. Wang, H. Liu, C. Zhang, *Electrochim. Acta* **2009**, *54*, 1733.

[82] J. S. Chen, T. Zhu, X. H. Yang, H. G. Yang, X. W. Lou, *J. Am. Chem. Soc.* **2010**, *132*, 13162.

[83] G. M. Zhou, D. W. Wang, F. Li, L. L. Zhang, N. Li, Z. S. Wu, L. Wen, G. Q. Lu, H. M. Cheng, *Chem. Mater.* **2010**, *22*, 5306.

[84] G. K. Mor, O. K. Varghese, M. Paulose, K. Shankar, C. A. Grimes, *Sol. Energy Mater. Sol. Cells* **2006**, *90*, 2011.

[85] M. D. Ye, X. K. Xin, C. J. Lin, Z. Q. Lin, *Nano Lett.* **2011**, *11*, 3214.

[86] Y. Piao, J. Kim, H. Bin Na, D. Kim, J. S. Baek, M. K. Ko, J. H. Lee, M. Shokouhimehr, T. Hyeon, *Nat. Mater.* **2008**, *7*, 242.

[87] G. F. Ortiz, I. Hanzu, T. Djenizian, P. Lavela, J. L. Tirado, P. Knauth, *Chem. Mater.*

2009, *21*, 63.

[88] G. F. Ortiz, I. Hanzu, P. Lavela, J. L. Tirado, P. Knauth, T. Djenizian, *J. Mater. Chem.* **2010**, *20*, 4041.

[89] L. G. Xue, Z. Wei, R. S. Li, J. L. Liu, T. Huang, A. S. Yu, *J. Mater. Chem.* **2011**, *21*, 3216.

[90] P. Poizot, S. Laruelle, S. Grugeon, L. Dupont, J. M. Tarascon, *Nature* **2000**, *407*, 496.

[91] Y. F. Shi, B. K. Guo, S. A. Corr, Q. H. Shi, Y. S. Hu, K. R. Heier, L. Q. Chen, R. Seshadri, G. D. Stucky, *Nano Lett.* **2009**, *9*, 4215.

[92] S. Laruelle, S. Grugeon, P. Poizot, M. Dolle, L. Dupont, J. M. Tarascon, *J. Electrochem. Soc.* **2002**, *149*, A627.

[93] K. Y. Xie, Z. G. Lu, H. T. Huang, W. Lu, Y. Q. Lai, J. Li, L. M. Zhou, Y. X. Liu, *J. Mater. Chem.* **2012**, *22*, 5560.

[94] H. B. Wu, J. S. Chen, X. W. Lou, H. H. Hng, *Nanoscale* **2011**, *3*, 4082.

[95] J. S. Chen, Y. L. Tan, C. M. Li, Y. L. Cheah, D. Y. Luan, S. Madhavi, F. Y. C. Boey, L. A. Archer, X. W. Lou, *J. Am. Chem. Soc.* **2010**, *132*, 6124.

[96] Z. Y. Wang, D. Y. Luan, S. Madhavi, C. M. Li, X. W. Lou, *Chem. Commun.* **2011**, *47*, 8061.

[97] H. W. Wang, Z. A. Hu, Y. Q. Chang, Y. L. Chen, H. Y. Wu, Z. Y. Zhang, Y. Y. Yang, *J. Mater. Chem.* **2011**, *21*, 10504.

[98] H. Jiang, J. Ma, C. Z. Li, *Chem. Commun.* **2012**, *48*, 4465.

[99] Q. F. Wang, B. Liu, X. F. Wang, S. H. Ran, L. M. Wang, D. Chen, G. Z. Shen, *J. Mater. Chem.* **2012**, *22*, 21647.

[100] X. H. Xia, J. P. Tu, Y. Q. Zhang, X. L. Wang, C. D. Gu, X. B. Zhao, H. J. Fan, *Acs Nano* **2012**, *6*, 5531.

[101] Y. K. Hsu, Y. C. Chen, Y. G. Lin, L. C. Chen, K. H. Chen, *Chem. Commun.* **2011**, *47*, 1252.

[102] T. Y. Wei, C. H. Chen, H. C. Chien, S. Y. Lu, C. C. Hu, *Adv. Mater.* **2010**, *22*, 347.

[103] J. S. Chen, Z. Y. Wang, X. C. Dong, P. Chen, X. W. Lou, *Nanoscale* **2011**, *3*, 2158.

[104] J. H. Kim, K. Zhu, Y. F. Yan, C. L. Perkins, A. J. Frank, *Nano Lett.* **2010**, *10*, 4099.

[105] W. Y. Li, L. N. Xu, J. Chen, *Adv. Funct. Mater.* **2005**, *15*, 851.

[106] S. L. Xiong, J. S. Chen, X. W. Lou, H. C. Zeng, *Adv. Funct. Mater.* **2012**, *22*, 861.

[107] H. L. Wang, L. F. Cui, Y. A. Yang, H. S. Casalongue, J. T. Robinson, Y. Y. Liang, Y. Cui, H. J. Dai, *J. Am. Chem. Soc.* **2010**, *132*, 13978.

[108] L. F. Hu, L. M. Wu, M. Y. Liao, X. H. Hu, X. S. Fang, *Adv. Funct. Mater.* **2012**, *22*, 998.

[109] L. J. Wang, B. Liu, S. H. Ran, L. M. Wang, L. N. Gao, F. Y. Qu, D. Chen, G. Z. Shen, *J. Mater. Chem. A* **2013**, *1*, 2139.

[110] Z. Y. Wang, Z. C. Wang, W. T. Liu, W. Xiao, X. W. Lou, *Energy Environ. Sci.* **2013**, *6*, 87.

[111] Y. Wang, G. Z. Cao, *Adv. Mater.* **2008**, *20*, 2251.

[112] G. N. Zhu, Y. G. Wang, Y. Y. Xia, *Energy Environ. Sci.* **2012**, *5*, 6652.

[113] X. W. Lou, L. A. Archer, Z. C. Yang, *Adv. Mater.* **2008**, *20*, 3987.

[114] J. F. Li, S. L. Xiong, X. W. Li, Y. T. Qian, *J. Mater. Chem.* **2012**, *22*, 23254.

[115] I. Lahiri, S. W. Oh, J. Y. Hwang, S. Cho, Y. K. Sun, R. Banerjee, W. Choi, *Acs Nano* **2010**, *4*, 3440.

[116] L. Taberna, S. Mitra, P. Poizot, P. Simon, J. M. Tarascon, *Nat. Mater.* **2006**, *5*, 567.

[117] M. M. Shaijumon, E. Perre, B. Daffos, P. L. Taberna, J. M. Tarascon, P. Simon, *Adv. Mater.* **2010**, *22*, 4978.

[118] Z. S. Wu, W. C. Ren, L. Wen, L. B. Gao, J. P. Zhao, Z. P. Chen, G. M. Zhou, F. Li, H. M. Cheng, *Acs Nano* **2010**, *4*, 3187.

[119] H. W. Liu, J. Wang, *J. Electron. Mater.* **2012**, *41*, 3107.

[120] L. Hu, P. Zhang, H. Zhong, X. R. Zheng, N. Yan, Q. W. Chen, *Chem. Eur. J.*

2012, *18*, 15049.

[121] J. R. Miller, P. Simon, *Science* **2008**, *321*, 651.

[122] C. Liu, F. Li, L. P. Ma, H. M. Cheng, *Adv. Mater.* **2010**, *22*, E28.

[123] N. S. Choi, Z. H. Chen, S. A. Freunberger, X. L. Ji, Y. K. Sun, K. Amine, G. Yushin, L. F. Nazar, J. Cho, P. G. Bruce, *Angew. Chem. Int. Ed.* **2012**, *51*, 9994.

[124] C. Z. Yuan, H. B. Wu, Y. Xie, X. W. Lou, *Angew. Chem. Int. Ed.* **2013**, DOI:10.1002/anie.201303971.

[125] M. Winter, R. J. Brodd, *Chem. Rev.* **2004**, *104*, 4245.

[126] W. F. Wei, X. W. Cui, W. X. Chen, D. G. Ivey, *Chem. Soc. Rev.* **2011**, *40*, 1697.

[127] T. Wu, J. Y. Li, L. R. Hou, C. Z. Yuan, L. Yang, X. G. Zhang, *Electrochim. Acta* **2012**, *81*, 172.

[128] L. L. Li, S. J. Peng, Y. L. Cheah, P. F. Teh, J. Wang, G. Wee, Y. W. Ko, C. L. Wong, S. Madhavi, *Chem. Eur. J.* **2013**, *19*, 5892.

[129] R. J. Zou, K. B. Xu, T. Wang, G. J. He, Q. Liu, X. J. Liu, Z. Y. Zhang, J. Q. Hu, *J. Mater. Chem. A* **2013**.

[130] Z. Y. Wang, F. B. Su, S. Madhavi, X. W. Lou, *Nanoscale* **2011**, *3*, 1618.

[131] L. Yu, L. Zhang, H. B. Wu, G. Q. Zhang, X. W. Lou, *Energy Environ. Sci.* **2013**, *6*, 2664.

[132] H. Zhang, G. P. Cao, Z. Y. Wang, Y. S. Yang, Z. J. Shi, Z. N. Gu, *Nano Lett.* **2008**, *8*, 2664.

[133] G. Q. Zhang, X. W. Lou, *Sci. Rep.* **2013**, *3*.

[134] J. B. Goodenough, K. S. Park, *J. Am. Chem. Soc.* **2013**, *135*, 1167.

[135] A. S. Arico, P. Bruce, B. Scrosati, J. Tarascon, W. V. Schalkwijk, *Nat. Mater.* **2005**, *4*, 366.

[136] M. V. Reddy, G. V. Subba Rao, B. V. R. Chowdari, *Chem. Rev.* **2013**, *113*, 5364.

[137] C. Z. Yuan, H. B. Wu, Y. Xie, X. W. Lou, *Angew. Chem. Int. Ed.* **2014**, *53*, 1488.

[138] H. C. Chien, W. Y. Cheng, Y. H. Wang, S. Y. Lu, *Adv. Funct. Mater.* **2012**, *22*, 5038.

[139] L. F. Shen, L. Yu, X. Y. Yu, X. G. Zhang, X. W. Lou, *Angew. Chem. Int. Ed.* **2015**, *54*, 1868.

[140] Y. J. Chen, J. Zhu, B. H. Qu, B. A. Lu, Z. Xu, *Nano Energy* **2014**, *3*, 88.

[141] L. Huang, D. C. Chen, Y. Ding, S. Feng, Z. L. Wang, M. L. Liu, *Nano Lett.* **2013**, *13*, 3135.

[142] G. X. Gao, H. B. Wu, S. J. Ding, X. W. Lou, *Small* **2015**, *11*, 432.

[143] J. F. Li, J. Z. Wang, X. Liang, Z. J. Zhang, H. K. Liu, Y. T. Qian, S. L. Xiong, *ACS Appl. Mater. Interfaces* **2014**, *6*, 24.

[144] X. Wang, X. L. Wu, Y. G. Guo, Y. T. Zhong, X. Q. Cao, Y. Ma, J. N. Yao, *Adv. Funct. Mater.* **2010**, *20*, 1680.

[145] J. Y. Wang, N. L. Yang, H. J. Tang, Z. H. Dong, Q. Jin, M. Yang, D. Kisailus, H. J. Zhao, Z. Y. Tang, D. Wang, *Angew. Chem. Int. Ed.* **2013**, *52*, 6417.

[146] J. F. Li, J. Z. Wang, D. Wexler, D. Q. Shi, J. W. Liang, H. K. Liu, S. L. Xiong, Y. T. Qian, *J. Mater. Chem. A* **2013**, *1*, 15292.

[147] G. Q. Zhang, X. W. Lou, *Angew. Chem. Int. Ed.* **2014**, *53*, 9041.

[148] J. Liu, S. Z. Qiao, J. S. Chen, X. W. Lou, X. R. Xing, G. Q. Lu, *Chem. Commun.* **2011**, *47*, 12578.

[149] Y. J. Hong, M. Y. Son, Y. C. Kang, *Adv. Mater.* **2013**, *25*, 2279.

[150] L. Yu, L. Zhang, H. B. Wu, X. W. Lou, *Angew. Chem. Int. Ed.* **2014**, *53*, 3711.

[151] J. G. Guan, F. Z. Mou, Z. G. Sun, W. D. Shi, *Chem. Commun.* **2010**, *46*, 6605.

[152] W. Du, R. M. Liu, Y. W. Jiang, Q. Y. Lu, Y. Z. Fan, F. Gao, *J. Power Sources* **2013**, *227*, 101.

[153] C. Z. Yuan, J. Y. Li, L. R. Hou, X. G. Zhang, L. F. Shen, X. W. Lou, *Adv. Funct. Mater.* **2012**, *22*, 4592.

[154] S. Kuboon, Y. H. Hu, *Ind. Eng. Chem. Res.* **2011**, *50*, 2015.

[155] Y. N. Xu, X. F. Wang, C. H. An, Y. J. Wang, L. F. Jiao, H. T. Yuan, *J. Mater.*

Chem. A **2014**, *2*, 16480.

[156] Q. Zhou, X. Wang, Y. Liu, Y. He, Y. Gao, J. Liu, *J. Electrochem. Soc.* **2014**, *161*, A1922.

[157] L. Li, Y. Q. Zhang, F. Shi, Y. J. Zhang, J. H. Zhang, C. D. Gu, X. L. Wang, J. P. Tu, *ACS Appl. Mater. Interfaces* **2014**, *6*, 18040.

[158] L. B. Kong, C. Lu, M. C. Liu, Y. C. Luo, L. Kang, X. H. Li, F. C. Walsh, *Electrochim. Acta* **2014**, *115*, 22.

[159] L. L. Li, Y. Cheah, Y. W. Ko, P. Teh, G. Wee, C. L. Wong, S. J. Peng, M. Srinivasan, *J. Mater. Chem. A* **2013**, *1*, 10935.

[160] L. Liu, L.-Q. Yang, H.-W. Liang, H.-P. Cong, J. Jiang, S.-H. Yu, *ACS Nano* **2013**, *7*, 1368.

[161] H. Guo, L. X. Liu, T. T. Li, W. W. Chen, J. J. Liu, Y. Y. Guo, Y. C. Guo, *Nanoscale* **2014**, *6*, 5491.